



**POLITECNICO**  
MILANO 1863



**Jet Propulsion Laboratory**  
California Institute of Technology

# Granular Imager: Modeling and Control

Supervisor: **Prof. Francesco Braghin**  
Politecnico di Milano

Mentor: **Dr. Marco B. Quadrelli**  
Jet Propulsion Laboratory, California Institute of Technology

Author:  
**Carlo Sinigaglia**  
878386

Academic year 2018/2019



This research was carried out at Jet Propulsion Laboratory, California Institute of Technology, during the internship sponsored by JVSRP (JPL Visiting Student Research Program) and NASA.



# Acknowledgments

I would like to express my special appreciation and thanks to my mentor at JPL Dr. Marco B. Quadrelli, who guided me with enthusiasm throughout the course of this research.

I would like to thank my supervisor at Politecnico di Milano, Prof. Francesco Braghin, for he gave me this opportunity and for having inspired me during the course of my studies.

Special thanks go to my lab mates, my time at JPL and in Pasadena would have not been the same without you.

Last but not least, I would like to thank my family for their encouragement and support throughout all my studies.



## Abstract

The purpose of this dissertation was to investigate modeling and control strategies for the Granular Imager (GI) concept. The GI idea is the result of an ongoing research endeavour to study the feasibility of a distributed space imaging system, whose optical surface is made of a granular cloud of reflective particles instead of a monolithic mirror. This work is framed in the 'Orbiting Rainbows' paradigm, a Phase II NIAC (Nasa Innovative Advanced Concepts) project.

The overall modeling problem involves a very large parameter space (i.e. optics, laser matter interaction, disordered systems, multi-scale simulation, formation flying, distributed systems, granular media, plasma physics, gravito-electro dynamics). In this dissertation, the overall system is modeled as a large ensemble of rigid bodies, physically disconnected from each other, whose interconnections depend on the actuation force fields. The nature of the system is modular both at the micro and macro scale. The subsystem elemental body at the macro-scale is a large satellite that contains and confine the granular media cloud. This spacecraft constitutes an optical sub-aperture that flying in formation with other identical elements generates a very large synthetic aperture. The elemental system at the micro-scale (i.e. a reflective grain) is modeled as a micrometric rigid body. A large number of these elements constitutes the granular cloud in each sub-aperture.

A complete model of this system is implemented and analyzed in the physics-based simulation software DSENDSEdu thus addressing the multi-scale dynamics. A set of relative equations of motion for the system in orbits is derived analytically and used to synthesize the various control strategies developed throughout this work.

The control problem at the macro-scale consists of formation flying multiple granular sub-apertures and it is solved with a linear optimal tracking controller. This strategy is simulated in the DSENDSEdu environment that allows to analyze the grain behaviour during formation keeping and retargeting.

The challenging task of controlling the grain dynamics at the micro-scale is considered both from a deterministic and a stochastic perspective. A laser interaction model based on ray-tracing techniques is used to derive a dynamical model for the grain behaviour while subjected to laser radiation. In this framework, a geometrical time-optimal control law based on a bilinear approximation of the system is derived for grain realignment, while nonlinear strategies for state-dependent models (i.e. state-dependent unconstrained and constrained Riccati approaches) are used for position and orientation control. A novel control strategy, based on the kinematic properties of the phase-plane generated by the geometrical control law, is considered to partially realign multiple grains simultaneously in the absence of damping and with a single laser source.

The problem of controlling a large number of particles with a small set of actuators necessarily asks for a controllability analysis. The failure of controllability in a deterministic sense sets the path for reformulating the problem under a stochastic viewpoint. A probabilistic approach for controlling the average space distribution of the particles is developed considering a simplified dynamical model. This strategy is based on Optimal Transport theory, that provides a mathematical framework to derive 'optimal' ways of transporting probabilistic distributions. The problem of controlling the collective dynamics of the particles is transported in the probability space, in which an optimal control problem is solved for the density evolution. A novel metric derived from Optimal Transport theory is used to overcome some limitations of the previous implementations. Numerical simulations proved the effectiveness of this strategy thus suggesting a future integration with the complete simulation model.

# Contents

<b>1</b>	<b>Introduction</b>	<b>1</b>
1.1	Motivations and existing technology . . . . .	2
1.2	Granular Imager concept design . . . . .	4
1.3	Modeling of the diffuse medium . . . . .	6
1.4	Work subdivision . . . . .	7
<b>2</b>	<b>Equations of motion</b>	<b>9</b>
2.0.1	Systems definition . . . . .	9
2.0.2	Translational equations of motion of spacecraft S . . . . .	10
2.0.3	State-space form and controllability analysis . . . . .	13
2.0.4	Spacecraft attitude dynamics and control problem . . . . .	14
2.0.5	Equation of motion of the cloud particle P relative to Spacecraft S . . . . .	15
<b>3</b>	<b>Laser interaction and control</b>	<b>17</b>
3.1	Actuator model and assumptions . . . . .	17
3.1.1	Ray-tracing model . . . . .	18
3.1.2	Actuators layout and particle properties . . . . .	21
3.2	Hemisphere 1DOF rotational model . . . . .	22
3.2.1	Structure and stability . . . . .	23
3.3	Control strategies for the 1DOF model . . . . .	25
3.3.1	Feedback linearization . . . . .	26
3.3.2	Time-optimal control . . . . .	26
3.3.3	Geometric control approach . . . . .	27
3.3.4	Kinematic properties of the phase-plane . . . . .	31
3.3.5	Numerical controlled response simulations . . . . .	34
3.3.6	Simultaneous single-input global control . . . . .	39
3.4	Hemisphere 3DOF model . . . . .	45
3.4.1	State-space formulation . . . . .	47
3.5	Control strategies for the 3DOF model . . . . .	47

3.5.1	State-dependent Riccati equation approach . . . . .	48
3.5.2	CD-SDR MPC approach . . . . .	52
3.6	Controllability for multiple hemispheres . . . . .	56
<b>4</b>	<b>Particle density control</b>	<b>58</b>
4.1	Considerations on controllability . . . . .	59
4.2	Collective control . . . . .	62
4.2.1	Optimal Transport based control . . . . .	62
4.3	OT with Euler step dynamics . . . . .	63
4.3.1	Derivation of the stochastic density evolution . . . . .	64
4.3.2	Optimal Transport based control problem . . . . .	66
4.3.3	Limitation of the current implementation . . . . .	67
4.4	Reformulation of the OT problem . . . . .	69
4.4.1	Earth’s mover distance . . . . .	69
4.4.2	Density control using the earth’s mover distance . . . . .	70
4.4.3	Nonlinear optimization problem . . . . .	70
<b>5</b>	<b>DSENDSEdu model</b>	<b>75</b>
5.1	System modeling and assumptions . . . . .	75
5.2	Model structure and implementation . . . . .	76
5.2.1	Open serial kinematic tree . . . . .	77
5.2.2	Parallel kinematic tree . . . . .	77
5.3	Force fields implementation . . . . .	78
5.3.1	Gravitational model . . . . .	78
5.3.2	Particle force fields . . . . .	78
5.4	Formation control scheme . . . . .	79
5.4.1	Validation of the linearized gravitational model . . . . .	80
5.4.2	LQR-based leader tracking . . . . .	82
5.4.3	LQR-based trajectory following . . . . .	85
5.5	Attitude control . . . . .	91
5.6	Granular medium model . . . . .	94
5.6.1	Realignment . . . . .	95
5.6.2	Decoupling and confinement . . . . .	98
<b>6</b>	<b>Conclusions and future work</b>	<b>103</b>
6.1	Research outcome and discussion . . . . .	103
6.2	Future work . . . . .	104
	<b>Appendices</b>	<b>109</b>
	<b>Appendix A Mathematical preliminaries</b>	<b>109</b>

A.0.1	Notation . . . . .	109
A.0.2	Reference frames and vectrices . . . . .	110
A.0.3	Vector derivatives in different reference frames . . . . .	111

# Chapter 1

## Introduction

This dissertation is the result of a seven month internship at NASA Jet Propulsion Laboratory under the JPL Visiting Research Student Program. This work is framed into the 'Orbiting Rainbows' paradigm, a Phase II NASA Innovative Advanced Concepts (NIAC) study whose aim is to extend the boundary of human space knowledge by advancing the current technology of space telescopes. The main limiting factor of current designs is the weight and cost of the primary aperture that does not allow to increase the dimension over a certain threshold, thus hindering the development of large aperture imaging systems. The radical difference envisioned by the 'Orbiting Rainbows' concept is to exploit the reflective and refractive properties of a cloud of grains to substitute a monolithic aperture with a distributed granular medium. In this way, the granular lens can achieve very large apertures at a fraction of weight and cost with respect to its classical monolithic counterpart. The Granular Imager (GI) design is made possible by recent theoretical and experimental understandings on the behaviour of diffuse granular media that open the way to new methods to sense and control these systems. The overall problem involves many areas of engineering simultaneously from cloud optics to distributed control strategies. However, the research carried out in Phase I and Phase II proved that the Granular Imager is feasible but also requires advancements in different areas. This dissertation will be focused on the modeling and control of a possible design of the Granular Imager (GI) from the dynamics perspective.

## 1.1 Motivations and existing technology

Typically, the cost of a space-borne imaging system is driven by the size and mass of the primary aperture. The solution proposed uses a method to construct an imaging system in orbit in which the nonlinear optical properties of a cloud of reflective particles, shaped into a stable surface, allow to form a lightweight aperture of an imaging system, hence reducing overall mass and cost. The trend in astronomy requires larger and larger aperture to allow challenging goals such as exo-planet detection. The need for an ultra lightweight very large aperture design is of fundamental importance.

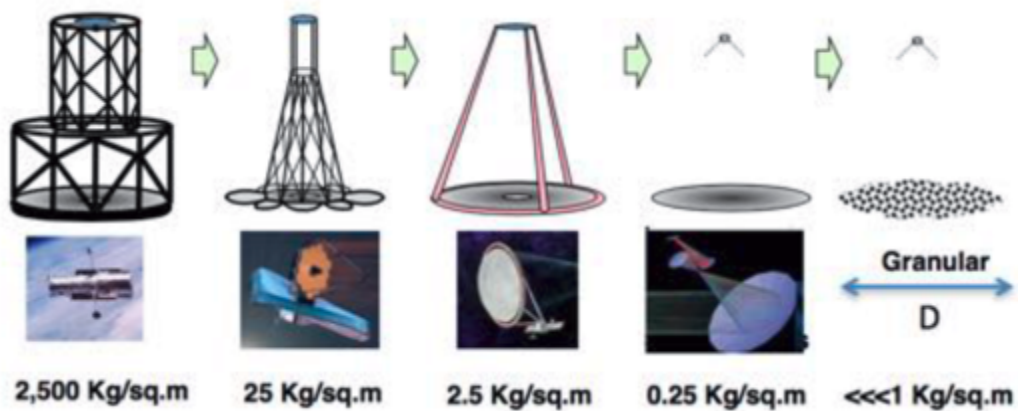


Figure 1.1: Evolution of large space telescopes

Metric	Conventional Mirror SoA	Light-Weight Mirror SoA	Inflatable	Liquid mirror	Granular Imager
Mass Areal Density	40-100 kg/m <sup>2</sup>	10-20 kg/m <sup>2</sup>	<5 kg/m <sup>2</sup>	100-200 kg/m <sup>2</sup>	<<0.1 kg/m <sup>2</sup>
Surface Figure Error	10 nm RMS	14 nm RMS	<5 micro-m RMS	<5 micro-m RMS	<100 nm RMS
Surface microroughness	<5Å	<10Å	500 nm	20 nm	< 100Å
First free-free mode	>100Hz	>100Hz	>1 Hz	>10 Hz	< 1 mHz
Size	0.1 to 2.4m and larger	0.3 to 1.35m and larger	1 to 10 m	1 to 10 m	> 10 m
Deployable	No	No	Yes	No	Yes
Thermal stability	Low CTE	Thermally controlled	Thermally Controlled	Thermally Controlled	Thermally Controlled
Formation Flying	No	No	No	No	Yes
Wavelength	Visible	Visible	Visible/Radar	Visible	Visible/Radar
Orbit	L2	L2	LEO	Ground	GEO/L2
Backing Structure	Yes	Yes	Yes	Yes	No
Packaging	Complex	Complex	Medium	N/A	Simple
Retargeting	RCS	RCS	RCS	No	Optical/EM
Fault-tolerance	Low	Low	Low	Low	High

Figure 1.2: State of the art of the current telescope technology

The concept of one single granular member can be further extended considering multiple sub-aperture patches that flying in formation would achieve even larger overall equivalent dimension invoking synthetic aperture interferometry techniques such as Golog arrays [23]. However, this increases the complexity of the overall system adding precise formation flying requirements. Other space-borne observatories proposed missions consider multiple elements, such as the New World Observer (NWO) or the Stellar Imager (SI). NWO consists of a large telescope and an occulter spacecraft in tandem at about 50,000 km apart. The aperture is limited to four meter due to its monolithic structure. On the other hand, the SI is an ultraviolet/optical aperture synthesis imager composed of at least 9, up to perhaps as many as 30, array elements (mirrorsats) and a central hub with focal-plane instrumentation. In a similar way, the granular sub-aperture patches of the Granular Imager will focus light on a central chief spacecraft. The fundamental difference is in the architecture of the mirror that allows to increase the aperture at the level of the single sub-apertures.

It is extremely difficult to design large aperture space optics which are both optically precise and can meet the practical requirements for launch and deployment in space [24]. Compared to conventional large aperture systems, the proposed con-

cept is unique in that: a) it would be a structure-less, very lightweight system, leading to areal densities of  $0.1 \left[ \frac{Kg}{m^2} \right]$  or less, compared to  $10 \left[ \frac{Kg}{m^2} \right]$  or more of monolithic apertures; b) one cloud could combine with other clouds to form extremely large apertures; c) would be easy to package, not requiring structural elements; d) line-of-sight retargeting and figure control would be realized remotely using electromagnetic fields, without the need for complex sensors and actuators on the backing structure. These properties enable new mission architectures, and are in contrast to current state-of-the-art systems which are limited to much smaller sizes and are quite massive. The paradigm that makes this Granular Imager possible is based on: a) avoiding any physical structure and sensing/actuation hardware on the primary aperture; b) using at-a-distance trapping and manipulation to confine and shape the cloud acting as primary.

## 1.2 Granular Imager concept design

The concept considered is a set of multiple satellite agents, each one integrates a granular aperture. It will be shown that the control challenges addressed are inherently multi-scale due to the simultaneous formation flying of these sub-apertures at the macro-scale and the collective behaviour of the grains at the micro-scale. However, it is possible to invoke spectral decoupling arguments and consider the two control problems separately.

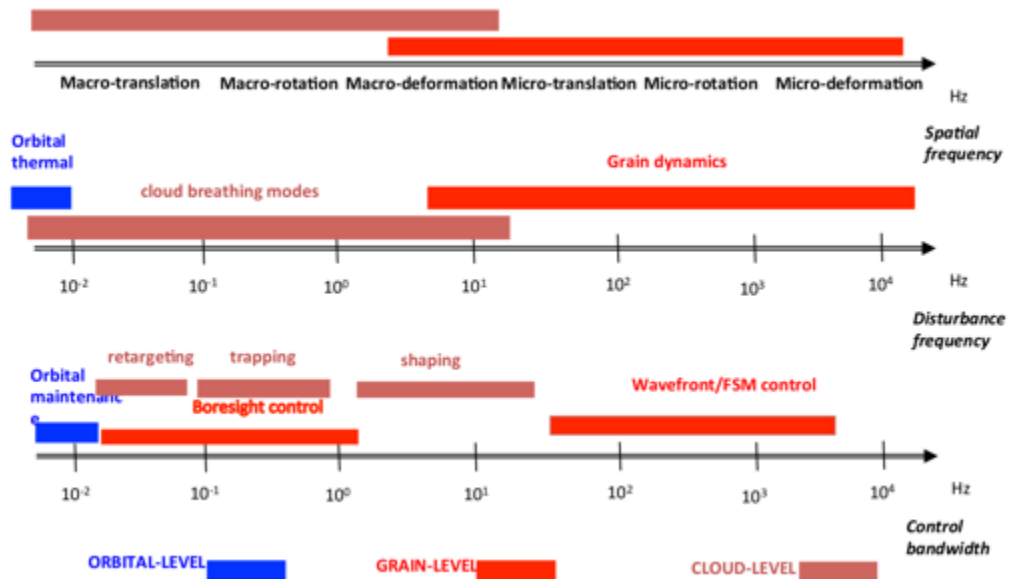


Figure 1.3: Spatial, temporal, and control scales involved in the GI problem [5]

At the level of the single sub-aperture, the stable confinement and rigidification of the granular medium at the micro-scale is envisioned to be obtained as follows [5]. First, the diffuse reflective is dispensed within a transparent inflatable envelope containing a neutral buffer gas, such as  $Ar$ . The released cloud is then guided into a stable Coulomb crystal by adjusting the boundary potentials of an electrodynamic trap to satisfy the condition for crystal formation. Once the crystal has been formed, the rotational alignment of the grains into the incoming wavefront is achieved by rastering a laser beam across the extent of the cloud. The radiation pressure of the laser beam rotates the grains in the proper direction.

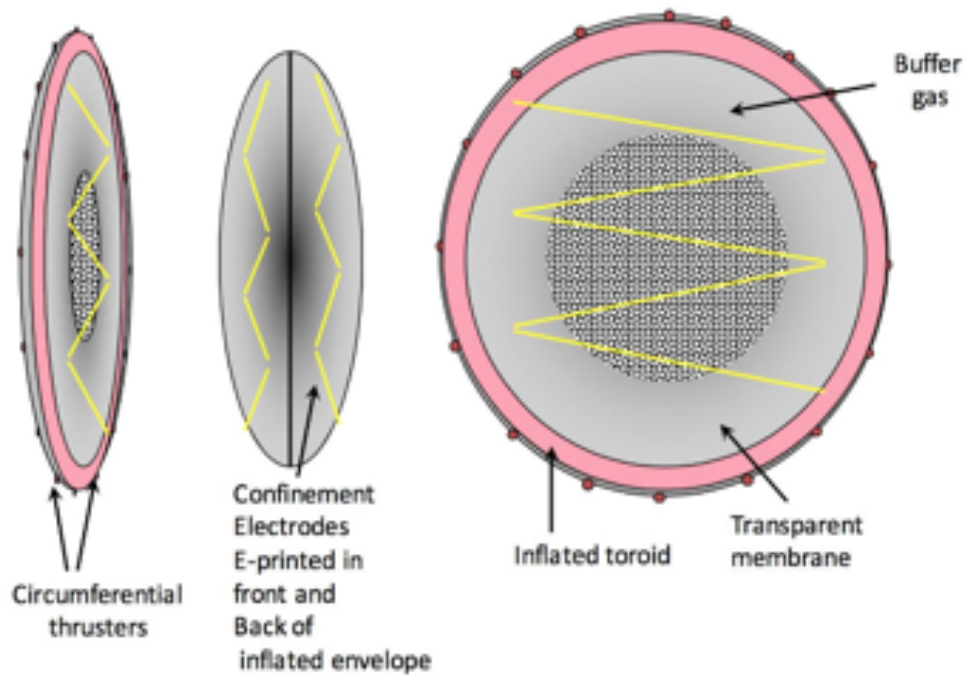


Figure 1.4: Sub-aperture schematic schematic concept

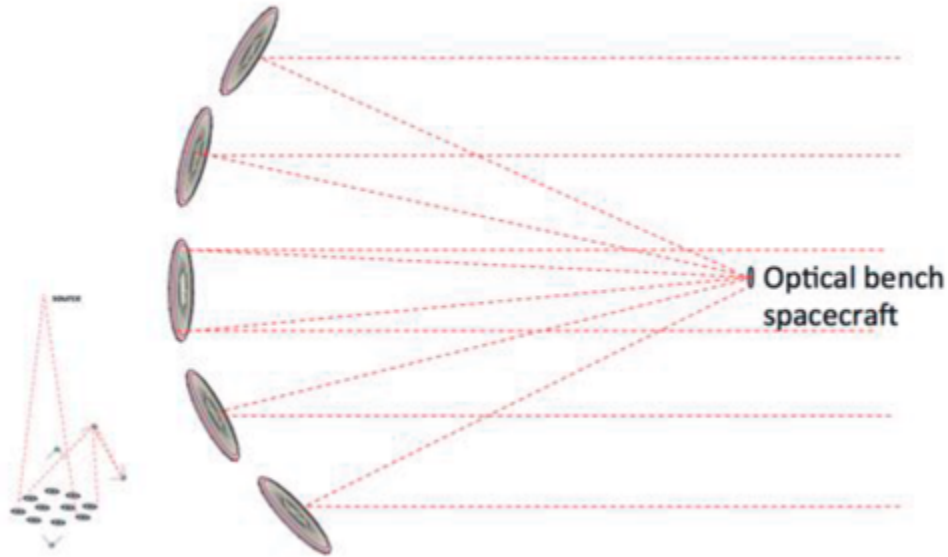


Figure 1.5: Formation flying of multiple sub-apertures

Through optical manipulation technology, the average alignment of the grains is controlled within each cloud to provide a cloud figure shape that is adequate for the optical requirements. Therefore, the top-down formation flying approach merges with the bottom-up optical manipulation approach to achieve the objective. The radical difference with respect to the existing technology consists of the 'at-a-distance' nature of the actuation of the granular lens that in this way does not need any backing structure or precise mechanical design. On the other hand, it poses complex challenges in the simultaneous control and alignment of many grains subjected to the same force field generated by the actuators. The addition of the buffer gas provides additional dissipation and allows the particles to be stabilized more easily. The control system is envisioned to be based on feeding back images of the cloud to the boundary electrodes so that with proper tuning a stable equivalent surface can be achieved.

### 1.3 Modeling of the diffuse medium

The dynamics of diffuse media is a complex phenomenon to model from the dynamics point of view [24, 5]. The granular medium presents many unique properties that can be considered a different state of matter in itself. Among its peculiar characteristics there are cohesiveness, fluid behaviour, compactification, phase transformation capability and many others. The controllable properties and manipulation capability

of these systems are matter of on-going research starting from the modeling point of view. There are many ways to model the dynamics of diffuse media, such as Cellular Automata or Lattice-Boltzmann Hydrodynamics [26, 5]. These techniques allow to describe the cloud dynamics within a specified spatial domain  $\Omega$  as a boundary value problem together with the stochastic equation of motion:

$$[\Gamma(x, t) + \Sigma(x, t, \omega)]u(x, t, \omega) = f(x, t, \omega) + f_c(x, t) \quad (1.1)$$

The operators in the equation of motion are stochastic due to the probabilistic nature of the single grains dynamics and of the whole system. Equation 1.1 describes the system together with the boundary conditions at  $\delta\Omega$ .  $x$  represents the spatial scale,  $t$  the temporal scale,  $\omega$  the random fluctuation,  $\Gamma$  is the deterministic operator describing the dynamics while  $\Sigma$  is the stochastic operator whose coefficients are zero-mean random process.  $u$  is the displacement of a grain of the cloud,  $f$  is the vector of exogenous disturbances and  $f_c$  the vector of control inputs. For a diffuse medium, two time scales enter the picture, as well as two spatial scales. The individual grain dynamics begins to emerge when  $\frac{\lambda}{L} \approx 1$ , where  $\lambda$  is the time (or space) scale of the stimuli internal or external to the cloud, whereas  $L$  is a time (or space) scale representative of the cloud itself. When  $\frac{\lambda}{L} \ll 1$ , the individual grain behavior is predominant, and when  $\frac{\lambda}{L} \gg 1$  the cloud collective behavior as a unit is predominant, therefore in this situation it could be considered as an effective rigidified medium (rigid body). In this dissertation, to keep the problem tractable, the system of grains (particles) will be modeled as a large set of micrometric rigid bodies, with the aim of studying their behaviour at the micro and macro scale separately, and when coupled with the macroscopic system in orbit.

## 1.4 Work subdivision

The main objective of this dissertation was to develop a multi-scale simulation environment that allows to study the interconnections between the different time scales at which the overall system is subjected and, at the same time, to develop control methodologies that can handle this multi-scale problem. In particular, classical optimal control theory is used for the formation flying problem at the macro-scale while nonlinear, deterministic and stochastic, control strategies are used to control the grains (granular ensemble) at the micro-scale. The equations of motion of the system in orbit around Earth are investigated in the first chapter. A linearized set of translational motion equations, useful to synthesize formation flying control algorithms, is derived for the relative motion of the formation of the sub-apertures. The particles (grains) full relative dynamics with respect to its container (inflatable envelope) is analytically described and an approximation to these equations is used to

implement control strategies in the following chapter. In the laser chapter, a laser-matter interaction model is used to synthesize two main nonlinear control strategies that allows realignment and position control. A novel control approach is proposed to simultaneously realign multiple grains with a single laser source in absence of damping. Chapter 4 addresses the problem of controlling the average position of thousands of particles simultaneously. After some considerations on the lack of classical controllability with the layout considered, a stochastic density control approach is developed based on the Optimal Mass Transport theory. This strategy allows to achieve global control of the collective behaviour of thousands of particles based on a simplified model. This stochastic viewpoint is needed to the partial failure of the deterministic control methodologies developed in chapter 3 in handling multiple particles simultaneously. In the last chapter, a complete simulation of the GI system is performed in the DSENDSEdu simulator engine, a C++\Python physics-based multi-body simulation software developed at NASA Jet Propulsion Laboratory. The environment has been implemented to allow inherent scalability on the number of particles and on the number of sub-apertures. Furthermore, it incorporates several phenomena that the granular particles inside the envelope experience. Specifically, the nonlinear laser-particle interaction, the presence of the buffer gas and a simplified model for the electrodynamic interaction. A complete simulation is then carried out, the (GI) system composed of a certain number of granular apertures perform formation flying tasks while retargeting to a point on Earth simulating Earth-Imaging applications. A quaternion-based PD attitude control is used at the macro scale while at the micro-scale the particles are realigned using laser radiation pressure. The global realignment has been achieved due to the presence of damping.

# Chapter 2

## Equations of motion

In this chapter, the equations of motion describing the relative dynamics of the elements of the Granular Imager are derived. At the macro-scale, the dynamics of the sub-aperture patches (spacecrafts) is described relative to an orbiting reference frame. On the other hand, at the micro-scale the dynamics of the particles is referred to its relative container.

### 2.0.1 Systems definition

Several reference frames are defined to describe the motion of the system, following the approach used in [27]. An inertial reference frame  $\mathcal{F}_I$  is attached to the center of Earth and is oriented following the commonly accepted convention for Earth-centered inertial frames. The x axis points towards the vernal equinox, the z axis points toward the North Pole and the y axis completes the right-handed frame. An orbiting reference, frame  $\mathcal{F}_O$ , follows a keplerian orbit around Earth and rotates with angular velocity  ${}^I\boldsymbol{\omega}^O$  with respect to  $\mathcal{F}_I$ . The location of the origin of  $\mathcal{F}_O$  is a circular solution to the following two-body problem with Earth as the central body:

$$\overset{II}{\underline{\mathbf{R}}}_O = -\frac{\mu \underline{\mathbf{R}}_O}{\|\underline{\mathbf{R}}_O\|^3} \quad (2.1)$$

The orientation of  $\mathcal{F}_O$  is given by its unit vectors  $\{\hat{\mathbf{q}}_1, \hat{\mathbf{q}}_2, \hat{\mathbf{q}}_3\}$ . The unit vector  $\hat{\mathbf{q}}_1$  points towards the radial direction, the unit vector  $\hat{\mathbf{q}}_3$  points in the direction of the orbit normal while the unit vector  $\hat{\mathbf{q}}_2$  completes the right-handed triad. An orbiting reference frame with this orientation is commonly referred as the Hill reference frame. Its origin follows a purely gravitational circular orbit and due to the definition of its orientation its angular velocity with respect to the inertial frame  $\mathcal{F}_I$  is constant and equal to the mean motion of the orbit.

A body-fixed reference frame  $\mathcal{F}_S$  is defined for each spacecraft that in turn contains a cloud of particles modeled as an ensemble of rigid bodies. The point describing the location of the center of mass of a generic particle is denoted as P.

A set of coordinate-free vectors is defined to describe the kinematics of the problem.

- $\underline{\mathbf{R}}_O$  is the vector from  $\mathcal{F}_I$  origin to  $\mathcal{F}_O$  origin.
- $\underline{\boldsymbol{\rho}}_S$  is the vector from  $\mathcal{F}_O$  origin to  $\mathcal{F}_S$  origin.
- $\underline{\mathbf{r}}_S$  is the vector from  $\mathcal{F}_I$  origin to  $\mathcal{F}_S$  origin.
- $\underline{\boldsymbol{\rho}}_P$  is the vector from  $\mathcal{F}_S$  origin to point P.
- $\underline{\mathbf{r}}_P$  is the vector from  $\mathcal{F}_I$  origin to point P.

The following relations follow from these definitions:

$$\underline{\mathbf{r}}_S = \underline{\boldsymbol{\rho}}_S + \underline{\mathbf{R}}_O \quad (2.2)$$

$$\underline{\mathbf{r}}_P = \underline{\boldsymbol{\rho}}_P + \underline{\boldsymbol{\rho}}_S + \underline{\mathbf{R}}_O = \underline{\boldsymbol{\rho}}_P + \underline{\mathbf{r}}_S \quad (2.3)$$

## 2.0.2 Translational equations of motion of spacecraft S

The translational equations of motion of a deputy spacecraft S are derived according to the following assumptions. The spacecraft is actuated in each of the three linear degrees of freedom by a control force (e.g. thrusters) and it is subjected to spherical gravity exerted towards the center of Earth (i.e. origin of  $\mathcal{F}_I$ ). Disturbance forces, radiation forces, third body perturbation and Earth oblateness are, for the time being, neglected. The mutual gravitational forces exerted by the cloud on the spacecraft are also neglected as it will be proved to be order of magnitudes smaller than the other forces. Hence, using Newton's Second Law:

$$\overset{II}{\underline{\mathbf{r}}}_S = -\frac{\mu \underline{\mathbf{r}}_S}{\|\underline{\mathbf{r}}_S\|^3} + \frac{\underline{\mathbf{F}}_{CS}}{m_S} \quad (2.4)$$

Differentiating equation 2.2 twice and using the propagation equation of point O in equation 2.1, it is possible to rearrange equation 2.4 and expresses it in terms of relative motion between the spacecraft and the orbiting reference frame (i.e.  $\underline{\boldsymbol{\rho}}_S$ ).

$$\overset{II}{\underline{\boldsymbol{\rho}}}_S = \overset{II}{\underline{\mathbf{r}}}_S - \overset{II}{\underline{\mathbf{R}}}_O = -\mu \left[ \frac{\underline{\mathbf{r}}_S}{\|\underline{\mathbf{r}}_S\|^3} - \frac{\underline{\mathbf{R}}_O}{\|\underline{\mathbf{R}}_O\|^3} \right] + \frac{\underline{\mathbf{F}}_{CS}}{m_S} \quad (2.5)$$

The Transport Theorem can be now applied twice to  $\overset{II}{\underline{\boldsymbol{\rho}}}_S$  so as to refer all the derivatives to the  $\mathcal{F}_O$  frame:

$$\underline{\rho}_S^H = \underline{\rho}_S^{OO} + 2 {}^I\underline{\omega}^O \times \underline{\rho}_S^O + {}^I\underline{\omega}^O \times {}^I\underline{\omega}^O \times \underline{\rho}_S \quad (2.6)$$

In equation 2.6 the assumption that the origin of  $\mathcal{F}_O$  is following a circular orbit with constant angular velocity is used, as a consequence, the angular velocity  ${}^I\underline{\omega}^O$  of frame  $\mathcal{F}_O$  with respect to  $\mathcal{F}_I$  is constant. Thus substituting 2.6 into 2.5:

$$\underline{\rho}_S^{OO} = -2 {}^I\underline{\omega}^O \times \underline{\rho}_S^O - {}^I\underline{\omega}^O \times {}^I\underline{\omega}^O \times \underline{\rho}_S - \mu \left[ \frac{\underline{r}_S}{\|\underline{r}_S\|^3} - \frac{\underline{R}_O}{\|\underline{R}_O\|^3} \right] + \frac{\underline{F}_{CS}}{m_S} \quad (2.7)$$

There is indeed a large difference between  $\underline{R}_O$  and  $\underline{\rho}_O$  that can be exploited to simplify and linearize the equation of motion. The nonlinear term in equation 2.7 is represented by the differential gravity term. The term  $\|\underline{r}_S\|^2$  can be expanded and rearranged as a function of  $\underline{\rho}_S$  and  $\underline{R}_O$  only.

$$\|\underline{r}_S\| = \|\underline{\rho}_S + \underline{R}_O\| = [(\underline{\rho}_S + \underline{R}_O) \cdot (\underline{\rho}_S + \underline{R}_O)]^{\frac{1}{2}} \quad (2.8)$$

$$\|\underline{r}_S\|^3 = [(\underline{\rho}_S + \underline{R}_O) \cdot (\underline{\rho}_S + \underline{R}_O)]^{\frac{3}{2}} = \|\underline{R}_O\|^3 \left[ 1 + \frac{\underline{\rho}_S \cdot \underline{\rho}_S + 2\underline{R}_O \cdot \underline{\rho}_S}{\|\underline{R}_O\|^2} \right]^{\frac{3}{2}} \quad (2.9)$$

Equation 2.9 is then substituted in the differential gravity term in 2.7, thus obtaining:

$$\mu \left[ \frac{\underline{r}_S}{\|\underline{r}_S\|^3} - \frac{\underline{R}_O}{\|\underline{R}_O\|^3} \right] = \frac{\mu}{\|\underline{R}_O\|^3} \left[ (\underline{\rho}_S + \underline{R}_O) \left[ 1 + \frac{\underline{\rho}_S \cdot \underline{\rho}_S + 2\underline{R}_O \cdot \underline{\rho}_S}{\|\underline{R}_O\|^2} \right]^{-\frac{3}{2}} - \underline{R}_O \right] \quad (2.10)$$

Due to the assumption made earlier (i.e.  $\|\underline{\rho}_S\| \ll \|\underline{R}_O\|$ ), the last term of equation 2.10 can be expanded in Taylor series up to first order:

$$\left[ 1 + \frac{\underline{\rho}_S \cdot \underline{\rho}_S + 2\underline{R}_O \cdot \underline{\rho}_S}{\|\underline{R}_O\|^2} \right]^{-\frac{3}{2}} \approx \left[ 1 - \frac{3}{2} \frac{\underline{\rho}_S \cdot \underline{\rho}_S + 2\underline{R}_O \cdot \underline{\rho}_S}{\|\underline{R}_O\|^2} \right] \quad (2.11)$$

Equation 2.11 is then substituted back in 2.10, rearranging terms and using the definition of dyadic product yields:

$$\mu \left[ \frac{\underline{r}_S}{\|\underline{r}_S\|^3} - \frac{\underline{R}_O}{\|\underline{R}_O\|^3} \right] \approx \frac{\mu}{\|\underline{R}_O\|^3} \underline{\underline{G}} \underline{\rho}_S - \frac{3\mu}{2\|\underline{R}_O\|^5} (2\underline{\rho}_S \underline{R}_O + \underline{R}_O \underline{\rho}_S + \underline{\rho}_S \underline{\rho}_S) \underline{\rho}_S \quad (2.12)$$

Where:

$$\underline{\underline{G}} = \frac{\|\underline{R}_O\|^2 \underline{\underline{1}} - 3\underline{R}_O \underline{R}_O}{\|\underline{R}_O\|^2} = \underline{\underline{1}} - 3\hat{\underline{\rho}}_1 \hat{\underline{\rho}}_1 \quad (2.13)$$

The last equation 2.13 is derived considering the definition of the orbiting reference frame  $\mathcal{F}_O$  where  $\underline{R}_O = \|\underline{R}_O\| \hat{\underline{\rho}}_1$ . Furthermore,  ${}^I\underline{\omega}^O = \|\underline{\omega}^O\| \hat{\underline{\rho}}_3$  where the norm of  ${}^I\underline{\omega}^O$  is the mean motion of the circular orbit  $\omega_O$  and is given by  $\omega_O^2 = \frac{\mu}{\|\underline{R}_O\|^3}$ . Finally,

neglecting the quadratic terms in equation 2.12, the linearized vectorial equation of motion of spacecraft S can be written as:

$$\overset{OO}{\underline{\dot{\rho}}}_S = -2{}^I\omega^O \times \overset{O}{\underline{\rho}}_S - {}^I\omega^O \times {}^I\omega^O \times \overset{O}{\underline{\rho}}_S - \omega_O^2 \underline{\underline{G}} \overset{O}{\underline{\rho}}_S + \frac{\underline{\underline{F}}_{CS}}{m_S} \quad (2.14)$$

Note that equation 2.14 is in coordinate-free form but all the time derivatives are taken with respect to the orbiting reference frame  $\mathcal{F}_O$ .

It is now possible to project the equation of motion in 2.14 in  $\mathcal{F}_O$ . The components of the vector  $\overset{O}{\underline{\rho}}_S$ , its derivatives and of the dyadic  $\underline{\underline{G}}$  can be obtained using the vectrix calculus:

$$[G] = \mathcal{F}_O \cdot \underline{\underline{G}} \cdot \mathcal{F}_O^T = \begin{bmatrix} -2 & 0 & 0 \\ 0 & 1 & 0 \\ 0 & 0 & 1 \end{bmatrix} \quad (2.15)$$

$$\underline{\rho}_S = \mathcal{F}_O \cdot \overset{O}{\underline{\rho}}_S = \begin{bmatrix} \rho_{Sx} \\ \rho_{Sy} \\ \rho_{Sz} \end{bmatrix} \quad (2.16)$$

$$\dot{\underline{\rho}}_S = \mathcal{F}_O \cdot \overset{O}{\underline{\dot{\rho}}}_S = \begin{bmatrix} \dot{\rho}_{Sx} \\ \dot{\rho}_{Sy} \\ \dot{\rho}_{Sz} \end{bmatrix} \quad (2.17)$$

$${}^I\omega^O = \mathcal{F}_O \cdot \overset{O}{\underline{\omega}}^O = \begin{bmatrix} 0 \\ 0 \\ \omega_O \end{bmatrix} \quad (2.18)$$

$$\underline{\underline{F}}_{CS} = \mathcal{F}_O \cdot \underline{\underline{F}}_{CS} = \begin{bmatrix} F_{CSx} \\ F_{CSy} \\ F_{CSz} \end{bmatrix} \quad (2.19)$$

The equation of motion, now expressed as a matrix equation, is:

$$\ddot{\underline{\rho}}_S = -2[{}^I\omega^O]^\times \dot{\underline{\rho}}_S - [{}^I\omega^O]^\times [{}^I\omega^O]^\times \underline{\rho}_S - \omega_O^2 [G] \underline{\rho}_S + \frac{\underline{\underline{F}}_{CS}}{m_S} \quad (2.20)$$

By doing the necessary calculations and expressing the column matrices by components the explicit form of equation 2.20 is:

$$\begin{bmatrix} \ddot{\rho}_{Sx} \\ \ddot{\rho}_{Sy} \\ \ddot{\rho}_{Sz} \end{bmatrix} = -2 \begin{bmatrix} 0 & -\omega_O & 0 \\ \omega_O & 0 & 0 \\ 0 & 0 & 0 \end{bmatrix} \begin{bmatrix} \dot{\rho}_{Sx} \\ \dot{\rho}_{Sy} \\ \dot{\rho}_{Sz} \end{bmatrix} + \begin{bmatrix} 3\omega_O^2 & 0 & 0 \\ 0 & 0 & 0 \\ 0 & 0 & -\omega_O^2 \end{bmatrix} \begin{bmatrix} \rho_{Sx} \\ \rho_{Sy} \\ \rho_{Sz} \end{bmatrix} + \frac{1}{m_S} \begin{bmatrix} F_{CSx} \\ F_{CSy} \\ F_{CSz} \end{bmatrix} \quad (2.21)$$

### 2.0.3 State-space form and controllability analysis

Equation 2.21 is called Clohessy-Wiltshire-Hill (CWH) equation and has been obtained under the following fundamental assumption: linearized system, circular reference orbit and spherical Earth gravity. Furthermore, it is assumed that the only forces acting on the body are gravity and control actions. These equations will be used to synthesize the control logic for each spacecraft. It is useful to rewrite the system in state-space and use the tools provided by LTI systems theory. The state for each spacecraft is given by the components of position and velocity in the orbiting frame  $\mathcal{F}_O$ .

$$\mathbf{x} = \begin{bmatrix} \dot{\rho}_{Sx} \\ \dot{\rho}_{Sy} \\ \dot{\rho}_{Sz} \\ \rho_{Sx} \\ \rho_{Sy} \\ \rho_{Sz} \end{bmatrix} \quad \mathbf{x} \in \mathbb{R}^6 \quad (2.22)$$

The equation of motion in state-space form is:

$$\dot{\mathbf{x}} = [A]\mathbf{x} + [B]\mathbf{u} \quad (2.23)$$

Where:

$$[A] = \begin{bmatrix} 0 & 2\omega_O & 0 & 3\omega_O^2 & 0 & 0 \\ -2\omega_O & 0 & 0 & 0 & 0 & 0 \\ 0 & 0 & 0 & 0 & 0 & -\omega_O^2 \\ 1 & 0 & 0 & 0 & 0 & 0 \\ 0 & 1 & 0 & 0 & 0 & 0 \\ 0 & 0 & 1 & 0 & 0 & 0 \end{bmatrix} \quad [B] = \frac{1}{m_S} \begin{bmatrix} 1 & 0 & 0 \\ 0 & 1 & 0 \\ 0 & 0 & 1 \\ 0 & 0 & 0 \\ 0 & 0 & 0 \\ 0 & 0 & 0 \end{bmatrix} \quad \mathbf{u} = \begin{bmatrix} F_{CSx} \\ F_{CSy} \\ F_{CSz} \end{bmatrix} \quad (2.24)$$

The stability of the system is determined by the eigenvalues  $\lambda$  of the state matrix  $[A]$ .

$$\lambda([A]) = \begin{bmatrix} 0 \\ 0 \\ -\omega_O i \\ -\omega_O i \\ \omega_O i \\ \omega_O i \end{bmatrix} \quad (2.25)$$

All the eigenvalues  $\lambda$  lies on the imaginary axis and thus the system is at the stability boundary. Furthermore, the zero-valued eigenvalues produce a constant drift term (i.e. a secular motion is expected to appear in the solution).

In addition, the linearization has decoupled the out-of-plane, cross-track motion from the in-plane motion. The cross-track motion is a simple harmonic oscillator.

On the other hand, the transverse and along-track drift components, varying linearly with time, implies that the in-plane relative positions will diverge.

The spacecrafts need to fly in formation in order to meet the optical criteria and work as sub-aperture patches, a control action is thus needed to achieve and keep the desired formation. A formation-flying control strategy is implemented in the DSENDSEdu simulator in chapter 5. In order to apply modern state-space based control strategies such as LQR, matrices  $\{A, B\}$  must constitute a controllable pair. For linear systems, the controllability can be assessed using the Kalman rank condition (i.e. the controllability matrix must be full rank). The controllability matrix is defined as:

$$[K] = [[B] [A][B] [A]^2[B] \dots [A]^5[B]] \quad (2.26)$$

Matrix  $[K]$  is full rank, hence the system is fully controllable (i.e. there exists a control action that can bring in finite time the state to the origin from every point in the state space).

## 2.0.4 Spacecraft attitude dynamics and control problem

Each spacecraft is assumed to be actuated along its three principal axis and it is therefore possible to fully control its attitude. The rotational equations of motion of a rigid body are decoupled from the translational ones if they are formulated with respect to a frame whose origin coincides with the center of mass [14, 15]. The rotational dynamics is described through the rate of change of the angular momentum, in coordinate-free form the inertial derivative of the angular momentum is:

$$\dot{\underline{\mathbf{h}}}^I = \underline{\boldsymbol{\tau}} \quad (2.27)$$

$\underline{\boldsymbol{\tau}}$  consists of all the external torques applied (i.e. possible torque disturbances and control actions). Since the body-fixed reference frame  $\mathcal{F}_S$  is located at the center of mass of the spacecraft, the angular momentum is  $\underline{\mathbf{h}} = \underline{\mathbf{J}}^I \underline{\boldsymbol{\omega}}^S$  where  $\underline{\mathbf{J}}$  is the inertia dyadic with respect to the center of mass and  $\underline{\boldsymbol{\omega}}^S$  is the angular velocity of the spacecraft body-fixed reference frame  $\mathcal{F}_S$  with respect to the inertial reference frame  $\mathcal{F}_I$ . Equation 2.27 can be reformulated taking derivatives with respect to the body-fixed frame  $\mathcal{F}_S$  using again the Transport Theorem.

$$\dot{\underline{\mathbf{h}}}^S + \underline{\boldsymbol{\omega}}^S \times \underline{\mathbf{h}} = \underline{\boldsymbol{\tau}} \quad (2.28)$$

Projecting equation 2.28 in  $\mathcal{F}_S$ :

$$\mathcal{F}_S^T \dot{\underline{\mathbf{h}}} + \mathcal{F}_S^T [\underline{\boldsymbol{\omega}}^S]^\times \underline{\mathbf{h}} = \mathcal{F}_S^T \underline{\boldsymbol{\tau}} \quad (2.29)$$

To avoid confusion  ${}^I\boldsymbol{\omega}^S$  will be called  $\boldsymbol{\omega}$  in the following equations. Then, simplyfing  $\mathcal{F}_S$  from both sides and using the definition of angular momentum:

$$[J]\dot{\boldsymbol{\omega}} = [\boldsymbol{\omega}]^\times [J]\boldsymbol{\omega} + \boldsymbol{\tau} \quad (2.30)$$

Equation 2.30 is the Euler equation describing the rotational dynamics of a rigid body, by integrating it the components of the angular velocity in the spacecraft frame  $\mathcal{F}_S$  can be obtained. However, to control the attitude the angular velocity must be related to an attitude metric. The unit quaternions metric will be used for its computational speed and its singularity free property. The quaternion  ${}^I\mathbf{q}_S$  is defined to describe the orientation of frame  $\mathcal{F}_S$  with respect to the inertial frame  $\mathcal{F}_I$ . It is possible to define a linear map to relate  ${}^I\mathbf{q}_S$  and its inertial time derivative  ${}^I\dot{\mathbf{q}}_S$  that depends on the angular velocity expressed in body frame  $\boldsymbol{\omega}$ .

$${}^I\dot{\mathbf{q}}_S = \frac{1}{2}[G(\boldsymbol{\omega})] {}^I\mathbf{q}_S = \frac{1}{2} \begin{bmatrix} 0 & \omega_3 & -\omega_2 & \omega_1 \\ -\omega_3 & 0 & \omega_1 & \omega_2 \\ \omega_2 & -\omega_1 & 0 & \omega_3 \\ -\omega_1 & -\omega_2 & -\omega_3 & 0 \end{bmatrix} {}^I\mathbf{q}_S \quad (2.31)$$

Equations 2.30 and 2.31 fully describe the rotational dynamics of the spacecraft with respect to the inertial frame  $\mathcal{F}_I$ . They will be used in the chapter 5 to derive an attitude control law for the spacecraft formation at the macro-scale.

## 2.0.5 Equation of motion of the cloud particle P relative to Spacecraft S

The equation of motion of the particle P is formally identical to the one of the spacecraft S when they are both referred to the inertial reference frame  $\mathcal{F}_I$ . For the time being, the mutual gravity between the two bodies (i.e. spacecraft and cloud particle) is neglected and it is assumed that the particle can be trapped through the force  $\mathbf{F}_{CP}$ . Furthermore, the particle is subjected to the gravitational field imposed by the primary body, that is assumed spherical.

$$\ddot{\mathbf{r}}_P = -\frac{\mu\mathbf{r}_P}{\|\mathbf{r}_P\|^3} + \frac{\mathbf{F}_{CP}}{m_P} \quad (2.32)$$

Equation 2.32 can be rearranged to describe the dynamics of the particle with respect to  $\mathcal{F}_S$  (i.e. the spacecraft body-fixed frame) that is rotating with angular velocity  ${}^I\boldsymbol{\omega}^S$  with respect to frame  $\mathcal{F}_I$ . This transformation is needed because the control, sensing and actuation system of the cloud will be on-board of S, as a consequence, the dynamics that is 'seen' by the control system is the one relative to  $\mathcal{F}_S$ . Differentiating

equation 2.3 twice with respect to  $\mathcal{F}_I$  and substituting equation 2.32 and 2.4, the relative dynamics with inertial derivatives is:

$$\underline{\underline{\rho}}_P^I = -\mu \left[ \frac{\underline{\underline{r}}_P}{\|\underline{\underline{r}}_P\|^3} - \frac{\underline{\underline{r}}_S}{\|\underline{\underline{r}}_S\|^3} \right] + \frac{\underline{\underline{F}}_{CP}}{m_P} - \frac{\underline{\underline{F}}_{CS}}{m_S} \quad (2.33)$$

In equation 2.33, the coupling between spacecraft and particle relative dynamics is due to the differential gravity term (i.e. they are on different orbits with respect to the primary body) and to the control forces applied to the spacecraft (i.e.  $\underline{\underline{F}}_{CS}$ ). The second source of coupling is purely caused by the relative nature of this equation of motion. The final step to obtain the relative dynamic is to transport the inertial derivative on the left-hand side of equation 2.33 in the body-fixed spacecraft frame  $\mathcal{F}_S$ .

$$\underline{\underline{\rho}}_P^{SS} = -{}^I\underline{\underline{\dot{\omega}}}^S \times \underline{\underline{\rho}}_P - 2{}^I\underline{\underline{\omega}}^S \times \underline{\underline{\rho}}_P^S - {}^I\underline{\underline{\omega}}^S \times {}^I\underline{\underline{\omega}}^S \times \underline{\underline{\rho}}_P + \frac{\underline{\underline{F}}_{CP}}{m_P} - \frac{\underline{\underline{F}}_{CS}}{m_S} \quad (2.34)$$

In equation 2.34, the additional Euler term proportional to the angular acceleration  ${}^I\underline{\underline{\dot{\omega}}}^S$  is present. The dot is used to underline the fact that the derivative of the angular velocity is the same if taken with respect to  $\mathcal{F}_I$  or  $\mathcal{F}_S$  [14]. The relative dynamics in equation 2.34 can be simplified considering that  $m_P \ll m_S$  and that  $\|{}^I\underline{\underline{\omega}}^S\|$  is very small. The assumption on the angular velocity depends on the bandwidth of the attitude control system of the spacecraft compared to the speed of the control system used for the single grains. This assumption will be verified in chapter 5. Then the dynamic equation can be rewritten as:

$$\underline{\underline{\rho}}_P^{SS} = \frac{\underline{\underline{F}}_{CP}}{m_P} \quad (2.35)$$

The centrifugal, Coriolis and Euler term that express the non inertial nature of the spacecraft body-fixed frame  $\mathcal{F}_S$  are neglected together with the coupling term introduced by the forces applied to the spacecraft  $\underline{\underline{F}}_{CS}$ . Equation 2.35 is a double-integrator system where the specific structure of the equation depends on the nature of the control actions  $\underline{\underline{F}}_{CP}$ .

# Chapter 3

## Laser interaction and control

The explicit form of equation 2.35 depends on the nature of the actuation considered. The simplifications adopted due to the large difference in the dynamics allow to study the interaction with the control force as if the equations were formulated with respect to a fixed inertial frame. In this chapter, the possibility of controlling the granular particles with laser pressure is considered. The laser source is assumed fixed with the inertial frame while the particle is free to move in space. The aim of the control strategy is to control alignment and position of the particles. A laser-particle interaction model is analysed and the dynamic response is studied for the in-plane case. Two different situations are considered, the single and multiple realignment towards the laser light direction for particles with one degree of freedom and the position and alignment control for a particle free to move in the 2D plane.

### 3.1 Actuator model and assumptions

Photons carry momentum that can be used to control and manipulate microscopic and mesoscopic particles. This is an established technology in biology through the use of optical tweezers. Previous research [28, 18, 25] has studied the modeling and control of micrometric dielectric particles using laser radiation pressure. In addition, its application to trap multiple mesoscopic particles to shape surfaces that can behave as optical mirrors [12] has been experimentally achieved. An optical membrane of noncontacting micrometric particles is created based on the trapping and binding forces. In this study, Maxwell's equations are solved and the mutual interactions between the particles is taken into account to achieve close packing. The modeling of the interaction with the laser source depends closely on the level of accuracy needed and the behaviours that are considered. The wavelength of the laser source  $\lambda$ , its spatial distribution around the beam axis, the size and shape of

the objects to be manipulated play a fundamental role in this choice. It is extremely difficult to develop a dynamic formulation for the mutual interactions between the particles that can be used from the control point of view.

In general, considering a laser source investing a spherical particle, the model adopted changes as a function of the ratio between wavelength and the dimension of the particle  $\frac{d}{\lambda}$  [11]. When  $\frac{d}{\lambda} \gg 1$  (*Regime 1*) the interactions phenomena are described from the ray optics perspective. While when  $\frac{d}{\lambda} \ll 1$  (*Regime 2*) the light's electric field imparts an oscillating electric dipole moment on the particle. The dipole is then attracted to the point of highest intensity gradient. Therefore, on a spherical particle subjected to a non uniformly distributed laser beam two main forces are present. A scatter force in the direction of the beam axis and a 'restoring' or gradient force lying in a perpendicular plane with respect to the scatter force. Thus, the particle is controlled by landscaping the intensity of the optical field resulting a spring-like behaviour in the neighbourhood of optical potential wells. This phenomenon is used in optical tweezers technology usually using Gaussian beams and a damping medium such as water.

### 3.1.1 Ray-tracing model

In this dissertation, it is assumed to work in *Regime 1*, the particle to be controlled will be modeled as a micrometric object thus the laser's wavelength  $\lambda$  must be in the nanometer scale for this model to hold. This is a typical range for commercial diode pumped solid state sources. Furthermore, the spatial distribution is considered approximately constant (i.e. flat top distribution or quasi-uniform illumination) and the source's diameter much greater than the characteristic dimension of the particle. As a consequence, in this condition, it is the specific shape of the particle that determines its dynamic response to the incident light field. A stable rotational equilibrium with light-source facing orientation can be obtained with specific engineered shaping of the particle. These characteristics have been studied to eventually control orientation of solar sails [2]. It has been shown that an hemispherical object with a reflective coating will experience a restoring torque towards the light direction [2]. A ray-tracer model can be used to approximately calculate the light-matter interaction [3]. The light beam is divided in a set of rays and the contribution to the momentum transfer is calculated for each ray. A certain number of reflections is considered. All the rays contributions are then summed and the resulting force is computed. A uniform laser beam exert forces and torques similar to aerodynamic interactions in airfoils [3, 18]. Following this analogy, the radiation pressure is integrated over the surface to obtain an overall force applied to an equivalent center of pressure. The offset between this point and the center of mass of the hemispheric particle generates an optical torque. The fundamental difference between the optical

tweezers is that the forces other than the scatter one are due to the specific shape of the object and not to the spatial distribution of the light field.

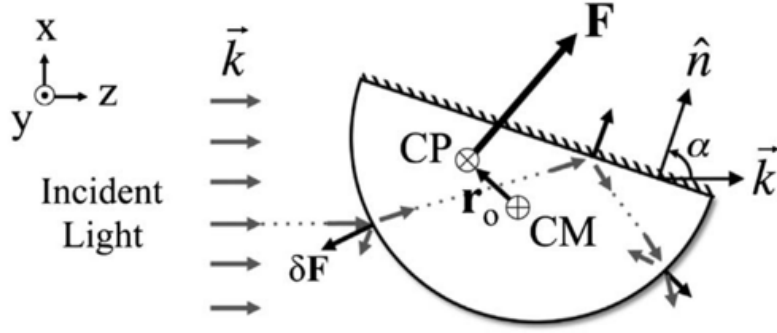


Figure 3.1: Resultant forces using the ray-tracing model, reproduced from [2]

Considering a hemispherical particle, the interaction can be described decomposing the generalized force in three main contributions. A scatter force in the direction of the propagating light. An optical lift force in a direction transverse to the previous one. Finally, an optical torque perpendicular both to the scatter and lift forces. The entity of these forces depends on the angle of attack ( $\alpha$  in Figure 3.1) that is the angle formed by the light direction with the normal vector to the flat surface. It is straightforward to notice that, due to symmetry, the laser light on axisymmetric objects determines in-plane translation and rotation on a plane perpendicular to the direction of the optical torque. Therefore, in the following, the problem will be modeled as two dimensional. It is possible to define equivalent efficiency coefficients  $Q_i$  that quantifies the 'distance' in terms of fraction of light reflected with respect to a perfect mirror with normal incidence. The intensity of force and torque acting on the particle as a function of the angle of attack can be written in terms of these dimensionless efficiency coefficients. The angle of attack is here denoted by  $\phi$ .

$$T = \frac{\pi r^3}{c} Q_t(\phi) I_{laser} \quad F_d = \frac{\pi r^2}{c} Q_d(\phi) I_{laser} \quad F_l = \frac{\pi r^2}{c} Q_l(\phi) I_{laser} \quad (3.1)$$

The efficiency coefficients in equation 3.1 are obtained normalizing the force or torque by the speed of light  $c$ , the light intensity  $I$  and a characteristic dimension  $r$  (in this case the radius of the hemisphere). The values for a refractive hemisphere with mirrored flat surface are numerically obtained in [3]. The torque and lift coefficients are odd function of the angle of attack, while the drag one is even. For this reason, only the range between 0 and 180 degrees is plotted below.

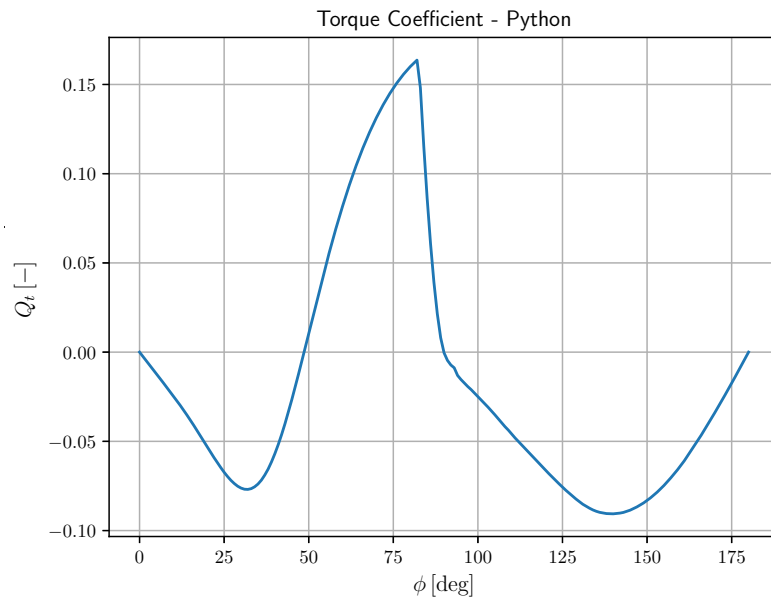


Figure 3.2: Torque Efficiency Coefficient

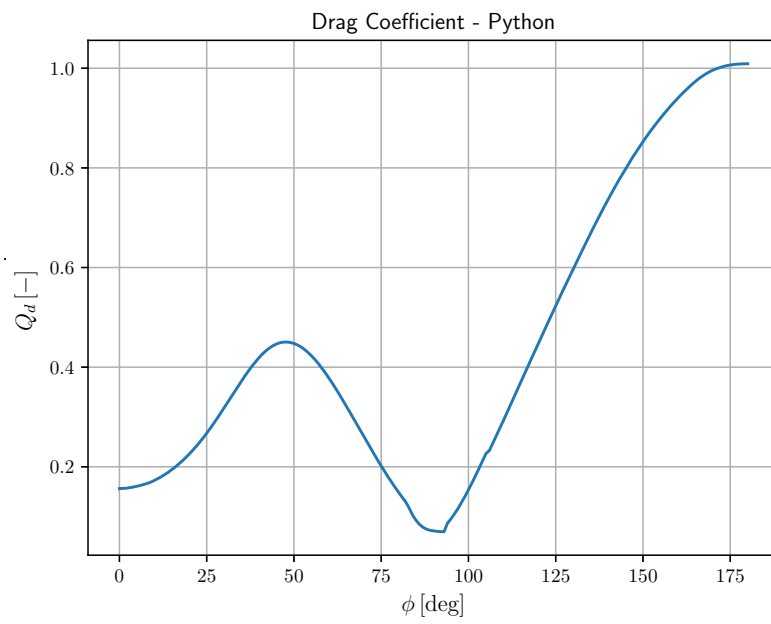


Figure 3.3: Drag Efficiency Coefficient

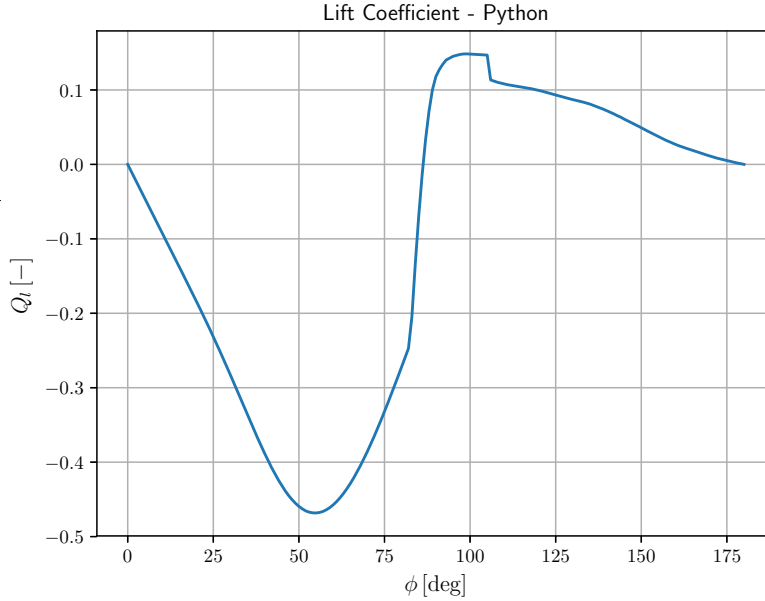


Figure 3.4: Lift Efficiency Coefficient

### 3.1.2 Actuators layout and particle properties

The modeling layout described above is used to derive control laws for the particles that compose the aperture of the Granular Imager. The quantitative knowledge of the efficiency coefficients allows to describe the laser-particle interaction so that a dynamic model useful from the control point of view can be analysed. The object to be manipulated is modeled as a micrometric glass hemisphere with properties shown in table 5.5. The light source is fixed with the spacecraft body-fixed frame  $\mathcal{F}_S$  and the light beam is oriented along the x-axis, due to the assumptions made in the previous sections this frame will be considered inertially fixed for the rest of the chapter. In the DSENDSEdu simulation in chapter 5 the coupling effects will be studied and the validity of this assumption proven. The body frame of the hemisphere is oriented along the principal axis of inertia with the x-axis oriented as the normal vector to the flat surface. As a consequence, the matrix describing the components of the inertia tensor resolved in this frame does not present diagonal terms and due to symmetry  $J_y = J_z$ .

Symbol	Property	Value	Units
r	radius	$2.5 \cdot 10^{-6}$	m
$\rho$	density	1060	$\frac{\text{Kg}}{\text{m}^3}$
m	mass	$3.47 \cdot 10^{-14}$	Kg
$J_x$	inertia component	$8.67 \cdot 10^{-26}$	$\text{Kg} \cdot \text{m}^2$
$J_z$	inertia component	$5.62 \cdot 10^{-26}$	$\text{Kg} \cdot \text{m}^2$

Table 3.1: Particle physical properties

The control problem for a single particle has been studied in [18, 28], in their dissertations PID control laws for orientation and position control along one axis have been successfully applied. In the following part instead, nonlinear control strategies will be derived for particle realignment and full position control with different layout of the sources. Compared with the previous techniques, this architecture allows to take explicitly into account the intrinsic nonlinearity of the system and achieve better performance with orders of magnitude less intensity values.

## 3.2 Hemisphere 1DOF rotational model

In this section, the in-plane rotational dynamics of the particle subjected to radiation pressure is analysed. Figure 3.2 shows a sketch of the one dimensional model. Considering the angle of attack  $\phi$  as the generalized angular coordinate to formulate the equation of motion, it is straightforward to notice that the nonlinearity is introduced by the efficiency coefficient  $Q_t(\phi)$ .

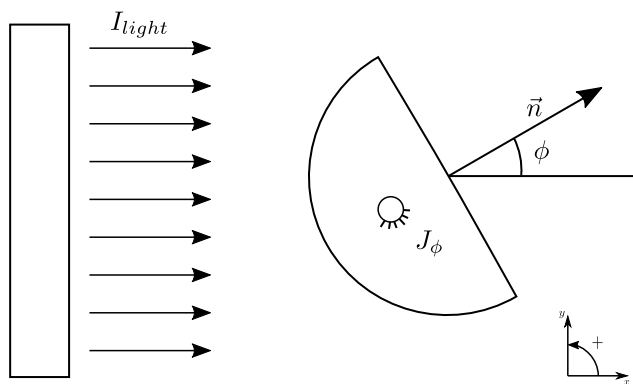


Figure 3.5: System schematics

The rotational equation of motion is simply:

$$J_z \ddot{\phi} = T \quad (3.2)$$

Where  $T$  is the optical torque described in the previous section and  $J_z$  the inertia component along the z-axis. Equation 3.2 can be rewritten by expanding the torque  $T$  as:

$$J_z \ddot{\phi} = \frac{\pi r^3}{c} Q_t(\phi) I_{light} \quad (3.3)$$

Considering  $I_{light}$  as a non-negative constant input  $I_{ref}$ , the equilibrium points of the system are given by the roots of the torque coefficient function  $Q_t(\phi)$ .

### 3.2.1 Structure and stability

The stability of the equilibrium points of the system when forced with constant light intensity can be studied using Lyapunov's indirect method. Equation 3.3 is rewritten in state space as:

$$\dot{\mathbf{x}} = \begin{bmatrix} I_{ref} K_t Q_t(\phi) \\ \dot{\phi} \end{bmatrix} = \mathbf{f}(\mathbf{x}) \quad (3.4)$$

Where  $K_t = \frac{\pi r^3}{c J_z}$  and the state vector  $\mathbf{x} = \begin{bmatrix} \phi \\ \dot{\phi} \end{bmatrix}$ . The equilibrium points are computed from the roots of the nonlinear algebraic equation:

$$\mathbf{f}(\mathbf{x}_0) = \mathbf{0} \quad (3.5)$$

The linearization around the equilibrium points is obtained as:

$$\Delta \mathbf{x} = \begin{bmatrix} \dot{\phi} - \dot{\phi}_{eq} \\ \phi - \phi_{eq} \end{bmatrix} \quad \Delta \dot{\mathbf{x}} = \left. \frac{\partial \mathbf{f}(\mathbf{x})}{\partial \mathbf{x}} \right|_{\mathbf{x}=\mathbf{x}_{eq}} \Delta \mathbf{x} \quad (3.6)$$

The stability of the linearized system depends on the real part of the eigenvalues of the state-matrix:

$$\left. \frac{\partial \mathbf{f}(\mathbf{x})}{\partial \mathbf{x}} \right|_{\mathbf{x}=\mathbf{x}_{eq}} = \begin{bmatrix} 0 & I_{ref} K_t \frac{\partial Q_t(\phi)}{\partial \phi} \Big|_{\phi=\phi_{eq}} \\ 1 & 0 \end{bmatrix} \quad \lambda_{1,2} = \pm \sqrt{I_{ref} K_t \frac{\partial Q_t(\phi)}{\partial \phi} \Big|_{\phi=\phi_{eq}}} \quad (3.7)$$

Thus the stability condition for the linearized system is:

$$Re[\lambda_{1,2}] \leq 0 \iff \left. \frac{\partial Q_t(\phi)}{\partial \phi} \right|_{\phi=\phi_{eq}} \leq 0 \quad (3.8)$$

If condition in equation 3.8 is verified the eigenvalues can only lay on the imaginary axis, the system is stable but not in an asymptotic sense, this is due to the absence of a damping term in the dynamic equation. The linearized system is a stable simple harmonic oscillator but nothing can be concluded on the stability of the nonlinear system according to Lyapunov's theorem due to the fact that the linearized system is not asymptotically stable. The frequency of the oscillation of the linearized system around the zero equilibrium depends on the properties of the particle and on the reference intensity  $I_{ref}$ .

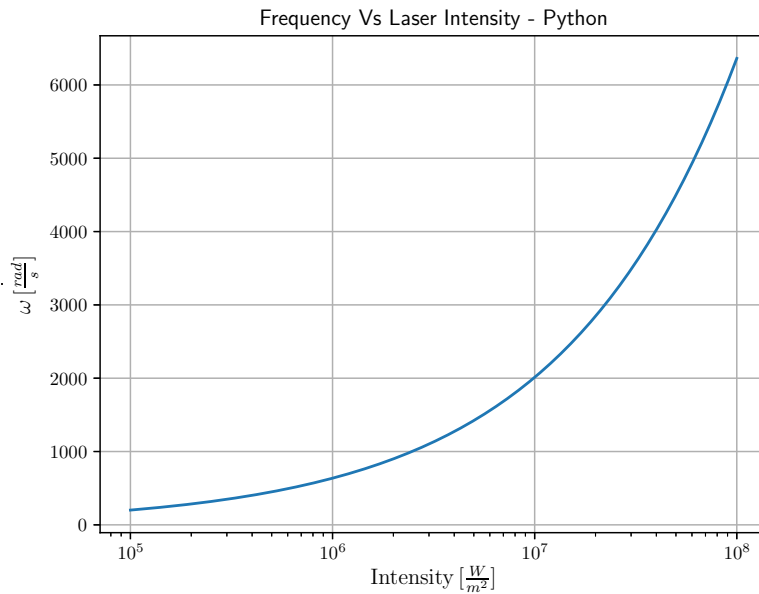


Figure 3.6: Linearized system natural frequency

The nonlinear system is numerically integrated and its behaviour is compared to its linear stable approximation in the neighbourhood of the equilibrium point. The nonlinear equation of motion is solved in a Python script, the integrator used is the Scipy LSODA that provides automatic stiffness detection and switching. The initial angular position is at  $10 [deg]$  with zero angular velocity. The laser intensity is  $10^6 [\frac{W}{m^2}]$ . As expected the natural frequency is  $\omega_0 \approx 600 [\frac{rad}{s}]$ . The dynamic responses are similar thus the linearized system can be considered a good approximation and the origin a locally stable equilibrium point.

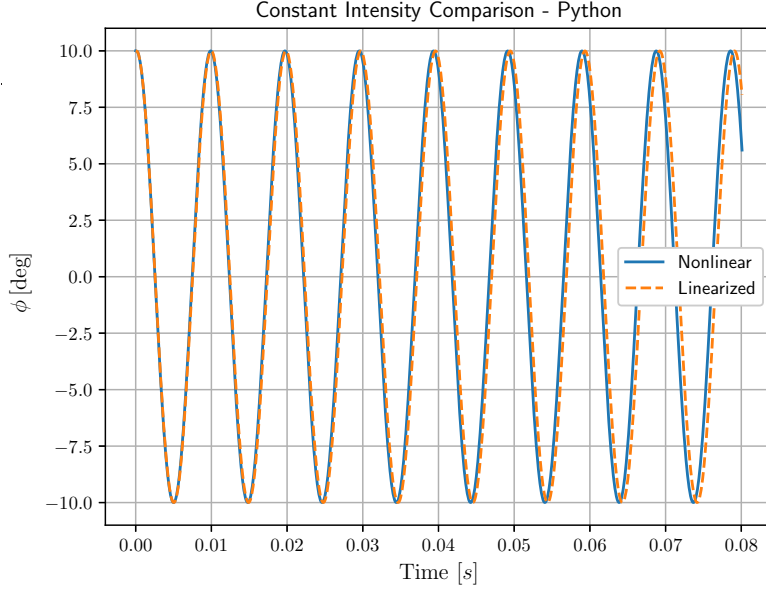


Figure 3.7: Constant Intensity - Linear Vs Nonlinear

### 3.3 Control strategies for the 1DOF model

The equation of motion 3.9 can be reformulated considering the light intensity as a non-negative control input  $u = I_{light}$ :

$$\dot{\mathbf{x}} = \begin{bmatrix} u K_t Q_t(\phi) \\ \dot{\phi} \end{bmatrix} = \mathbf{f}(\mathbf{x}, u) \quad (3.9)$$

The aim of the control strategy is to realign and orient the particle around the zero equilibrium. It is easy to show that is not possible to use a linear approximation of the system around this point and use LTI theory to synthesize a control law. This is because linearizing in the state and control around the origin the contribution of the variation of the control vanishes.

$$\Delta \dot{\mathbf{x}} = \left. \frac{\partial \mathbf{f}(\mathbf{x}, u)}{\partial \mathbf{x}} \right|_{\mathbf{x}=\mathbf{0}, u=I_{ref}} \Delta \mathbf{x} + \left. \frac{\partial \mathbf{f}(\mathbf{x}, u)}{\partial u} \right|_{\mathbf{x}=\mathbf{0}, u=I_{ref}} \Delta u \quad (3.10)$$

$$\left. \frac{\partial \mathbf{f}(\mathbf{x}, u)}{\partial u} \right|_{\mathbf{x}=\mathbf{0}, u=I_{ref}} = \begin{bmatrix} \left. \frac{I_{ref} K_t}{J_\phi} Q_t(\phi) \right|_{\phi=0} \\ 0 \end{bmatrix} = \begin{bmatrix} 0 \\ 0 \end{bmatrix} \quad (3.11)$$

This is typical of nonlinear affine systems where the state dependent modulating input function is null at the equilibrium and thus the system is not controllable

in that point. Physically, no optical torque is exerted when the angle of attack is null. The possibility of using feedback linearization is studied in the next section and after some considerations a more robust geometrical control approach is implemented based on a bilinear approximation of the system.

### 3.3.1 Feedback linearization

Due to the shape of the system, assuming that the state is completely known an algebraic transformation on the control input can be performed:

$$v = uK_tQ_t(\phi) \quad (3.12)$$

Thus the system becomes:

$$\ddot{\phi} = v \quad (3.13)$$

Equation 3.13 represents the dynamics of a linear double integrator thus a PD control law can be implemented to impose the desired error dynamics. A feed-forward term can be added to track the acceleration dynamics.

$$\ddot{\phi} = v = K_p(\phi_{ref} - \phi) + K_d(\dot{\phi}_{ref} - \dot{\phi}) + \ddot{\phi}_{ref} \quad (3.14)$$

The error dynamics is thus:

$$e := \phi_{ref} - \phi \quad \ddot{e} + K_d\dot{e} + K_p e = 0 \quad (3.15)$$

Tuning the parameters  $K_d, K_p$  is possible to impose the desired error dynamics, however it assumed to be arbitrary able to choose the value of  $v$ . The actual control action  $u$  is obtained inverting equation 3.12. Nonetheless, this operation is not always possible. The problem arises at the equilibrium when  $Q_t(0) = 0$  and the system is not controllable, hence an arbitrary dynamics can not be imposed. This poses theoretical and numerical problem in the implementation of this nonlinear control technique. In addition, due to the non-negative constraint  $u > 0$  the direction in which the control torque is applied is completely determined by the sign of  $Q_t(\phi)$  (i.e. there is no control on the sign of the torque applied), constraining the error dynamics imposed by the transformed control action  $v$ . This is why the unstable equilibrium points can not be stabilized and trajectory tracking can not be achieved. These limiting factors make this control logic not particularly suitable for this case although being widely used for controlling nonlinear systems [32].

### 3.3.2 Time-optimal control

The problems of the previous sections can be overcome considering a bilinear approximation of the system. Using this approximation a geometric time-optimal approach

will be analysed based on [31]. This strategy takes directly into account the non-negativity of the control action and the behaviour of the torque coefficient in the vicinity of the origin. Furthermore, algebraic transformations or zero divisions are avoided. The control action is rewritten as a modulating function of a reference laser intensity (i.e.  $I_{light}(t) = I_{ref} u(t)$ ). The equation of motion in state-space becomes:

$$\mathbf{x} = \begin{bmatrix} \dot{\phi} \\ \phi \end{bmatrix} \quad \dot{\mathbf{x}} = \begin{bmatrix} I_{ref} u(t) K_t Q_t(\phi) \\ \dot{\phi} \end{bmatrix} = \mathbf{f}(\mathbf{x}, u) \quad (3.16)$$

It is possible to rewrite equation 3.16 to highlight that it is affine with respect to the control input:

$$\dot{\mathbf{x}} = [A]\mathbf{x} + [F(\mathbf{x})]u \quad (3.17)$$

Where  $[A]$  and  $[F(\mathbf{x})]$  are:

$$[A] = \begin{bmatrix} 0 & 0 \\ 1 & 0 \end{bmatrix} \quad [F(\mathbf{x})] = \begin{bmatrix} I_{ref} K_t Q_t(\phi) \\ 0 \end{bmatrix} \quad (3.18)$$

The aim of the time-optimal control law is to bring the system to the origin in minimum time. However, the origin is a not controllable point for which  $[F(\mathbf{0})] = \mathbf{0}$ , this is a problem when facing the optimal control problem with an indirect approach. The Hamiltonian is:

$$H(\mathbf{x}, u, \boldsymbol{\lambda}) = 1 + \boldsymbol{\lambda}^T([A]\mathbf{x} + [F(\mathbf{x})]u) \quad (3.19)$$

if  $T$  is the minimum time solution of the problem, the optimality condition to be satisfied is:

$$H(T) = 0 \quad (3.20)$$

This must hold when the state has reached the target condition  $\mathbf{x}(T) = \mathbf{0}$ , however the Hamiltonian evaluated at the origin is:

$$H(\mathbf{x} = \mathbf{0}, u(T), \boldsymbol{\lambda}(T)) = 1 + \boldsymbol{\lambda}(T)^T[F(\mathbf{0})]u(T) = 1 \quad (3.21)$$

This is again caused by the non controllability of the system at the origin. As a consequence, a geometric direct approach will be developed starting from an approximation of the system in the neighbourhood of the origin.

### 3.3.3 Geometric control approach

It can be noticed that the torque efficiency plot is approximately linear with the angle of attack  $\phi$  in the neighbourhood of the origin  $\mathbf{x}_0 = \begin{bmatrix} 0 \\ 0 \end{bmatrix}$ , this has been proven

by the previous numerical simulation. As a consequence, a viable approximation for the the nonlinear system is a state linearization performed as follows:

$$\Delta \dot{\mathbf{x}} = \left. \frac{\partial \mathbf{f}(\mathbf{x}, u)}{\partial \mathbf{x}} \right|_{\mathbf{x}=\mathbf{x}_0} \Delta \mathbf{x} \quad (3.22)$$

The partial derivative is:

$$\left. \frac{\partial \mathbf{f}(\mathbf{x})}{\partial \mathbf{x}} \right|_{\mathbf{x}=\mathbf{0}} = \begin{bmatrix} 0 & u I_{ref} K_t \left. \frac{\partial Q_t(\phi)}{\partial \phi} \right|_{\phi=0} \\ 1 & 0 \end{bmatrix} = \begin{bmatrix} 0 & -\omega_l^2 u \\ 1 & 0 \end{bmatrix} \quad (3.23)$$

Where  $\omega_l$  is the natural frequency of the linearized system and depends on the reference intensity as shown in figure 3.6. The system in equation 3.22 can be rewritten as a bilinear system:

$$\Delta \dot{\mathbf{x}} = \begin{bmatrix} 0 & 0 \\ 1 & 0 \end{bmatrix} \begin{bmatrix} \Delta \dot{\phi} \\ \Delta \phi \end{bmatrix} + \begin{bmatrix} 0 & -\omega_l^2 \\ 0 & 0 \end{bmatrix} \begin{bmatrix} \Delta \dot{\phi} \\ \Delta \phi \end{bmatrix} u(t) = [A]\Delta \mathbf{x} + [B]\Delta \mathbf{x}u \quad (3.24)$$

In order to make the structure of the bilinear system in equation 3.24 more transparent, a simple change of variables is performed to simplify the structure of the system by introducing a normalized time variable:  $\tilde{t} = t\omega_l$  [rad]. In this way, using the chain rule it is possible to rewrite the time derivatives in equation 3.24 and define a new state vector:

$$\frac{d\Delta\phi(t(\tilde{t}))}{d\tilde{t}} = \frac{\Delta\dot{\phi}}{\omega_l} \quad \Delta \tilde{\mathbf{x}} = \begin{bmatrix} \frac{d\Delta\phi(\tilde{t})}{d\tilde{t}} \\ \Delta\phi(\tilde{t}) \end{bmatrix} \quad (3.25)$$

Equation 3.25 can be substituted in 3.24 to obtain the dynamics of the new state vector with respect to the normalized time.

$$\frac{d\Delta \tilde{\mathbf{x}}}{d\tilde{t}} = \begin{bmatrix} 0 & 0 \\ 1 & 0 \end{bmatrix} \begin{bmatrix} \frac{d\Delta\phi}{d\tilde{t}} \\ \Delta\phi \end{bmatrix} + \begin{bmatrix} 0 & -1 \\ 0 & 0 \end{bmatrix} \begin{bmatrix} \frac{d\Delta\phi}{d\tilde{t}} \\ \Delta\phi \end{bmatrix} \tilde{u}(\tilde{t}) = [A]\Delta \tilde{\mathbf{x}} + [\tilde{B}]\Delta \tilde{\mathbf{x}}\tilde{u} \quad (3.26)$$

The normalized time is measured in radians therefore the normalized angular velocity is dimensionless. The control action is derived as a function of the normalized state using a geometrical switching approach [31]. Two regions of the state-space are defined in which the control switches between 0 and 1. A control law designed in such a way takes directly into account the non-negative input constraint at which the control input is subjected. The bilinear system in 3.26 can be decomposed in two subsets as a function of the state of the control (i.e.  $u = \{0, 1\}$ ).

$$\Delta \dot{\mathbf{x}} = [A]\Delta \mathbf{x} = \begin{bmatrix} 0 & 0 \\ 1 & 0 \end{bmatrix} \begin{bmatrix} \Delta \dot{\phi} \\ \Delta \phi \end{bmatrix} \quad \text{if} \quad u = 0 \quad (3.27)$$

$$\Delta \dot{\mathbf{x}} = [(A + B)]\Delta \mathbf{x} = \begin{bmatrix} 0 & -\omega_l^2 \\ 1 & 0 \end{bmatrix} \begin{bmatrix} \Delta \dot{\phi} \\ \Delta \phi \end{bmatrix} \quad \text{if} \quad u = 1 \quad (3.28)$$

The normalization is useful because in this way, the control logic, as a function of the normalized time, is independent of the frequency  $\omega_l$  of the system. It will be shown that  $\omega_l$  is the main parameter to increase the speed of convergence to the origin of the state-space and can be increased by increasing the input light (i.e. changing the reference intensity  $I_{ref}$ ). The control action makes the overall system discontinuous, this fact poses numerical difficulties in the integration of the dynamics. Therefore, zero-crossing detection algorithms for switching systems are implemented in the Python code for the correct integration of the dynamic equations and the accurate computation of the switching instants between the two subsystems.

The subsystem in equation 3.28 behaves as a simple harmonic oscillator, as a consequence it follows circular trajectories in the phase-plane. The circular trajectories are followed at constant unitary angular velocity. On the other hand, the subsystem in equation 3.27 is a simple double-integrator without forcing term, hence it follows horizontal straight lines with direction given by the sign of the ordinate (i.e. the normalized velocity  $\frac{d\Delta\phi}{dt}$ ). The control logic modifies the control input  $u = \{0, 1\}$  as a function of the state of the system so as to reduce the distance from the origin of the state-space (i.e. phase-plane). The control law drives the state in equation 3.26 to the origin of the state-space switching between the two systems in order to reduce the distance from the origin at each cycle. The logic is geometrical in the sense that it defines the switching regions in the state-space based on the trajectories followed by the two subsystems. It builds subsequently segments of circular arcs ( $u = 1$ ) and straight constant velocity lines ( $u = 0$ ) in an appropriate way.

In order to simplify notation, in the state vector in 3.26 the delta sign is dropped

and the variables are renamed:  $\Delta \tilde{\mathbf{x}} = \begin{bmatrix} \frac{d\Delta\phi}{dt} \\ \Delta\phi \end{bmatrix} \rightarrow \tilde{\mathbf{x}} = \begin{bmatrix} \tilde{x}_1 \\ \tilde{x}_2 \end{bmatrix}$ .

The control law is designed in order to reduce the norm of the state vector  $\tilde{\mathbf{x}}$  at each cycle.

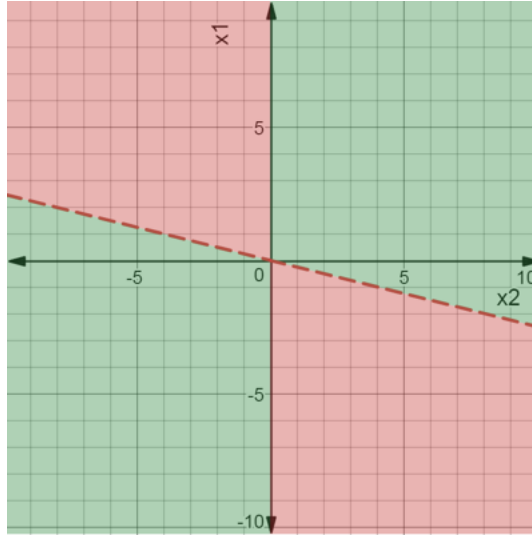


Figure 3.8: Switching Control Law

$$u(\tilde{t}) = \begin{cases} u = 1 & \text{for } \gamma\tilde{x}_2^2 + \tilde{x}_1\tilde{x}_2 > 0 \\ u = 0 & \text{else} \end{cases} \quad (3.29)$$

In figure 3.8 the switching control regions defined in 3.29 are plotted in the phase plane. The switching lines are straight lines corresponding to the vertical axis and a straight line with equation  $\tilde{x}_1 = -\gamma\tilde{x}_2$ . The control state is set to 1 in the green region while it is set to 0 in the red region. In the green region the system follows a circular clock-wise trajectory with unitary angular velocity, while in the red one the normalized velocity  $\tilde{x}_1$  is constant and the normalized position  $\tilde{x}_2$  varies at constant rate, being the system in the double-integrator region. A chattering problem occurs in the vicinity of the origin due to the fast switching, therefore a tolerance must be defined. A parameter  $\delta$  is introduced and together with the parameter  $\gamma$  it defines an accepted tolerance radius in which the norm of  $\tilde{x}$  is confined:

$$u(\tilde{t}) = \begin{cases} u = 1 & \text{for } \gamma\tilde{x}_2^2 + \tilde{x}_1\tilde{x}_2 + \delta > 0 \\ u = 0 & \text{else} \end{cases} \quad (3.30)$$

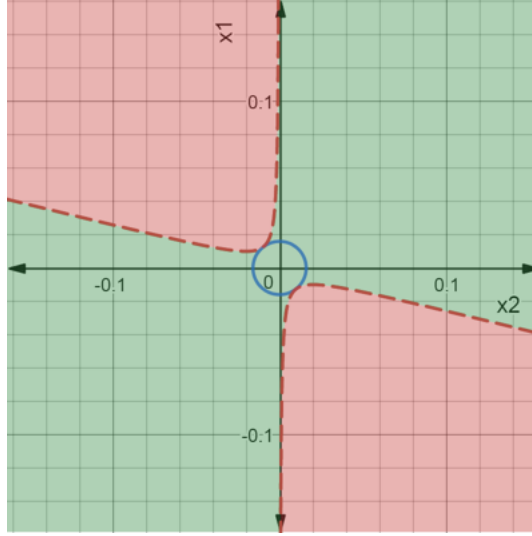


Figure 3.9: Modified Switching Control Law

In figure 3.9 the  $\delta$  parameter is set to  $10^{-4}$  while  $\gamma$  is 0.2482. The values of  $\delta$  and  $\gamma$  are fundamental parameters in the tuning of the control system given a certain reference input light  $I_{ref}$ . In particular, the value of  $\gamma$  is chosen to minimize the time of convergence to the origin [31]. In this sense the above control law is time-optimal. The tolerance confinement radius (i.e. the minimum distance between the origin and the dotted curve) can be computed analytically with a simple minimization problem. Considering the curve equation in 3.30 as a constraint the radius of the circle is calculated by finding the point lying on the curve that has minimum distance from the origin. The confinement radius is  $r = \sqrt{2\delta^2\sqrt{\frac{\gamma+1}{\delta}} + 2\gamma\delta}$ . In figure 3.9 the green and red regions are plotted together with the confinement radius  $r$ . Even if the switching curves tend asymptotically to two straight lines, in the vicinity of the origin the switching angles change slightly. Furthermore, the tuning of the confinement radius allows to reach an arbitrary distance from the origin depending on the performance specifications.

### 3.3.4 Kinematic properties of the phase-plane

The controlled switched system described in equations 3.27 and 3.28 shows an interesting kinematic property in the phase-plane. Independently of the initial conditions, the "angular" velocity at which the circular arcs of trajectory are followed in the green region is the same. Furthermore, the linear velocity in the red regions is indeed different but it is proportional to the distance to be covered. As a consequence, if the

initial state lays on the positive abscissa axis (i.e. the initial condition has zero normalized velocity and any initial position) the normalized switching times at which the control law changes between 0 and 1 can be calculated analytically as a function of the normalized time independently on the initial position. Therefore, for a given set of control parameters, theoretically, the time-optimal control law can be calculated as a feed-forward law and does not depend anymore on the state but only on the normalized time. After a complete cycle, the system intercepts the abscissa axis with a reduced angular position and zero normalized velocity, the same reasoning as for the first cycle can be repeated showing that the control law is periodic.

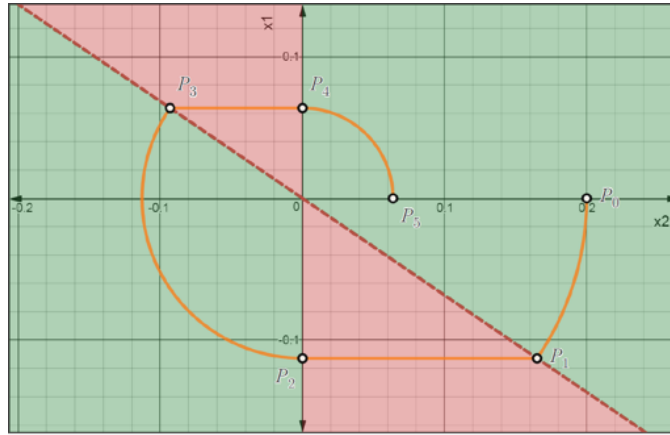


Figure 3.10: Controlled System Trajectory

In figure 3.10 the controlled state trajectory of the system is plotted with initial conditions  $\tilde{\mathbf{x}} = \begin{bmatrix} 0 \\ R_0 \end{bmatrix}$  with  $R_0 = 0.2 [rad]$ . The confinement radius is neglected and the switching lines in equation 3.29 are considered. Only a complete cycle is plotted due to the periodic nature of the switching times imposed by the control action. The following analytical derivation is valid for every cycle independent of the initial  $\tilde{x}_2$ . The time unit is the normalized time defined in the previous section and it is measured in radians. The angular velocity in the green regions is unitary, as a consequence it is easy to compute the time needed from the initial condition to reach each switching line. Note that the angle formed by the first switching line

with the abscissa axis is  $\alpha = \text{atan}(\gamma)$ . Five time intervals need to be derived:

$$\left\{ \begin{array}{ll} \Delta\tilde{T}_1 & P_0 \rightarrow P_1 \\ \Delta\tilde{T}_2 & P_1 \rightarrow P_2 \\ \Delta\tilde{T}_3 & P_2 \rightarrow P_3 \\ \Delta\tilde{T}_4 & P_3 \rightarrow P_4 \\ \Delta\tilde{T}_5 & P_4 \rightarrow P_5 \end{array} \right. \quad (3.31)$$

It is easy to see that  $\Delta\tilde{T}_1 = \alpha$  [rad]. To compute  $\Delta\tilde{T}_2$ , with basic geometrical considerations, the normalized absolute value of the velocity at  $P_1$  can be calculated as  $R_0 \sin(\alpha)$ , furthermore the distance  $D(P_1 \rightarrow P_2)$  is  $R_0 \cos(\alpha)$ . In the section between  $P_1$  and  $P_2$  the velocity is constant, as a consequence:

$$\Delta\tilde{T}_2 = \frac{D(P_1 \rightarrow P_2)}{V_{P_1 \rightarrow P_2}} = \frac{R_0 \cos(\alpha)}{R_0 \sin(\alpha)} = \cot(\alpha) [\text{rad}] \quad (3.32)$$

$\Delta\tilde{T}_3$  is simply  $\frac{\pi}{2} + \alpha$  and  $\Delta\tilde{T}_5$  is  $\frac{\pi}{2}$ . To calculate  $\Delta\tilde{T}_4$  the same reasoning as in 3.32 can be done:

$$V_{P_3 \rightarrow P_4} = R_0 \sin(\alpha)^2 \quad D(P_3 \rightarrow P_4) = R_0 \sin(\alpha) \cos(\alpha) \quad (3.33)$$

$$\Delta\tilde{T}_4 = \frac{D(P_3 \rightarrow P_4)}{V_{P_3 \rightarrow P_4}} = \frac{R_0 \cos(\alpha) \sin(\alpha)}{R_0 \sin(\alpha)^2} = \cot(\alpha) \quad (3.34)$$

The switching control law as a function of the normalized time is in fact a function of  $\alpha(\gamma)$ :

$$u(\tilde{t}) = \begin{cases} u = 1 & \text{for } \tilde{t} \in [0, \alpha] \\ u = 0 & \text{for } \tilde{t} \in [\alpha, \alpha + \cot(\alpha)] \\ u = 1 & \text{for } \tilde{t} \in [\alpha + \cot(\alpha), 2\alpha + \cot(\alpha) + \frac{\pi}{2}] \\ u = 0 & \text{for } \tilde{t} \in [2\alpha + \cot(\alpha) + \frac{\pi}{2}, 2\alpha + 2\cot(\alpha) + \frac{\pi}{2}] \\ u = 1 & \text{for } \tilde{t} \in [2\alpha + 2\cot(\alpha) + \frac{\pi}{2}, 2\alpha + 2\cot(\alpha) + \pi] \end{cases} \quad (3.35)$$

Equation 3.35 represents the switching control law for each cycle that drives the system to the origin. The normalized cycle time is  $\tilde{T}_{cycle} = 2(\alpha + \cot(\alpha)) + \pi$  [rad]. Note that the normalized cycle time is expressed in radians due to the normalization with respect to  $\omega_l$ . Assuming fixed the physical properties of the particle,  $\omega_l$  depends on the reference laser intensity used by the control input as shown in figure 3.6.

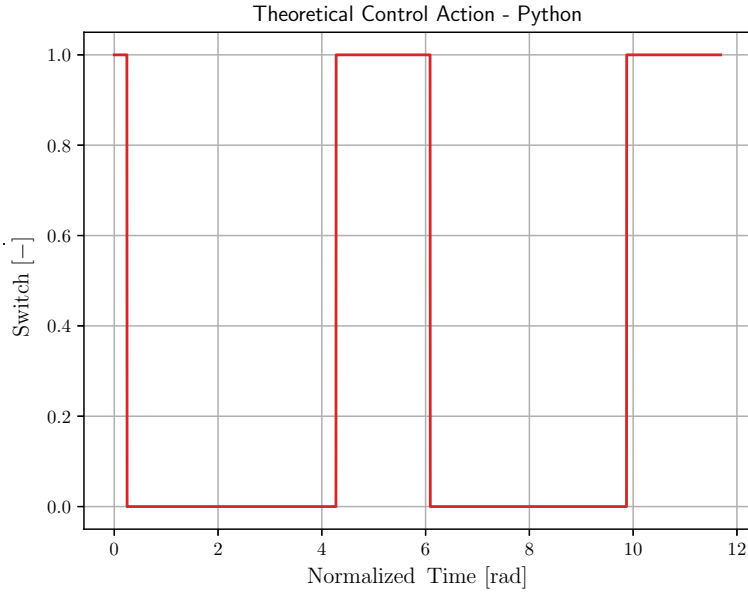


Figure 3.11: Theoretical Control Action - Python

The switching control action in figure 3.11 is independent of the specific initial angular position and thus, after a proper rescaling with the linearized natural frequency  $\omega_l$ , can be thought as a feed-forward time-optimal control law. A possible implementation of this open loop algorithm is studied in the next sections. Indeed, this algorithm requires numerically precise switching instants to avoid instability and therefore lacks robustness.

### 3.3.5 Numerical controlled response simulations

#### Bilinear system

The switching control law discussed in the previous section is now simulated on the bilinear approximation of the system. Two reference intensities are considered. The normalized switching times are rescaled accordingly. In this simulation, the control action is computed in closed-loop. Both the simulations start with zero initial angular velocity and 10 [deg] angular displacement.

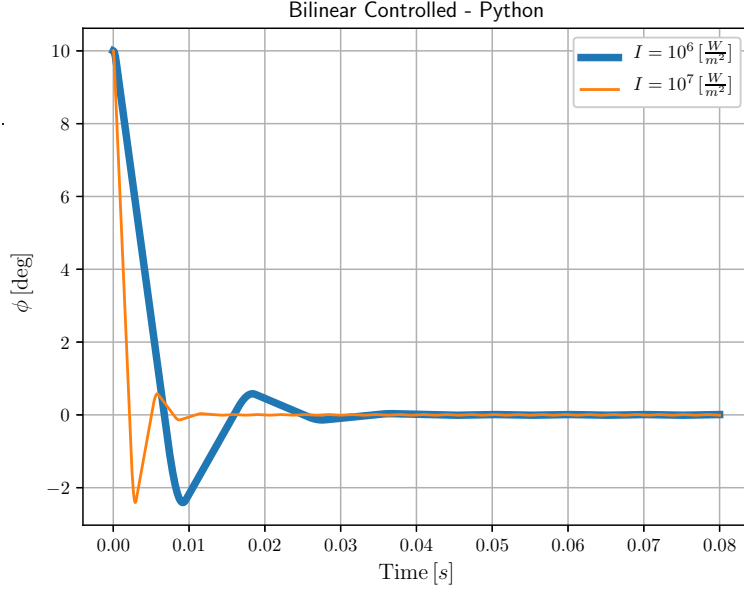


Figure 3.12: Bilinear System Controlled - Varying reference Intensity - Python

The time needed for a complete cycle is  $T_{cycle} = \frac{\tilde{T}_{cycle}}{\omega_l} [s]$ , this explains why the control law with reference intensity  $I_{ref,1} = 10^7 [\frac{W}{m^2}]$  and angular frequency  $\omega_{l,1} \approx 2000 [\frac{rad}{s}]$  is faster than the one with  $I_{ref,2} = 10^6 [\frac{W}{m^2}]$  and  $\omega_{l,2} \approx 600 [\frac{rad}{s}]$ . It is interesting to notice that they both present the same undershoot value. The faster response is simply a rescaling of the other one obtained by multiplying the time axis by  $\frac{\omega_{l,2}}{\omega_{l,1}}$ . This fact is evident if the two responses are compared in the normalized phase-plane 3.13. The velocity at which each system follows the trajectory varies as a function of the frequency (i.e. the reference intensity) but the support of the curve is always the same. This indeed holds when the angular velocity (i.e. the ordinate on the phase-plane) is normalized by the frequency. The periodic nature of the control action is evident from the control history plotted in 3.14. The time is normalized by the frequency and hence it can be noticed that the normalized switching times are periodic and identical for the two responses. This proves that the control law has the same structure independent of the frequency considered.

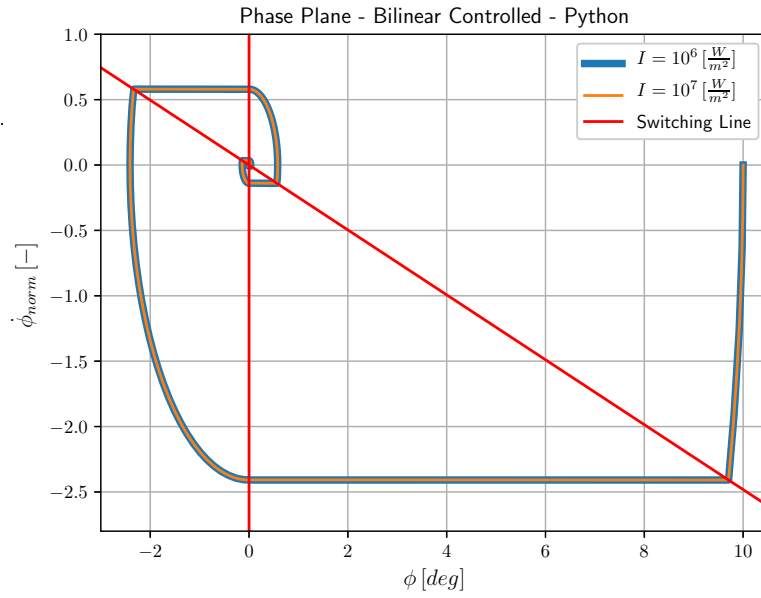


Figure 3.13: Bilinear System Controlled - Phase Plane - Python

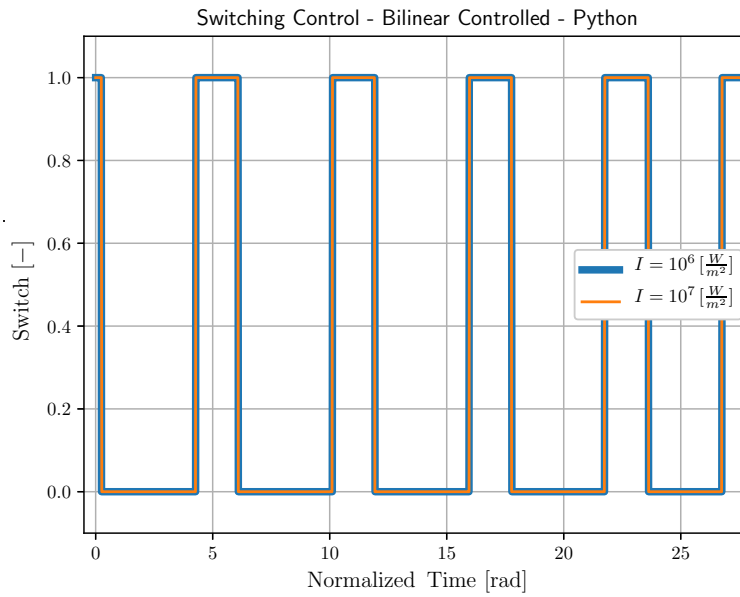


Figure 3.14: Bilinear System Controlled - Control Switch - Python

## Nonlinear system

The control strategy is simulated on the fully nonlinear system and its response is compared to its bilinear approximation. It seems reasonable to assume a linear torque coefficient in a range  $\phi \in [-30^\circ, 30^\circ]$ . The control is again computed in closed-loop as a feedback law. The reference intensity used is  $I_{ref} = 10^6 \frac{W}{m^2}$  and the initial angular position is  $30$  [deg]. The angular time histories of the two systems match almost exactly as seen in 3.15, however the control actions differ in 3.16. This shows that the bilinear behaviour approximately holds for three cycles then the nonlinearities shift the switching times. A slight change in the frequency at which the nonlinear system follows the phase-plane is due to the deviation from the linear behaviour of the torque efficiency coefficient as a function of the angular position. This problem will be analysed in detail in the next section.

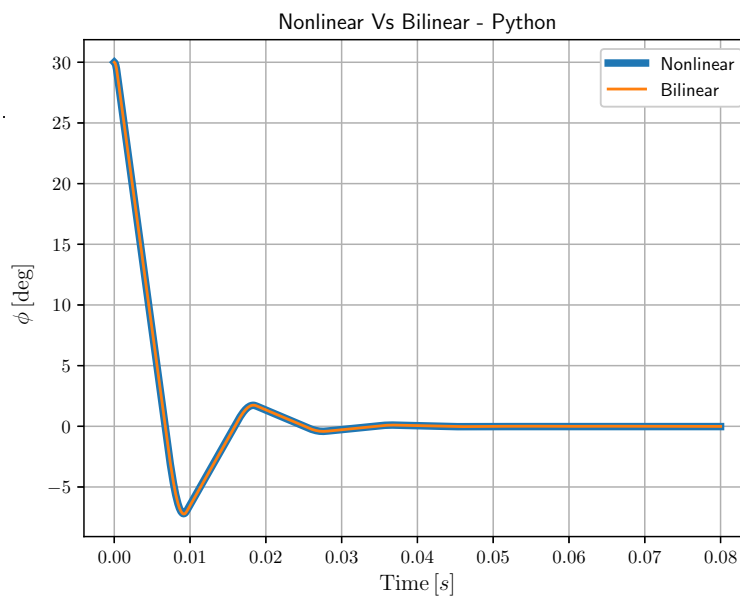


Figure 3.15: Non Linear vs Bilinear controlled response comparison

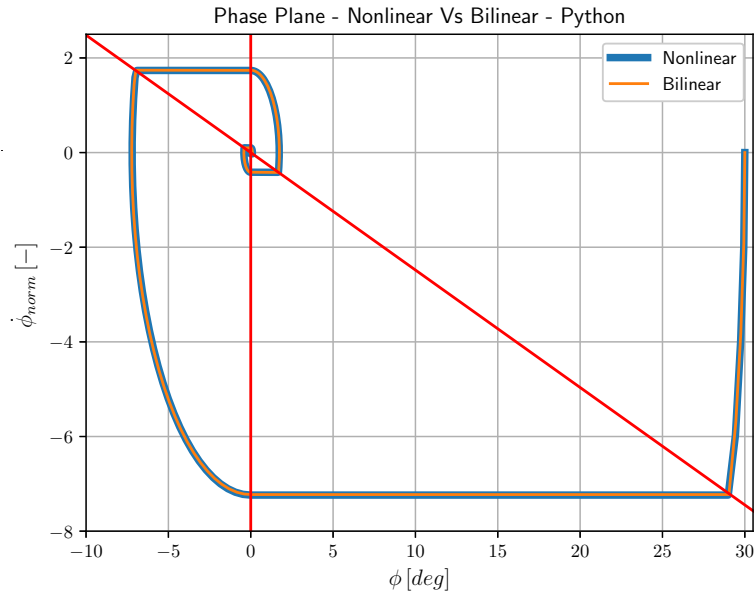


Figure 3.16: Non Linear vs Bilinear Phase Plane

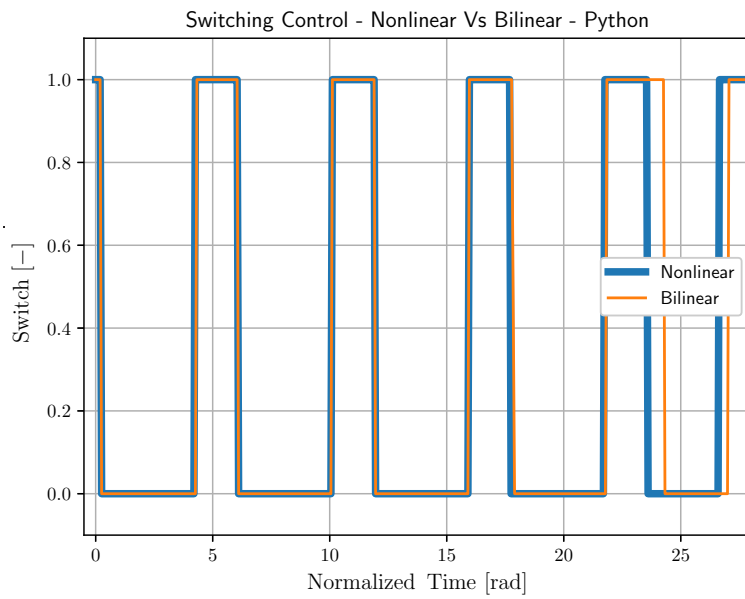


Figure 3.17: Non Linear vs Bilinear Control Law

### 3.3.6 Simultaneous single-input global control

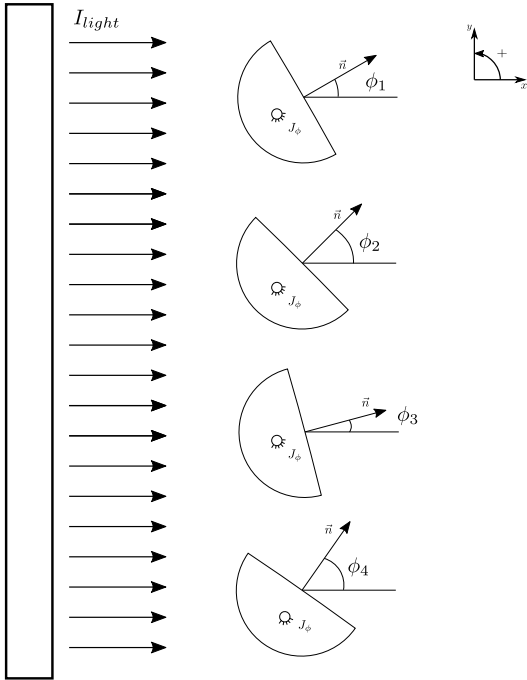


Figure 3.18: Multiple particles schematics

The useful properties of the control law derived for the bilinear system can be exploited to simultaneously control multiple identical systems. The layout is the following. A single source is the global input for multiple identical hemispheres. It is assumed that the initial velocity is zero for each elemental system and the initial angular positions are distributed around a 30 degrees range in the neighbourhood of  $\phi = 0$  [deg]. The complete system is not controllable in the classical sense. The global nature of the control action affects each subsystem differently as function of each angle of attack (i.e.  $\phi_i$ ). It is not possible to drive each angular position to a different target but in this specific condition a single switched control law of the kind developed before could theoretically drive all the different angles to zero simultaneously. This is possible thanks to the constant angular velocity at which each trajectory in the phase-plane is followed. Independently of the initial angular positions, the switching instants are the same. Therefore, an open-loop control action could drive all the substates to the origin simultaneously. An efficient numerical integration algorithm is needed to carefully compute the switching time instants and integrate each discontinuous subsystem accordingly. If the switching times are not exactly synchronized some subsystems could numerically diverge. The `assimulo` [4] Python library is used to implement an event-handler to integrate

precisely the equation of motion of the system. A system composed of  $N = 100$  identical bilinear systems is simulated in the figures below. Each subsystem is subjected to the same open-loop control action plotted in figure 3.21. The reference intensity is  $I_{ref} = 10^6 \frac{W}{m^2}$  and therefore the normalized control action is rescaled by  $\omega_l \approx 600 \left[ \frac{\text{rad}}{\text{s}} \right]$ . All the subsystems are driven to the origin simultaneously using the same global control action.

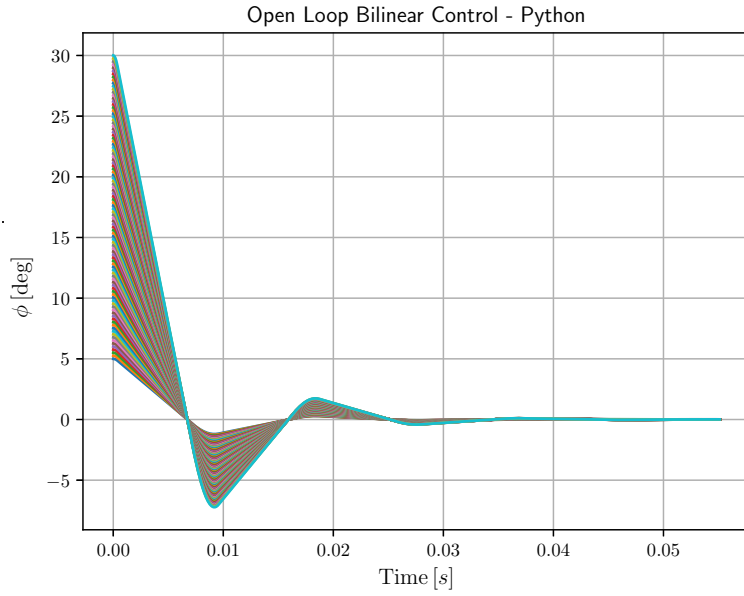


Figure 3.19:  $N=100$  identical bilinear systems simultaneous control time history

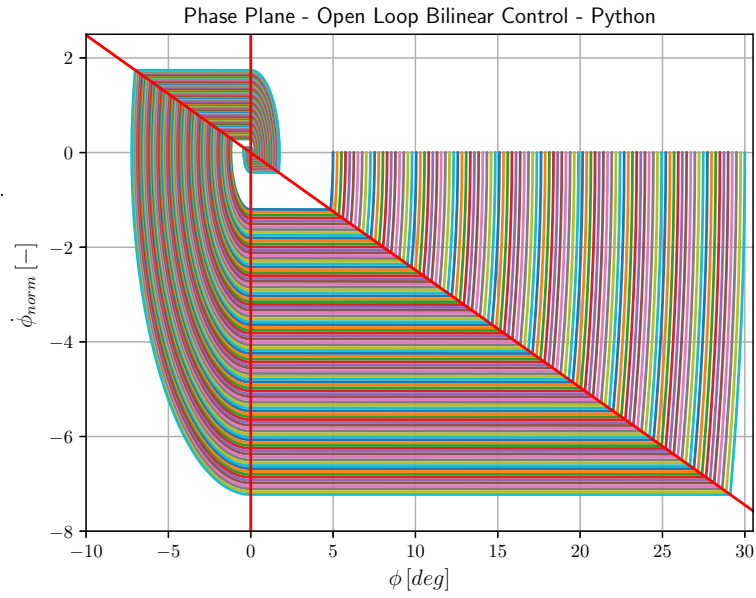


Figure 3.20: N=100 phase plane

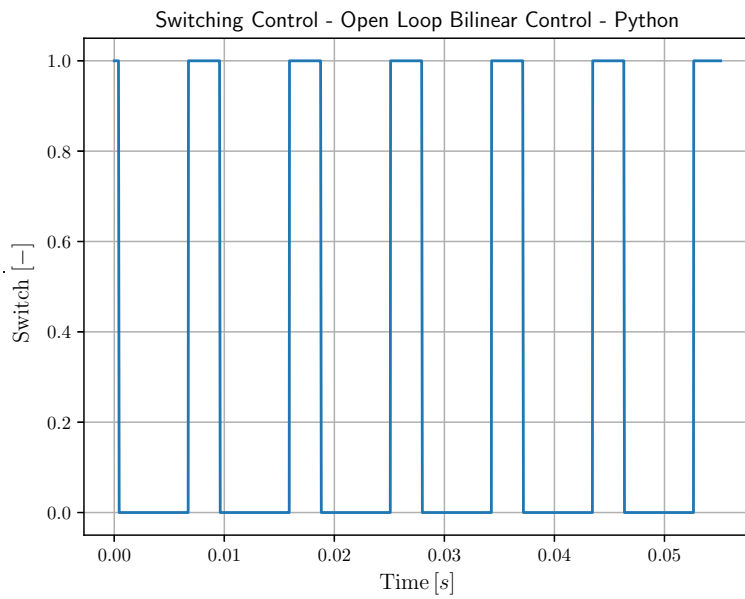


Figure 3.21: Open loop global control action

## Nonlinear system

The open-loop control law works for the bilinear approximation of the system but for this approach to hold also in the fully nonlinear case, the 'natural' frequencies must be independent of the initial conditions. From the figure below, it is evident that there is a frequency shift that is dependent on the initial conditions.

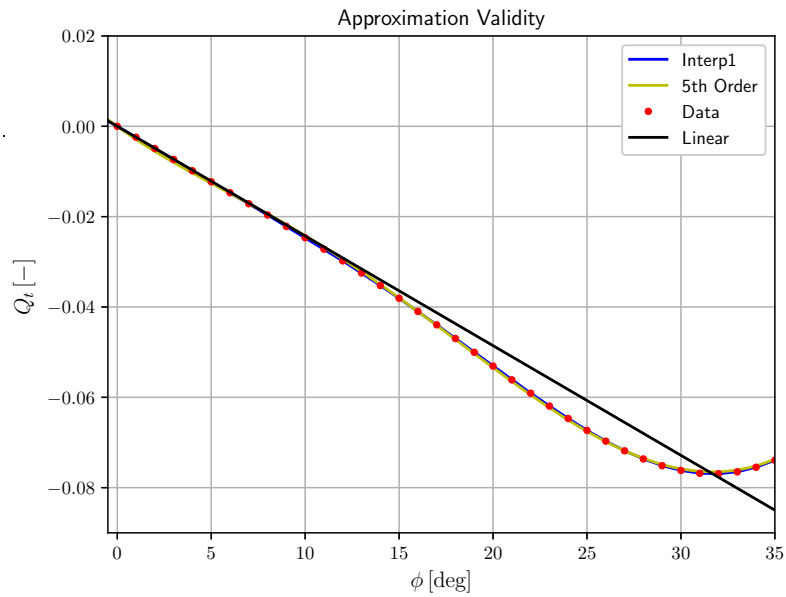


Figure 3.22: Detailed behaviour of the torque efficiency coefficient

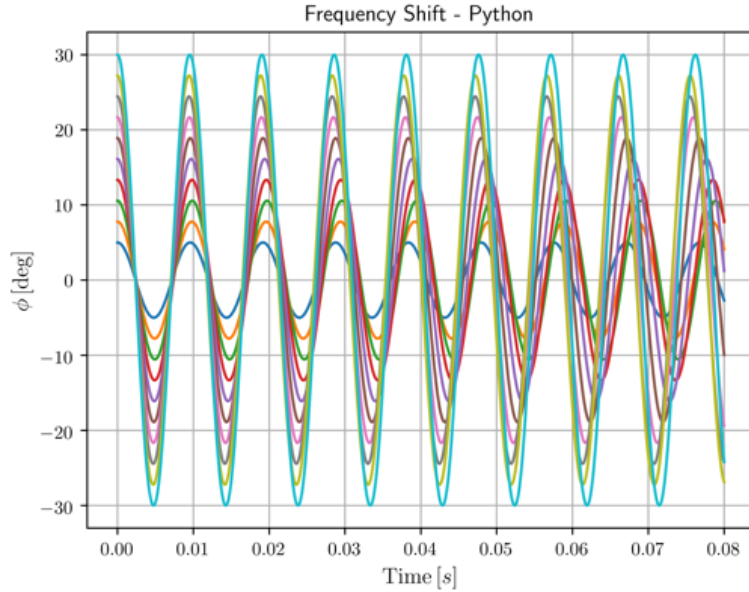


Figure 3.23: Constant input response with different initial conditions

Figure 3.22 shows the deviation from the linear behaviour when the angle of attack is above 10 [deg]. This is not a problem when there is only one particle to be controlled as shown in the previous section. The feedback nature of the control law is able to compensate this deviation and the responses were almost identical for the nonlinear system and its bilinear approximation. However, the inherent lack of robustness of an open-loop strategy does not allow to apply these techniques for the realignment of multiple particles simultaneously. A solution is to keep track of the mean state of the system and to compute a global control action based on it until a certain time threshold. The responses start to differ significantly after a fraction of the control cycle. At this point the control input is set to one. In this way, it is possible to confine the angular positions around a certain range of angles in which they continue to oscillate. This problem is solved in the DSENDSEdu simulation in chapter 5 by adding a damping medium. In the presence of rotational damping, all the particles' angular positions will converge asymptotically to the origin.

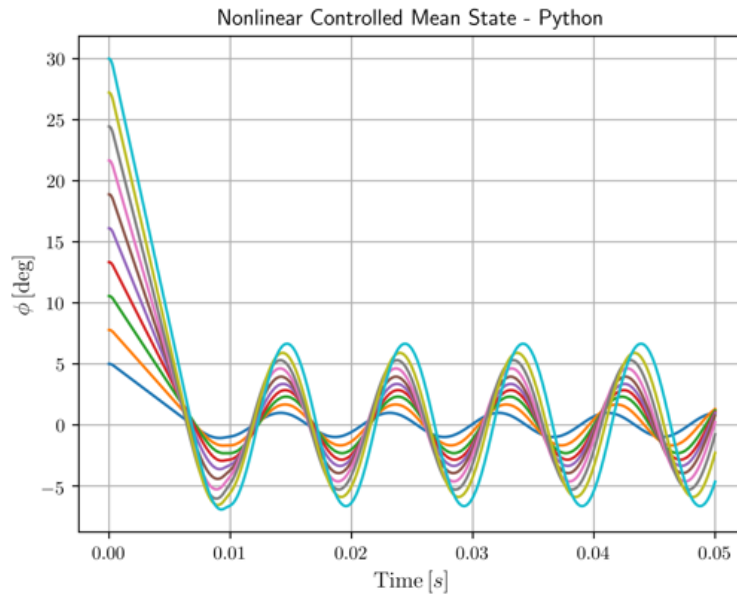


Figure 3.24: Controlled response of the nonlinear system with mean feedback

### 3.4 Hemisphere 3DOF model

The model developed in the previous section can be expanded removing the pin constraint. In so doing, the linear momentum transfer must be taken into account together with the angular one. A possible layout consists of four perpendicular actuators. It will be shown that the system is point-wise fully controllable and thus nonlinear control strategies can be implemented.

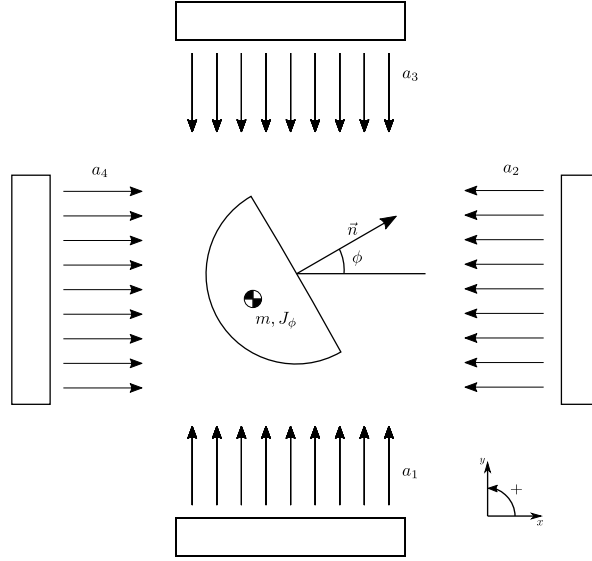


Figure 3.25: System schematics

$a_i$  is the light intensity of the  $i$ -th source,  $m$  the mass of the particle and  $J_z$  the inertia along  $z$ -axis. The laser sources are considered fixed to an inertial frame (i.e. the same assumption used for the 1DOF model). The versors defining the light direction for each source lie in the same plane. Hence, drag and lift force vectors generated by each actuator do not have out of plane components, while the torque vectors are all parallel and perpendicular to it. Therefore, a 2D model in which the particle has three degrees of freedom can be derived.

#### Translational Dynamics

The equation of motion are obtained in coordinate-free form and then projected along the inertial frame. Using Newton's second law the equation of motion is:

$$m \ddot{\mathbf{r}} = \mathbf{F}_1 + \mathbf{F}_2 + \mathbf{F}_3 + \mathbf{F}_4 \quad (3.36)$$

Where  $\mathbf{F}_i = \mathbf{F}_{di} + \mathbf{F}_{li}$  contains the effects due to drag and lift exerted by the  $i$ -source. Defining  $\hat{\mathbf{a}}_i$  the fixed versor describing the direction of the  $i$ -th laser source and  $\hat{\mathbf{a}}_{i\perp}$

as its perpendicular, obtained rotating  $\hat{\mathbf{a}}_i$  counter-clockwise, the force contribution of each laser source can be written as:

$$\underline{\mathbf{F}}_i = \underline{\mathbf{F}}_{di} + \underline{\mathbf{F}}_{li} = \frac{\pi r^2}{c} a_i (Q_{di}(\phi_i) \hat{\mathbf{a}}_i + Q_{li}(\phi_i) \hat{\mathbf{a}}_{i\perp}) \quad (3.37)$$

Where  $\phi_i$  is the angle formed by  $\hat{\mathbf{a}}_i$  and the normal vector to the flat hemisphere surface measured counter-clockwise from  $\hat{\mathbf{a}}_i$ . The vectors defined above in coordinate-free form can be projected in the inertial reference frame:

$$\begin{cases} \underline{\mathbf{r}} = \ddot{x} \hat{\mathbf{x}} + \ddot{y} \hat{\mathbf{y}} \\ \hat{\mathbf{a}}_1 = \hat{\mathbf{y}} \\ \hat{\mathbf{a}}_2 = \hat{\mathbf{x}} \\ \hat{\mathbf{a}}_3 = \hat{\mathbf{y}} \\ \hat{\mathbf{a}}_4 = \hat{\mathbf{x}} \end{cases} \quad (3.38)$$

Equation 3.37 can be substituted in 3.36, then using 3.38 equation 3.36 can be split in two second order differential scalar equations.

$$\begin{bmatrix} m\ddot{x} \\ m\ddot{y} \end{bmatrix} = \frac{\pi r^2}{c} \begin{bmatrix} -Q_l(\phi_1)a_1 - Q_d(\phi_2)a_2 + Q_l(\phi_3)a_3 + Q_d(\phi_4)a_4 \\ Q_d(\phi_1)a_1 - Q_l(\phi_2)a_2 - Q_d(\phi_3)a_3 + Q_l(\phi_4)a_4 \end{bmatrix} \quad (3.39)$$

### Rotational Dynamics

Defining  $\phi$  as the angle formed by the abscissa axis of the inertial frame with the normal vector of the hemisphere measured counter-clockwise from the x-axis, and considering it as the rotational degree of freedom, the 2D rotational dynamics can be written as:

$$J_z \ddot{\phi} = \frac{\pi r^3}{c} (Q_t(\phi_1)a_1 + Q_t(\phi_2)a_2 + Q_t(\phi_3)a_3 + Q_t(\phi_4)a_4) \quad (3.40)$$

The functions  $Q_{di}, Q_{li}$  and  $Q_{ti}$  are the same for each laser source, however the angle of attack at which they are evaluated changes.  $\phi_i$  is the relative angle of attack for each laser source and can be expressed as a function of the rotational degree of freedom  $\phi$  defined above:

$$\begin{bmatrix} \phi_1 \\ \phi_2 \\ \phi_3 \\ \phi_4 \end{bmatrix} = \begin{bmatrix} \frac{3\pi}{2} + \phi \\ \pi + \phi \\ \frac{\pi}{2} + \phi \\ \phi \end{bmatrix} \quad (3.41)$$

### 3.4.1 State-space formulation

The equations 3.39 and 3.40 are coupled by the inputs and by the angle of attack  $\phi$ . The equations can be grouped and the system rewritten in state-space:

$$\mathbf{x} = \begin{bmatrix} \dot{x} \\ \dot{y} \\ \dot{\phi} \\ x \\ y \\ \phi \end{bmatrix} \quad \mathbf{u} = \begin{bmatrix} a_1 \\ a_2 \\ a_3 \\ a_4 \end{bmatrix} \quad \dot{\mathbf{x}} = [A]\mathbf{x} + [B(\mathbf{x})]\mathbf{u} \quad (3.42)$$

Where  $\mathbf{x}$  is the state vector and  $\mathbf{u}$  the control input vector. Matrices  $[A]$  and  $[B]$  are:

$$[A] = \begin{bmatrix} [\mathbf{0}]_{3 \times 3} & [\mathbf{0}]_{3 \times 3} \\ [\mathbf{I}]_{3 \times 3} & [\mathbf{0}]_{3 \times 3} \end{bmatrix} \quad [B] = \begin{bmatrix} [\hat{B}(\mathbf{x})] \\ [\mathbf{0}]_{3 \times 4} \end{bmatrix} \quad (3.43)$$

Where  $[\hat{B}(\mathbf{x})]$  is:

$$[\hat{B}(\mathbf{x})] = \frac{\pi r^2}{c} \begin{bmatrix} -\frac{1}{m}Q_l(\phi_1) & -\frac{1}{m}Q_d(\phi_2) & \frac{1}{m}Q_l(\phi_3) & \frac{1}{m}Q_d(\phi_4) \\ \frac{1}{m}Q_d(\phi_1) & -\frac{1}{m}Q_l(\phi_2) & -\frac{1}{m}Q_d(\phi_3) & +\frac{1}{m}Q_l(\phi_4) \\ \frac{r}{J_z}Q_t(\phi_1) & \frac{r}{J_z}Q_t(\phi_2) & \frac{r}{J_z}Q_t(\phi_3) & \frac{r}{J_z}Q_t(\phi_4) \end{bmatrix} \quad (3.44)$$

The structure of equation 3.42 is a set of three nonlinear double-integrators where the coupling is introduced by the state-dependent input matrix. Matrix  $[\hat{B}(\mathbf{x})]$  determines how the light sources affect the translational and rotational dynamics, the elements of  $[\hat{B}(\mathbf{x})]$  are the force coefficients functions defined above and they all depend on the state  $\phi$  (i.e. the way the inputs affects the states depends on the relative angle of attack  $\phi_i$ ). Considering the relation in equation 3.41 and grouping each contribution, equation 3.44 can be rewritten as:

$$[\hat{B}(\mathbf{x})] = [\hat{B}(\phi)] = \begin{bmatrix} f_{x1}(\phi) & f_{x2}(\phi) & f_{x3}(\phi) & f_{x4}(\phi) \\ f_{y1}(\phi) & f_{y2}(\phi) & f_{y3}(\phi) & f_{y4}(\phi) \\ f_{t1}(\phi) & f_{t2}(\phi) & f_{t3}(\phi) & f_{t4}(\phi) \end{bmatrix} \quad (3.45)$$

## 3.5 Control strategies for the 3DOF model

The aim of this section is to develop a control strategy that is able to bring the state-vector in equation 3.42 from any initial condition to the origin of the state-space. The class of nonlinear models with the structure of equation 3.42 is called

state-dependent models and their structural similarity with linear state-space models suggests a state-dependent Riccati equations (SDRE) control approach. [9, 32].

### 3.5.1 State-dependent Riccati equation approach

A general affine nonlinear system  $\dot{\mathbf{x}} = \mathbf{f}(\mathbf{x}) + \mathbf{g}(\mathbf{x})\mathbf{u}$  can be transformed into a non unique state-dependent coefficient parametrization  $\dot{\mathbf{x}} = [A(\mathbf{x})]\mathbf{x} + [B(\mathbf{x})]\mathbf{u}$  that mimics a linear state-space structure. The system in 3.42 has already a state-dependent coefficient structure therefore all the problems posed by the non uniqueness of the parametrization are not present. For this nonlinear system, a control law is sought that, while driving the system states to the origin from any point in the state-space, minimizes the infinite horizon cost functional:

$$J = \frac{1}{2} \int_0^{\infty} \mathbf{x}^T [Q] \mathbf{x} + \mathbf{u}^T [R] \mathbf{u} dt \quad (3.46)$$

The exact nonlinear infinite-horizon optimal control problem solution can be obtained solving the Hamilton-Jacobi-Bellman partial differential equation that provides a necessary and sufficient condition for optimality. The Hamiltonian for this problem is:

$$H(\mathbf{x}, \mathbf{u}, \frac{\partial V}{\partial \mathbf{x}}) = \frac{1}{2} \mathbf{x}^T [Q] \mathbf{x} + \frac{1}{2} \mathbf{u}^T [R] \mathbf{u} + \frac{\partial V}{\partial \mathbf{x}} ([A]\mathbf{x} + [B(\mathbf{x})]\mathbf{u}) \quad (3.47)$$

Where  $V = V(\mathbf{x})$  is the value function of Dynamic Programming theory. The HJB equation can be derived from the DP principle as:

$$\frac{\partial V}{\partial t} + \inf_{\mathbf{u} \in \mathcal{U}} H(\mathbf{x}, \mathbf{u}, \frac{\partial V}{\partial \mathbf{x}}) = 0 \quad (3.48)$$

The nonlinear system is time invariant, a candidate value function is  $V(\mathbf{x}) = \frac{1}{2} \mathbf{x}^T [P(\mathbf{x})] \mathbf{x}$  that is not explicitly time dependent. The optimal feedback control action that satisfies the HJB condition on the Hamiltonian can be obtained by substituting the candidate value function and then zeroing the first variation of the Hamiltonian with respect to the control input:

$$\frac{\partial H}{\partial \mathbf{u}} = 0 \rightarrow \mathbf{u} = -[R]^{-1} [B(\mathbf{x})]^T [P(\mathbf{x})] \mathbf{x} \quad (3.49)$$

Therefore HJB condition reduces to:

$$\frac{1}{2} \mathbf{x}^T ([P(\mathbf{x})][A] + [A]^T [P(\mathbf{x})] - [P(\mathbf{x})][B(\mathbf{x})][R]^{-1} [B(\mathbf{x})]^T [P(\mathbf{x})] + [Q]) \mathbf{x} = 0 \quad (3.50)$$

Where 3.50 is obtained substituting the optimal feedback control action 3.49 in equation 3.48. In the linear case, the algebraic Riccati equation is obtained directly from 3.50 but since  $[B(\mathbf{x})]$  is a matrix valued function of  $\mathbf{x}$  the quantity inside the parenthesis in 3.50 can not be set to zero. The state-dependent Riccati equation (SDRE) approach provides an approximation to the HJB equation and yields in general a suboptimal feedback control law for the infinite-horizon optimization problem. The SDRE algorithm consists of finding the symmetric positive-definite solution  $[P(\mathbf{x})]$  to the Riccati state-dependent algebraic matrix equation:

$$[P(\mathbf{x})][A] + [A]^T[P(\mathbf{x})] - [P(\mathbf{x})][B(\mathbf{x})][R]^{-1}[B(\mathbf{x})]^T[P(\mathbf{x})] + [Q] = 0 \quad (3.51)$$

At each instant, the method treats the state-dependent coefficients matrices as being constant, and computes a control action by solving an LQ optimal control problem. The resulting controller relies to the existence of a pointwise solution of equation 3.51. In this case the state-dependent input matrix is only a function of the angle of attack therefore the existence of solutions can be checked numerically solving the equation for  $\phi \in [0, 2\pi]$ . For a general input-affine system that has been factorized in state-dependent coefficient form, depending on the choice of  $[A(\mathbf{x})]$  only local asymptotic stability and local optimality can be proven for the closed-loop system. However, it is possible to show [9] that global asymptotic stability is recoverable if the closed-loop coefficient matrix is symmetric and the pair  $\{[A(\mathbf{x})], B(\mathbf{x})\}$  is controllable for every  $\mathbf{x}$  in the state-space. In LQR control theory, the existence of solution to the optimal feedback controller is determined by the controllability of the system, by the positive definiteness of the control weight matrix  $[R]$  and by the semi-positive definiteness of matrix  $[Q]$ . The concept of point-wise controllability [9, 13, 22] extends the linear controllability concept to state-dependent models with the following theorem.

**Theorem 1**  $[A(\mathbf{x})]$  is a controllable parametrization of the nonlinear system if  $\{[A(\mathbf{x})], [B(\mathbf{x})]\}$  is a controllable pair for all  $\mathbf{x} \in \mathbb{R}^n$ .

This condition is easy to verify for the system in 3.42,  $[A]$  is a constant matrix while  $[B(\mathbf{x})] = [B(\phi)]$ .  $\phi$  is an angular quantity, thus it needs only to be evaluated in the range  $[0, 2\pi]$ . The condition expressed in theorem 1 can be reformulated as:

$$\begin{cases} K(\phi) = [B(\phi) AB(\phi) A^2B(\phi) A^3B(\phi) A^4B(\phi) A^5B(\phi)] \\ \text{rank}(K(\phi)) = 6 \quad \forall \quad \phi \in [0, 2\pi] \end{cases} \quad (3.52)$$

The point-wise controllability is evaluated for each angle  $\phi$  with the Kalman rank condition. It turns out that this condition is verified for every angle  $\phi$  for the system in 3.42, thus the system is point-wise fully controllable and a solution to the state-dependent Riccati equation in 3.51 exists anywhere in the state-space. To prove the

global asymptotic stability, the following theorem introduces a symmetry condition on the closed loop matrix.

**Theorem 2** *If the closed-loop coefficient matrix  $[A(\mathbf{x})_d]$  is symmetric for all  $\mathbf{x} \in \mathbb{R}^n$ , then if the pair  $\{[A(\mathbf{x})], [B(\mathbf{x})]\}$  is point-wise controllable, the closed-loop solution is globally asymptotically stable.*

The closed-loop state-dependent matrix is:

$$[A(\phi)_d] = [A] - [R]^{-1}[B(\phi)]^T[P(\phi)] \quad (3.53)$$

Where  $[P(\phi)]$  is the solution of:

$$[P(\phi)][A] + [A]^T[P(\phi)] - [P(\phi)][B(\phi)][R]^{-1}[B(\phi)]^T[P(\phi)] + [Q] = 0 \quad (3.54)$$

Its existence is proven by the previous controllability result. In this case  $[A(\phi)_d]$  is symmetric for every angle  $\phi$  as a consequence the controlled system is globally asymptotically stable and thus it is possible to regulate the states to the origin regardless of the initial conditions.

### SDR simulation

A Python model of the system in 3.42 is implemented together with a SDR controller. The SDR controller solves equation 3.54 at each time step and compute the control inputs using equation 3.49. The control inputs correspond to the intensity of the four laser sources  $a_i$ . The parameters that determine the performance of the controller are the weighting matrices  $Q$  and  $R$ . After normalizing the weights in  $Q$  due to the different units of the state-vector, the weights are tuned with a trial and error procedure.

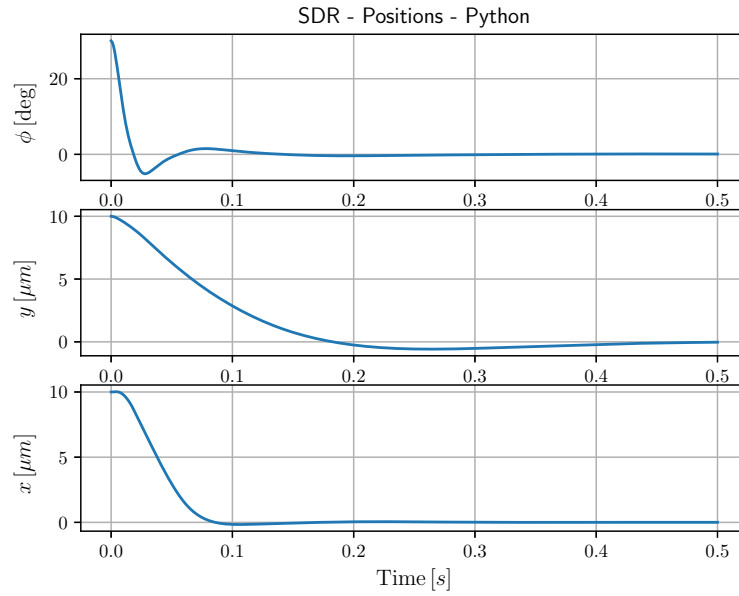


Figure 3.26: Controlled Position and Orientation

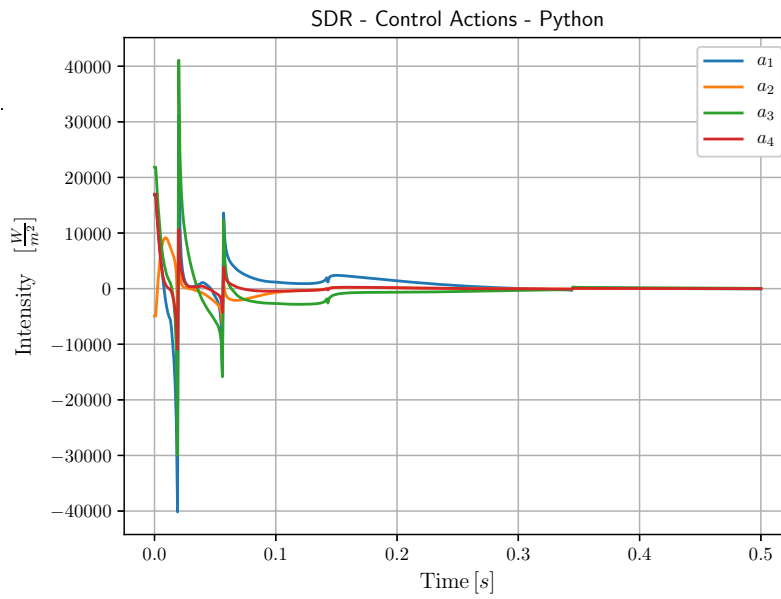


Figure 3.27: Control Actions

In figure 3.26 the convergence to the origin of the state-space is shown for the last three states (i.e.  $x, y$  and  $\phi$ ), obviously their derivatives go to zero as well. The initial

conditions are set at  $10\mu\text{m}$  in each direction and a rotation of  $30[\text{deg}]$ . However, looking at figure 3.27, negative unphysical control actions are theoretically required. The control inputs are constrained to be non negative and if they are saturated and forced to be positive the controller is no more able to drive the system to the origin. A method to take explicitly into account this constraint is the Constrained state-dependent Riccati equation that is implemented in the next section.

### 3.5.2 CD-SDR MPC approach

The CD-SDRE is a way to take into account input constraints directly, in this sense it is similar to an MPC. The aim is to develop a control strategy for the system in 3.42 such that the control inputs (i.e. the light intensities) are nonnegative. This approach uses equations of motion in discrete fashion and the MPC framework to derive an optimization problem that can be solved using quadratic programming. Following the MPC idea the quadratic cost function is of the form:

$$J(\mathbf{x}(0), \mathbf{U}) = \frac{1}{2} \sum_{k=0}^{N_h} \mathbf{x}_k^T [Q] \mathbf{x}_k + \mathbf{u}_k [R] \mathbf{u}_k \quad (3.55)$$

The horizon in 3.55 is finite and consists of  $N_h$  steps thus giving an additional parameter to tune the controller. Vector  $\mathbf{U}$  is obtained appending the control sequence  $\mathbf{u}_k$  in a single vector and constitutes the optimization variable (i.e.  $\mathbf{U} = [\mathbf{u}_0, \mathbf{u}_1, \dots, \mathbf{u}_{N_h-1}]$ ). The dynamic constraint is the discretized version of equation 3.42 that is propagated at each step. The discrete matrices are obtained with the zero-order hold technique from their continuous counterpart. Mimicking the zero order hold method for linear systems, the linear state-matrix and the non-linear input matrix in equation 3.42 can be discretized [19]. Considering a small enough time step  $\Delta t$ :

$$[A_d] = e^{[A]\Delta t} = \sum_{k=0}^{\infty} \frac{[A]^k \Delta t^k}{k!} \approx I + [A]\Delta t = \begin{bmatrix} 1 & 0 & 0 & 0 & 0 & 0 \\ 0 & 1 & 0 & 0 & 0 & 0 \\ 0 & 0 & 1 & 0 & 0 & 0 \\ \Delta t & 0 & 0 & 1 & 0 & 0 \\ 0 & \Delta t & 0 & 0 & 1 & 0 \\ 0 & 0 & \Delta t & 0 & 0 & 1 \end{bmatrix} \quad (3.56)$$

$$[B_d] = \int_{t_0}^{t_0+\Delta t} e^{[A]\tau} [B(\mathbf{x}(\tau))] d\tau \approx [B(\mathbf{x}(t_0))]\Delta t + \frac{1}{2}[A][B(\mathbf{x}(t_0))]\Delta t^2 \quad (3.57)$$

Equation 3.56 is approximated with a Taylor series up to first order. In 3.57 the matrix valued function  $[B]$  is supposed to be approximately constant in the time

interval  $\Delta t$ . Equation 3.42 can be approximately transformed into the difference equation:

$$\mathbf{x}_{k+1} = [A_d]\mathbf{x}_k + [B_d(\mathbf{x}_k)]\mathbf{u}_k \quad (3.58)$$

The finite horizon discrete optimal control problem is thus:

$$\min_{\mathbf{U}} \quad J(\mathbf{x}(0), \mathbf{U}) \quad (3.59)$$

$$\text{subject to} \quad \mathbf{x}_{k+1} = [A_d]\mathbf{x}_k + [B_d(\mathbf{x}_k)]\mathbf{u}_k \quad (3.60)$$

$$u_{k,i} \geq 0 \quad (3.61)$$

The constraint 3.61 specifies that each laser source intensity  $i$  must be nonnegative at each time instant  $k$ . It is not trivial to solve the problem above in the current form, due to the nonlinear state propagation, numerical methods from techniques such as nonlinear programming should be invoked. A viable approximation is to use the SDR approach (i.e. the similarities with a linear system) and recast the optimization problem as a standard linear MPC. In the standard MPC framework, the optimization is performed at each step and then, after that the first control action of the sequence is applied (i.e.  $\mathbf{U}(0)$ ), the horizon window is shifted and the control recomputed. If the time window is reasonably tuned not to be too wide, the state dynamics can be computed approximating it to a linear one. The resulting linearized equation is:

$$\mathbf{x}_{k+1} = [A_d]\mathbf{x}_k + [B_d(\mathbf{x}_0)]\mathbf{u}_k \quad (3.62)$$

Equation 3.62 is used instead of 3.60 so that the dynamic constraint becomes linear and the optimization problem is a quadratic problem with linear constraints. The discrete control input matrix is evaluated at the beginning of each step.

Numerically efficient techniques exist to solve such problems in Python environment such as CVXOPT or CVXPY. The lower level solver CVXOPT is preferred due to ease of implementation in the DSENDSEdu simulator. As done for the SDR case, a Python simulation is performed to test that the hypothesis previously made in the linearization hold. The main limitation of this approach is indeed that the propagation of the state seen by the controller is linear and depends on the state at the beginning of the optimization horizon (i.e.  $\mathbf{x}_0$ ). This problem influences the choice of the optimal horizon. An horizon too wide will decrease performance due to its incorrect propagation of the dynamics while an horizon too short will not have the capacity to predict the response of the system and consequently optimize the control actions. Two time steps are considered in the integration of the system. A smaller time steps  $dt = 10^{-5} [s]$  is used for the integration of the dynamics while

$dt_c = 10^{-2}$  [s] is used inside the controller to discretize the dynamic equations and propagate them using the MPC logic. The number of time steps that the controller propagates is set to  $N = 10$ .

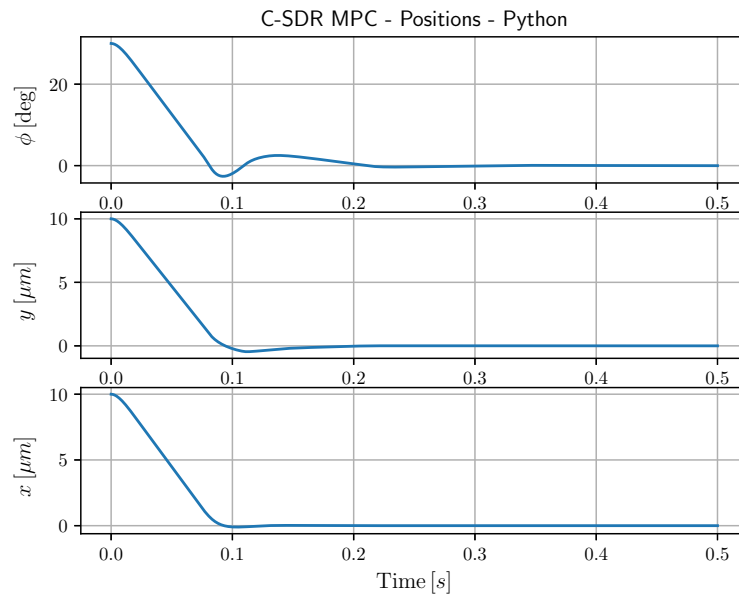


Figure 3.28: Controlled Position and Orientation

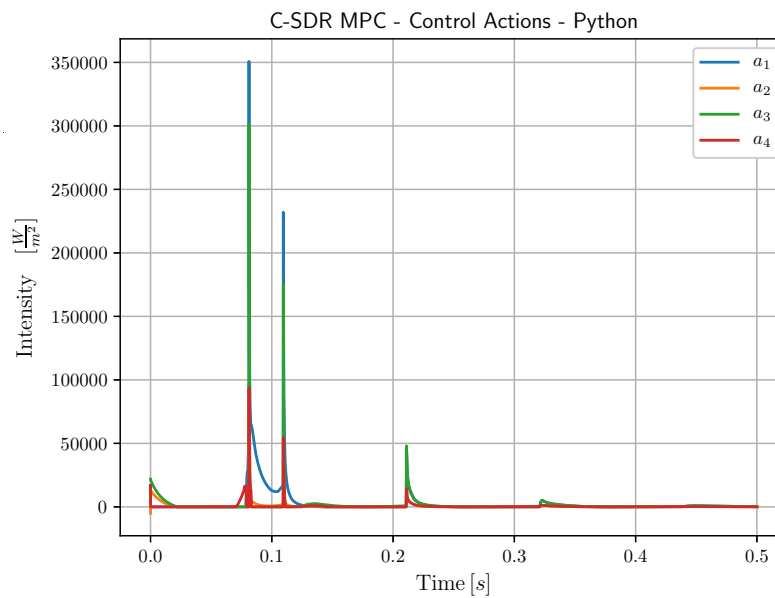


Figure 3.29: Control Actions

The figures above show that with the CD-SDR approach is possible to realign and reposition the system around the origin of the state space. The theoretical controllability result for the SDR does not hold if the control inputs are constrained to be nonnegative. However, as it is evident from the plots, the system is controllable. The control actions needed are indeed higher with respect to the unconstrained problem but still a fraction of the intensity used for the orientation controller alone (i.e.  $I_{ref} = 10^6 \frac{W}{m^2}$ ). The time of convergence to the origin is still in the same order of magnitude.

The effect of changing the control horizon is analysed in the figures below. It is evident that the optimal selection must be a trade off between a sufficient horizon of propagation and an accurate description of the dynamics.

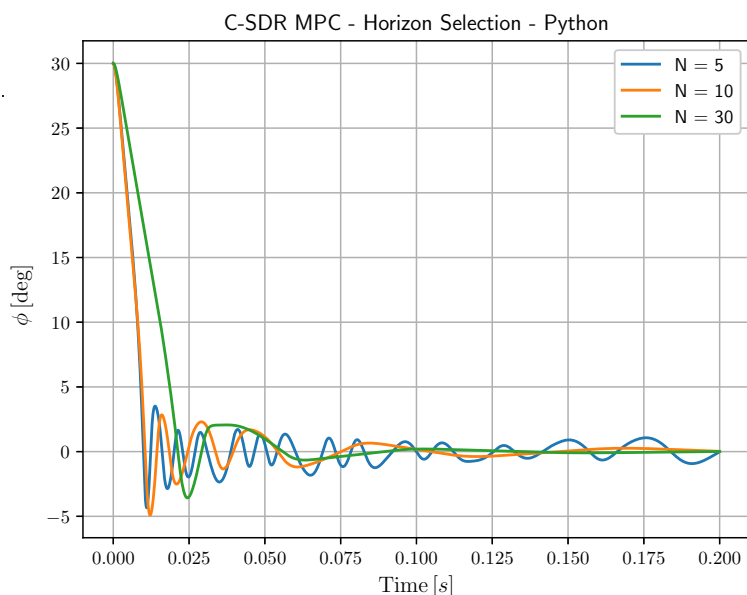


Figure 3.30: Horizon Selection

The time history of the angle of attack is simulated for three different horizons. For  $N = 5$  the horizon is too short and the system starts oscillating at a relatively high frequency. The controller is not able to stably drive the angle to the zero value. For  $N = 30$  the horizon is too long and the propagated dynamics is not accurate as a consequence the controller is slower in reaching the target. A trade-off between these two is the  $N = 10$  steps horizon where the controller achieves good performance.

### 3.6 Controllability for multiple hemispheres

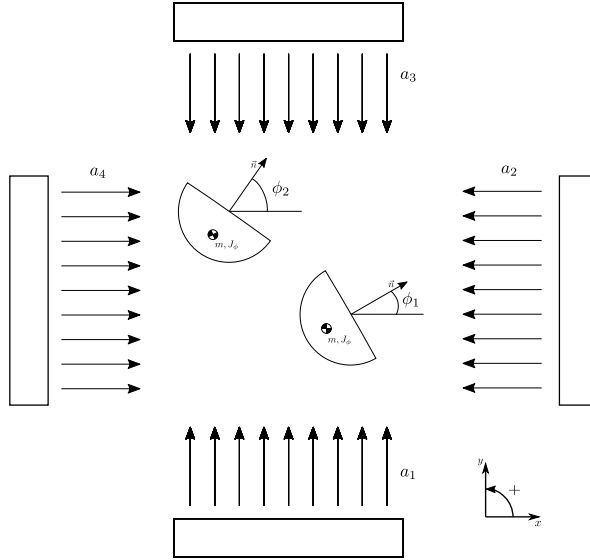


Figure 3.31: System schematics with two hemispheres

In this section, the controllability of a new system composed by multiple identical hemispheres is studied. This is motivated by the fact that in the GI arrangement the laser sources will act as global control actions with the aim of confining and controlling multiple subsystems at the same time. This objective is challenging and it is not trivial to understand if it is achievable even in theory. The point-wise controllability tool can be used to assess the controllability of the system. The same arrangement with four sources is considered. The overall system state space model is obtained stacking the states of the subsystems. The laser sources on the four sides are the global inputs. The state and its derivative for each element are expressed as:

$$\mathbf{x}_i = \begin{bmatrix} \dot{x}_i \\ \dot{y}_i \\ \dot{\phi} \\ x_i \\ y_i \\ \phi_i \end{bmatrix} \quad \mathbf{u} = \begin{bmatrix} a_1 \\ a_2 \\ a_3 \\ a_4 \end{bmatrix} \quad \dot{\mathbf{x}}_i = [A]_i \mathbf{x}_i + [B(\mathbf{x}_i)]_i \mathbf{u} \quad (3.63)$$

The overall state and its time evolution is obtained stacking together the states of

the elemental systems.

$$\mathbf{z} = \begin{bmatrix} \mathbf{x}_0 \\ \mathbf{x}_1 \\ \dots \\ \mathbf{x}_n \end{bmatrix} \quad \dot{\mathbf{z}} = [A]_z \mathbf{z} + [B]_z(\mathbf{z}) \mathbf{u} \quad (3.64)$$

Where the state and input matrices are:

$$[A]_z = \begin{bmatrix} [A]_1 & 0 & \dots & 0 \\ 0 & [A]_2 & \dots & 0 \\ \dots & \dots & \dots & \dots \\ 0 & 0 & \dots & [A]_n \end{bmatrix} \quad [B(\mathbf{z})]_z = \begin{bmatrix} [B(\mathbf{x}_1)]_1 \\ [B(\mathbf{x}_2)]_2 \\ \dots \\ [B(\mathbf{x}_n)]_n \end{bmatrix} \quad (3.65)$$

Mutual interactions between the subelements are not considered as a consequence the state matrix is block diagonal. The coupling originates from the global control actions but each subsystem is affected differently due to the state dependency of the input matrix. The theorem on point-wise controllability can be used to study the controllability of the overall system. The input matrix dependency on the state can be reduced as:

$$[B(\mathbf{z})]_z = \begin{bmatrix} [B(\phi_1)]_1 \\ [B(\phi_2)]_2 \\ \dots \\ [B(\phi_n)]_n \end{bmatrix} \quad (3.66)$$

For the sake of simplicity, considering only two subsystems the controllability matrix must be evaluated for all the possible values of  $\phi_1$  and  $\phi_2$ , as a consequence, the grid  $[0, 2\pi] \times [0, 2\pi]$  must be spanned. In this case the state and input matrices are:

$$[A]_z = \begin{bmatrix} [A]_1 & 0 \\ 0 & [A]_2 \end{bmatrix} \quad [B(\mathbf{z})]_z = \begin{bmatrix} [B(\phi_1)]_1 \\ [B(\phi_2)]_2 \end{bmatrix} \quad (3.67)$$

Thus the controllability matrix is:

$$\begin{cases} [K(\phi_1, \phi_2)] = [[B(\phi_1, \phi_2)] A [B(\phi_1, \phi_2)] A^2 [B(\phi_1, \phi_2)] \dots A^{11} [B(\phi_1, \phi_2)]] \\ \text{rank}([K(\phi_1, \phi_2)]) = 6 \quad \forall \quad \phi_1, \phi_2 \in [0, 2\pi] \end{cases} \quad (3.68)$$

Equation 3.68 shows that the number of controllable states of the system is 6. This means that only a hemisphere is controllable or a six dimensional combination of the states of the two as for example the mean state. In the next chapter, the loss of controllability of a system of multiple particles will be analyzed and it will be proved that it does not depend on the nonlinearities but on the global nature of the control actions.

# Chapter 4

## Particle density control

The control of a granular medium presents complex challenges. In the previous chapter, non linear control strategies have been successfully applied to a single grain achieving control and realignment. Furthermore, a novel approach to tackle multiple grains realignment has been proposed. However, this strategy works in very specific conditions and position control is not present. It has also been shown that with the layout used for position control of one particle, multiple particles are not controllable in the deterministic sense. A realistic granular medium model should take into account the different dynamics occurring simultaneously. At the micro-scale the single grain dynamics is predominant while at the meso-scale a collective behaviour necessarily emerge. In this dissertation the granular medium is modeled as a large ensemble of identical rigid bodies with a 'preferred' direction. In recent years, many approaches have been developed for controlling swarm of active elements. Most of the strategies aim at defining the control law for each agent based on the density (i.e. the spatial distribution) either in a centralized or decentralized way [17]. The control actions are then applied to each element of the swarm with an independent actuator, the control laws are Markov feedback laws with global gains but dependent on the specific state of each agent, that's why an independent actuation is needed. The striking difference in this case is that the cloud of refractive grains is not only actuated at-a-distance but the control actions are of global nature, in the sense that the number of inputs is orders of magnitude less than the degree of freedoms of the system. The cloud is therefore largely underactuated. A possible solution to this problem could be to make use of results from ensemble control theory [7, 33]. This approach aims at controlling simultaneously ensembles of almost identical systems with a global control action. However, this ends up in an open-loop control strategy and it relies on the strong assumption that all the elemental (i.e. subsystems) are in the same initial state. Although being a powerful approach to control parametric

ensembles, it is a tool that can not be used in this case. The control of collective behaviour of identical elements has been addressed in [8] but also in this case the nature of the actuation is local. However, the idea of transporting the physical positions of the elements into a density of mass then normalized to be a probability distribution can be exploited. The idea is to design a control law that depends on the density of all the particles as a whole. The equations of motion are then recast as a density time evolution [26]. The equations of motion of the single particles turn into a density dynamic evolution that in deterministic continuous time is described by the Liouville equation while if stochastic effects are considered by the Fokker–Planck equation [6]. In discrete time, the density evolution can be controlled reformulating Optimal Transport based techniques [30]. The next section will prove that a deterministic classical control approach is not applicable for transporting multiple particles simultaneously even in simpler systems thus setting the path to a global average stochastic control strategy. A simplification of the system considered in the previous chapter is adopted and a more theoretical approach is used to study the feasibility of this control strategy. Describing the control problem in terms of density evolution instead of tracking the states of every single particle allows to reduce the dimensionality of the problem. Furthermore, even if the single particles are not controllable their collective behaviour can be to some extent controlled and guided to a certain set of distributions.

## 4.1 Considerations on controllability

The final part of the previous chapter has shown that a complex system made of several copies of the nonlinear system of hemispheres is not controllable in the classical sense with the actual schematic with four inputs. Even when the particles to be controlled are two the system is not controllable. It is useful to consider a simplified model for the particles that neglects the nonlinearity introduced by the angle of attack to gain further insight on the controllability of such systems.

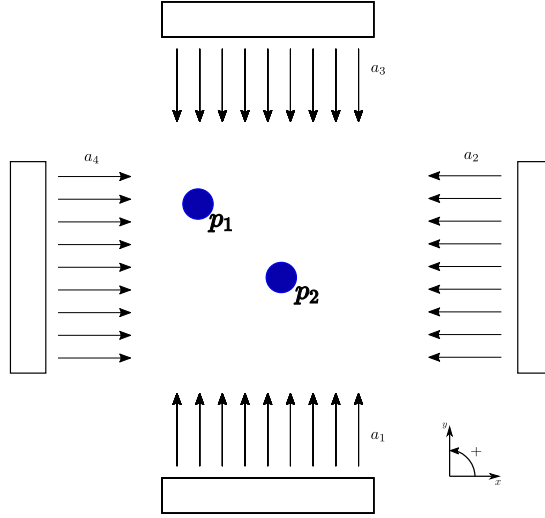


Figure 4.1: Simplified model schematics

The simplified model is a system of two particles that behave as simple double integrators with unit mass. Each of the four inputs affect directly the acceleration in the respective direction. The subsystems states are the position and velocity in the two directions. The overall state of the system is obtained by stacking the states of the subsystems together. The overall system is still subjected to the same number of control inputs. For the moment being, the constraint on the nonnegative nature of the control input is also neglected, this would indeed reduce the degree of controllability of the system. The states and inputs of the system are:

$$\mathbf{x}_i = \begin{bmatrix} \dot{x}_i \\ \dot{y}_i \\ x_i \\ y_i \end{bmatrix} \quad \mathbf{x} = \begin{bmatrix} \mathbf{x}_1 \\ \mathbf{x}_2 \\ \dots \\ \mathbf{x}_n \end{bmatrix} \quad \mathbf{u} = \begin{bmatrix} a_1 \\ a_2 \\ a_3 \\ a_4 \end{bmatrix} \quad (4.1)$$

The equation of motion of the subsystem is:

$$\dot{\mathbf{x}}_i = [A]_i \mathbf{x}_i + [B]_i \mathbf{u} = \begin{bmatrix} 0 & 0 & 0 & 0 \\ 0 & 0 & 0 & 0 \\ 1 & 0 & 0 & 0 \\ 0 & 1 & 0 & 0 \end{bmatrix} \mathbf{x}_i + \begin{bmatrix} 0 & -1 & 0 & 1 \\ 1 & 0 & -1 & 0 \\ 0 & 0 & 0 & 0 \\ 0 & 0 & 0 & 0 \end{bmatrix} \mathbf{u} \quad (4.2)$$

While the overall equation of motion is:

$$\dot{\mathbf{x}} = [A]\mathbf{x} + [B]\mathbf{u} = \begin{bmatrix} [A]_1 & 0 & \dots & 0 \\ 0 & [A]_2 & \dots & 0 \\ \dots & \dots & \dots & \dots \\ 0 & 0 & \dots & [A]_n \end{bmatrix} \begin{bmatrix} \mathbf{x}_1 \\ \mathbf{x}_2 \\ \dots \\ \mathbf{x}_n \end{bmatrix} + \begin{bmatrix} [B]_1 \\ [B]_2 \\ \dots \\ [B]_n \end{bmatrix} \mathbf{u} \quad (4.3)$$

For the sake of simplicity let's consider a system of two particles. In this case the state and input matrices are:

$$[A] = \begin{bmatrix} [A]_1 & 0 \\ 0 & [A]_2 \end{bmatrix} \quad [B] = \begin{bmatrix} [B]_1 \\ [B]_2 \end{bmatrix} \quad (4.4)$$

The overall system is indeed linear and the controllability of the pair  $\{[A], [B]\}$  can be checked using Kalman rank condition. In this case the state space is 8-dimensional so the controllability matrix is:

$$[K] = [[B] \quad [A][B] \quad \dots \quad [A]^7[B]] \quad (4.5)$$

The number of controllable is given by the rank of matrix  $[K]$ :

$$\text{rank}([K]) = 4 \quad (4.6)$$

The number of controllable states is 4 that means that only one particle is fully controllable. The problem is in the global nature of the input effects that does not allow a decoupling in the way it affects the dynamics of the particles. This section has then shown that the lack of controllability for the nonlinear system studied in detail in the previous chapter does not come from the nonlinear effects but simply on the global nature of the control actions that affect each sub-element simultaneously. The controllability problem does not even depend on the double integrator structure of the system. If the model is further reduced to a system of particles that behave as single integrators (i.e. there is no velocity and the control action acts directly on position). In this way, the system states are halved and the subsystem is:

$$\mathbf{x}_i = \begin{bmatrix} x_i \\ y_i \end{bmatrix} \quad \dot{\mathbf{x}}_i = [A]_i \mathbf{x}_i + [B]_i \mathbf{u} = \begin{bmatrix} 1 & 0 \\ 0 & 1 \end{bmatrix} \mathbf{x}_i + \begin{bmatrix} 0 & -1 & 0 & 1 \\ 1 & 0 & -1 & 0 \end{bmatrix} \mathbf{u} \quad (4.7)$$

The controllability matrix is:

$$[K] = [[B] \quad [A][B] \quad [A]^2[B] \quad [A]^3[B]] \quad (4.8)$$

The number of controllable states is again given by the rank of matrix  $[K]$ :

$$\text{rank}([K]) = 2 \tag{4.9}$$

This demonstrates that even a system composed of single integrator elements is not controllable with the actual layout when the number of particles is two or higher. However, the classical concept of controllability is probably not the right tool to assess the capacity of a set of actuators to steer a system of particles. What the failure of controllability test does tell is that the states of the particles are not controllable in the deterministic sense.

## 4.2 Collective control

The previous section studied the controllability of the states of every single particle, a change of the viewpoint of this problem is necessary to address the challenge of controlling an uncountable number of particles simultaneously. A system of many particles in the Euclidian space can be studied in terms of the "density" of the particles in a specified control volume. This approach tackles the problem considering that the number of particles is high enough with respect to the dimension of the control volume that is possible to define a local density function. The problem is thus reduced to control the density function over the workspace. Then the control system should be designed to steer the density towards a desired target distribution. This approach in continuous time can be modeled with partial differential equations of the reaction-advection-diffusion type where the desired coverage profiles are obtained by tuning the parameters in the model or by boundary control [17, 10]. The problem of controlling the particles turn into the problem of controlling the density function. The density function is tuned to obtain an average collective behaviour. In this dissertation, the density control will be addressed reformulating the problem as a discrete Optimal Mass Transportation problem.

### 4.2.1 Optimal Transport based control

The Optimal Mass Transport theory is concerned with moving mass from an initial distribution to a final one with the least amount of cost. It was originally formulated to move amount of 'mass' from a certain distribution (position) to another in an optimal sense. This optimal 'mass' transportation problem can be reformulated in terms of probability distributions after a unitary rescaling [30]. A probability mass function describes the probability of finding a certain amount of mass in a specific location. Originally, the OT problem has been formulated in a static fashion [8], thus concerned in finding an optimal map between an initial and a final distribution (i.e. 'what' goes 'where'). If a dynamic extension is considered, the controlled evolution

of the density function towards a desired distribution is analogous to a stochastic optimal control problem. This stochastic viewpoint can be used to describe the system of particles (grains) focusing on their collective behaviour. The optimization objective is to find a transport map that given a certain distribution is able to steer it towards the desired one. The optimal transport map is the one that, among all the possible maps between the two desired distributions, is able to minimize a certain cost functional [26, 17, 8]. In the following section, this approach is used to steer the density of particles towards a desired distribution.

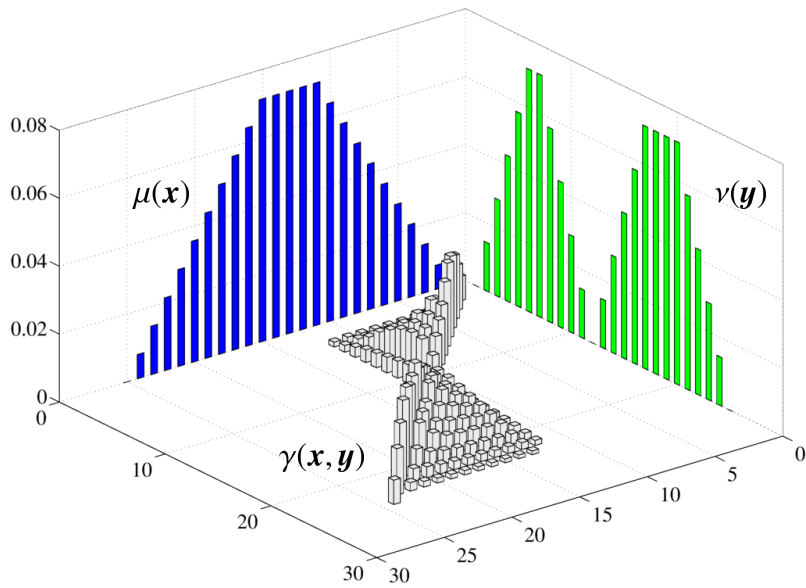


Figure 4.2: The initial probability mass function (pmf)  $\mu(x)$  (in blue) is transported to the desired pmf  $\nu(y)$  (in green) while minimizing the cost function  $c(x, y) = \|x - y\|_2$ . The optimum transference plan  $\gamma(x, y)$  is shown in gray. (Reproduced with permission from [26]).

### 4.3 OT with Euler step dynamics

The formulation of the problem and its modeling are taken from [26]. Consider a 2D workspace that is delimited by actuators on four side. This is basically a multi-grid generalization of the system schematics adopted in the previous chapters. The workspace is discretized according to the number of actuators. Each element of the grid is called a bin. The considerations on controllability of the previous section have shown that a classical control approach for multiple particles in the same bin is not possible. The problem is in the global nature of the actions that affects each particle in the same way. A possible solution is to introduce a decoupling due to the

distance from the specific actuator. This is justified by the fact that, for example, the force introduced by electrodynamic actuators will depend on the inverse of the distance from the source. Furthermore, it is assumed that the discretized dynamics in time behaves as a set of single integrators (i.e. the inertial forces are neglected).

### 4.3.1 Derivation of the stochastic density evolution

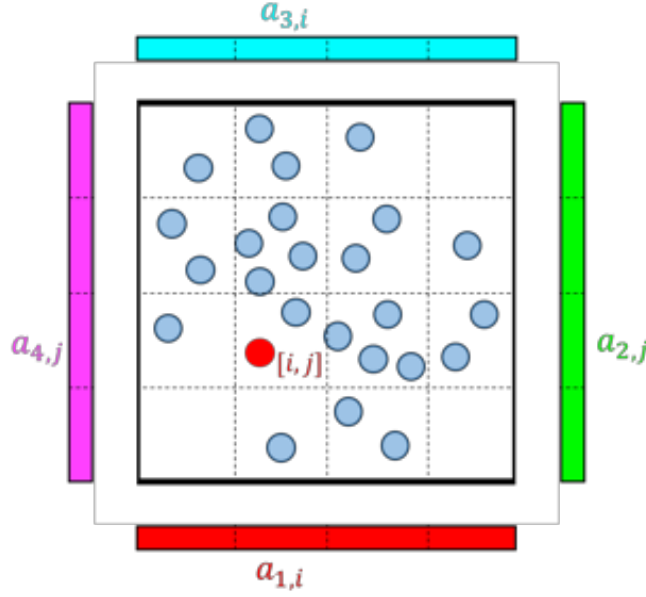


Figure 4.3: The red particle in the bin  $[i, j]$  experiences the forces from the actuators  $a_{1,i}, a_{2,j}, a_{3,i}, a_{4,i}$  (Reproduced with permission from [26])

The equation of motion for a particle  $p$  located in bin  $[i, j]$  at time instant  $k$  is:

$$\mathbf{x}_{k+1}^p = \mathbf{x}_k^p + \Delta \mathbf{f} \quad \mathbf{x}_k^p = \begin{bmatrix} x_k^p \\ y_k^p \end{bmatrix} \quad (4.10)$$

Where  $\Delta$  is the time step and  $\mathbf{f}$  is the force that depends on the position of the particle at time instant  $k$ , specifically on the distance from the four actuators that are active on the bin where the particle is located.

$$f_x = \frac{a_{4,j}}{dis(a_{4,j}, p)} - \frac{a_{2,j}}{dis(a_{2,j}, p)} \quad f_y = \frac{a_{1,i}}{dis(a_{1,i}, p)} - \frac{a_{3,i}}{dis(a_{3,i}, p)} \quad (4.11)$$

$dis(a_{n,i}, p)$  is the distance between particle  $p$  and the actuator  $a_{n,i}$ .

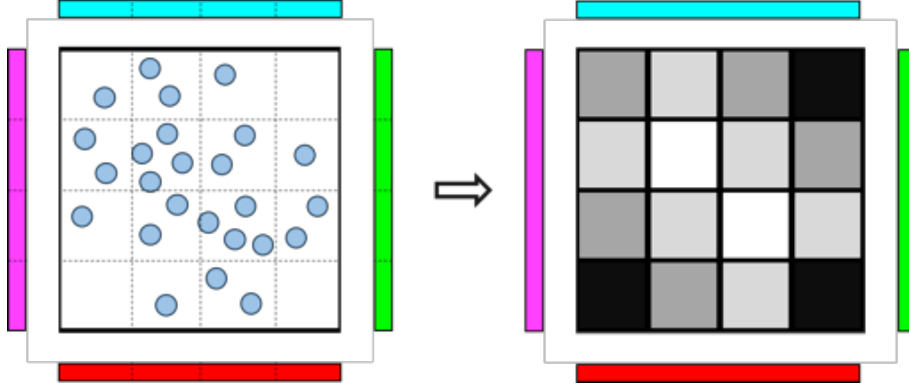


Figure 4.4: The cloud of particles is transformed into a probability distribution, the lighter bins contain more probability mass (Reproduced with permission from [26]).

The deterministic layout in figure 4.3.1 can be transformed in a stochastic one defining the discrete probability density matrix  $\mu \in \mathbb{R}^{n_{bins} \times n_{bins}}$  where  $\mu[i, j]$  represents the probability mass present in the bin  $[i, j]$ . For  $\mu$  to be a probability density function the conservation property  $\sum_{i=1}^{n_{bins}} \sum_{j=1}^{n_{bins}} \mu[i, j] = 1$  must hold, this problem must be automatically taken into account in the density evolution. The information about the specific position of the particles inside each bin is lost while the average discrete spatial distribution over the workspace is considered. The discrete time evolution of the density function  $\mu$  is derived from the particle dynamics model in 4.10. If  $l_{bin}$  represents the length and wide of each bin, it follows from 4.10 that the force from actuator  $a_{1,i}$  that would move all the particles in bin  $[i, j]$  to the bin  $[i, j + 1]$ , thus pushing them horizontally is given by:

$$a_{1,i,j,max} = \frac{1}{\Delta} l_{bin} dis(a_{1,i}, [i, j]) \quad (4.12)$$

Where  $dis(a_{1,i}, [i, j])$  represents the minimum distance from actuator  $a_{1,i}$  to the bin  $[i, j]$ . The stochastic probabilistic behaviour of the density evolution emerges from the assumption that if  $a_{1,i} \leq a_{1,i,max}$  the fraction of density that will be transported from bin  $[i, j]$  to the bin  $[i, j + 1]$  due to actuator  $a_{1,i}$  is  $\frac{a_{1,i}}{a_{1,i,j,max}}$ . Thus considering the density function at time step  $k$  evaluated at the bin  $[i, j]$ , its evolution at the successive time step is given by:

$$\begin{aligned}
\mu_{k+1}[i, j] = & \mu_k[i, j] \left( 1 - \frac{a_{1,i}}{a_{1,i,j,max}} - \frac{a_{2,j}}{a_{2,i,j,max}} - \frac{a_{3,i}}{a_{3,i,j,max}} - \frac{a_{4,j}}{a_{4,i,j,max}} \right) + \\
& + \frac{\mu_k[i, j-1]a_{1,i}}{a_{1,i,j-1,max}} + \frac{\mu_k[i+1, j]a_{2,j}}{a_{2,i+1,j,max}} + \\
& + \frac{\mu_k[i, j+1]a_{3,i}}{a_{3,i,j+1,max}} + \frac{\mu_k[i-1, j]a_{4,j}}{a_{4,i-1,j,max}}
\end{aligned} \tag{4.13}$$

The constraint on the maximum amount of actuation is needed for the conservation property to hold between successive time step. It is easy to see from equation 4.13 that if the actuation is beyond that limit the probability mass function at step  $k+1$  would go negative. Furthermore, it also limits the propagation of the distribution to flow only towards adjacent bins. The maximum intensity of actuation is limited by the maximum flow allowed for the bins located at the border. It is also assumed that the actuators are located at a certain distance  $d_{act}$  so that the global maximum actuation for each actuator is limited to:

$$a_{max} = \frac{1}{\Delta} l_{bin} d_{act} \tag{4.14}$$

$a_{max}$  is the actuator intensity that moves all the probability mass located on a border bin towards its 'internal' neighbour.

### 4.3.2 Optimal Transport based control problem

The objective of the control strategy is to steer the density distribution of the particles  $\mu \in \mathbb{R}^{n_{bins} \times n_{bins}}$  towards a desired target distribution  $\nu \in \mathbb{R}^{n_{bins} \times n_{bins}}$ , the problem can be formulated as a convex optimization problem whose objective is to find the actuator intensities that minimize a certain distance between the actual and desired distribution at each step [26].

$$\begin{aligned}
& \min_{a_{1,i}, a_{2,j}, a_{3,i}, a_{4,j}} && D_{L_1}(\mu_{k+1}, \nu) \\
& \text{subject to} && \mu_{k+1}[i, j] = f(\mu_k, a_{1,i}, a_{2,j}, a_{3,i}, a_{4,j}) \quad \forall i, j \in \{1, \dots, n_{bins}\} \\
& && a_{1,i} \leq a_{max} \quad \forall i \in \{1, \dots, n_{bins}\} \\
& && a_{2,j} \leq a_{max} \quad \forall j \in \{1, \dots, n_{bins}\} \\
& && a_{3,i} \leq a_{max} \quad \forall i \in \{1, \dots, n_{bins}\} \\
& && a_{4,j} \leq a_{max} \quad \forall j \in \{1, \dots, n_{bins}\}
\end{aligned} \tag{4.15}$$

Where the explicit form of the propagation constraint is expressed by 4.13. The optimization problem formulated in [26] is convex due to the convexity of the constraints and of the cost function. The dynamic constraint between two successive steps is convex because  $\mu_k$  is considered a constant and the optimization seeks for the best possible action to minimize the cost function at step  $k + 1$  modifying the bounded intensities of the actuators. It is easy to notice that with this single-step layout the density  $\mu_{k+1}$  on a certain bin is a linear combination of the four actuators that are effecting that bin. The constraint on the actuators is indeed convex. The distance used is the  $L_1$  matrix norm defined as:

$$D_{L_1}(\mu, \nu) = \sum_i^{n_{bins}} \sum_j^{n_{bins}} | \mu[i, j] - \nu[i, j] | \quad (4.16)$$

Equation 4.16 defines a convex norm therefore convex optimization techniques can be used to solve this problem.

### 4.3.3 Limitation of the current implementation

Although the optimization problem formulated in 4.15 can be solved with efficient numerical algorithms from convex optimization theory, the structure of the metric used (i.e. the cost function), and the horizon considered present some limitations. The optimization problem is solved considering only a single step. The density can only flow between adjacent bins in one time step due to the dynamic constraint 4.13. Furthermore, it can be seen from 4.16 that the maximum distance is bounded. If the two distributions are disjointed (i.e. there is no overlap between them in the square grid) the  $D_{L_1, max}(\mu, \nu) = 2$ . This poses a theoretical problem in the optimization algorithm. If the actual and desired distributions are sufficiently 'distant' the cost function will not be affected by the flow of the distribution at the next step because both  $D_{L_1, max}(\mu_k, \nu) = D_{L_1, max}(\mu_{k+1}, \nu) = 2$  for every combination of the actuator intensities. Furthermore, being  $D_{L_1}$  an element-wise distance it is a limited indicator of the spatial distance between the distributions on the two dimensional grid.

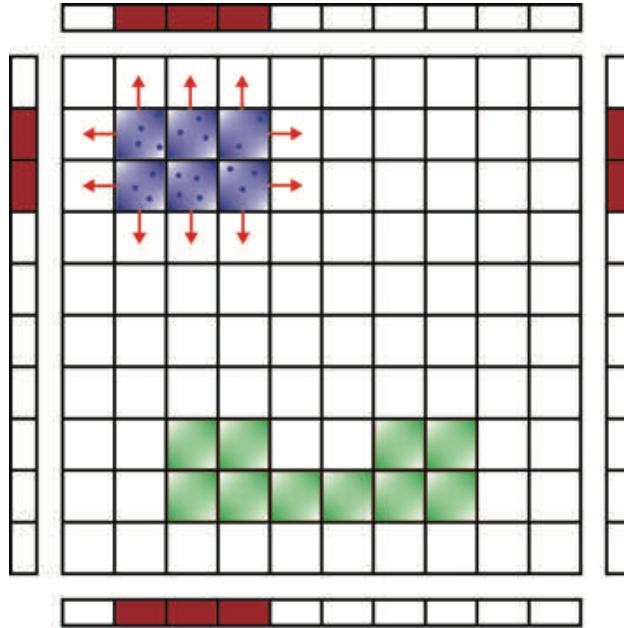


Figure 4.5: The actual probability mass function  $\mu_k$  (in blue) can only be transported between adjacent bins (red arrows), the  $L_1$  distance with the desired distribution  $\nu$  (in green) is unchanged for every combination of the active actuators (in red).

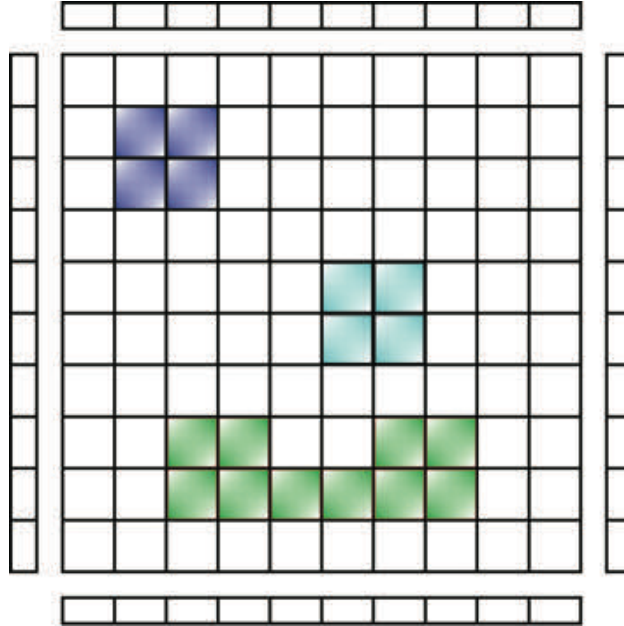


Figure 4.6: the  $L_1$  distance between the density function in blue and in light-blue with respect to the desired distribution  $\nu$  (in green) is the same while it is clear that the light-blue density is in some sense 'closer'.

## 4.4 Reformulation of the OT problem

Optimal Transport Theory provides a way to define a metric that takes simultaneously into account the distance over the grid and the 'amount' of mass to move. This metric is the Wasserstein distance [30] that represents the optimal, minimum cost solution of Monge's Optimal Transport classical problem [29]. It can be seen as the geodesic between the two distributions and thus the ideal objective that the optimization problem must minimize to make the distribution at a certain time step as close as possible to the desired one. The Wasserstein distance in discrete fashion is called the Earth's mover distance (EMD) and in this form is used as a measure of similarity between images [29]. The analogy between a two dimensional distribution of intensity of pixels over an image and the probability distribution of this problem is apparent. Therefore the useful properties of this metric will be exploited to reformulate the previous Optimal Transport problem.

### 4.4.1 Earth's mover distance

In this discrete two dimensional case the probability distributions are matrix valued functions, each element of the matrix is associated to a bin and its value repre-

sents the probability mass in that bin. The discrete Monge’s OT problem seeks for a transport plan that determines how much and where the ‘mass’ in each bin should be moved from the initial distribution to match the desired one minimizing an underlying ground metric. It makes sense to define the ground metric in analogy with the Euclidian distance, assuming unitary distance between the bins. Then the cost of transporting a certain amount of distribution from one bin to another is the distance to be covered times the amount of mass to be transported. The Optimal Transport plan in this case can be recast as a linear problem. The solution to this problem gives the optimal map (i.e. what goes where) and the optimal cost of this transportation. The optimal cost normalized by the total flow is the Earth’s mover distance. However, the classical problem formulation is unconstrained and the mass is free to be moved to every bin directly.

#### 4.4.2 Density control using the earth’s mover distance

In the density control problem, the dynamic constraint limits the flow of the density to neighbouring bins, as a consequence, the optimal transport plan represented by the Earth’s mover distance can not be achieved in one step. However, the control problem can be recast as finding the best possible actuation intensities that minimize the earth’s mover distance at the successive step. In this way, the algorithm searches for the direction of propagation that will have minimum distance from the desired distribution. There is a fundamental difference with the previous metric used. Even if the propagation is limited, the global nature of this new metric is able to ‘see’ the objective in every feasible configuration over the probability space. Hence, there will always be a feasible direction that minimizes the cost until a steady-state distribution is reached (i.e. condition of minimum cost). The drawback of this implementation is the non convexity and the computational cost.

#### 4.4.3 Nonlinear optimization problem

$$\min_{a_{1,i}, a_{2,j}, a_{3,i}, a_{4,j}} D_{EMD}(\mu_{k+1}, \nu) \quad (4.17)$$

The nonlinear optimization problem expressed by equation 4.17 has the same constraints as the convex one but the cost function is now the EMD distance. A routine in Python is used to solve the nonlinear optimization problem. At each step, the algorithm seeks for the actuator intensities that minimize the EMD distance. For each guessed solution the cost is calculated as a solution of a nested linear optimization program. A discrete OT problem is solved to calculate the minimum distance between the propagated distribution  $\mu_{k+1}$  generated by the trial solution and the

desired distribution  $\nu$ . The outer nonlinear optimization algorithm should then converge to the solution that minimizes this distance thus moving the distribution the closest as possible to the desired one. This is still a single step algorithm, in the sense that after the approximate optimal solution is obtained the particle dynamics is propagated and the cycle is repeated. The system is simulated in the figures below.

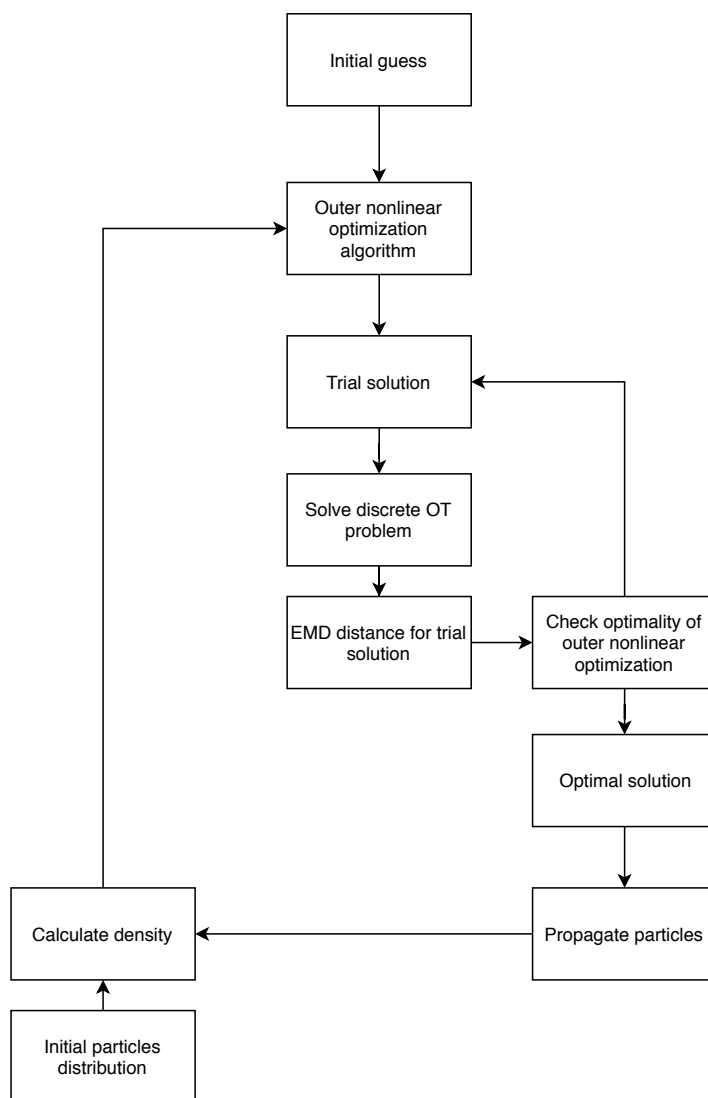


Figure 4.7: Algorithm schematic

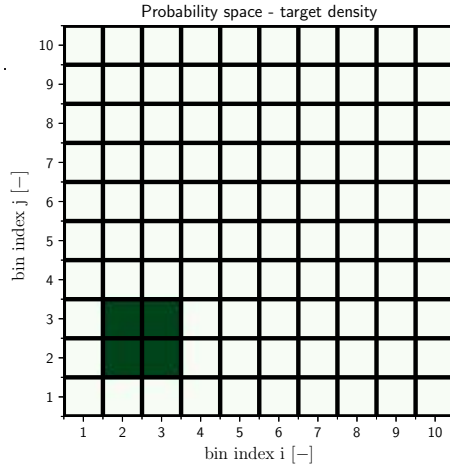


Figure 4.8: target probability distribution  $\nu$

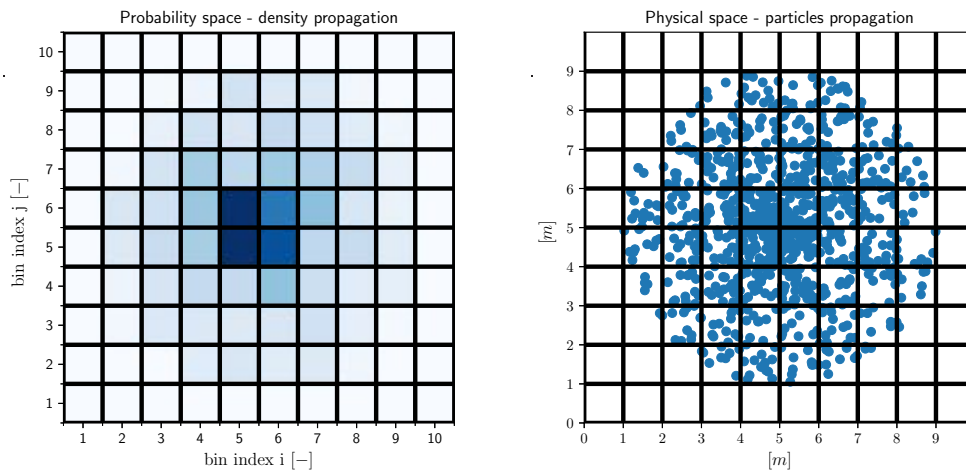


Figure 4.9: Iteration number  $k = 0$

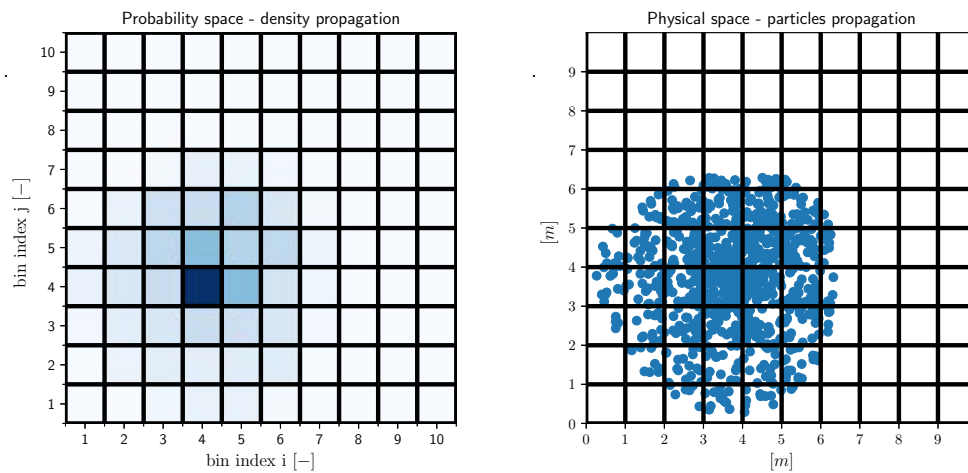


Figure 4.10: Iteration number  $k = 30$

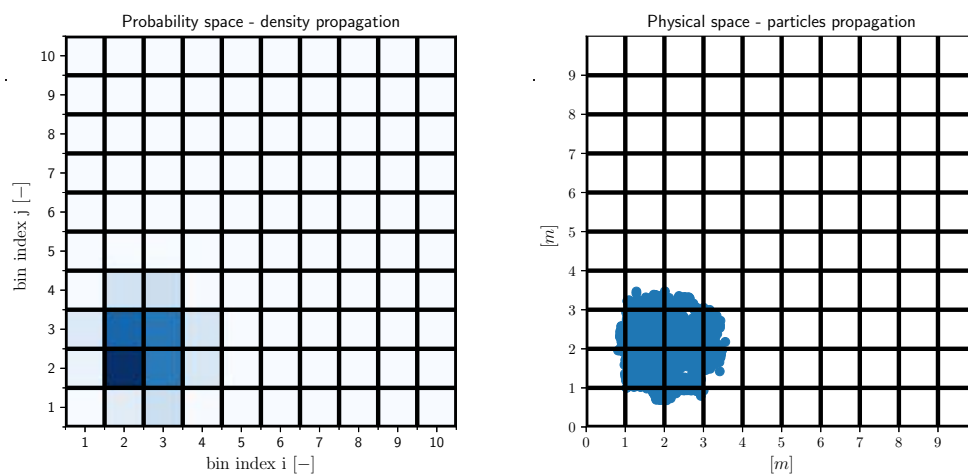


Figure 4.11: Iteration number  $k = 200$

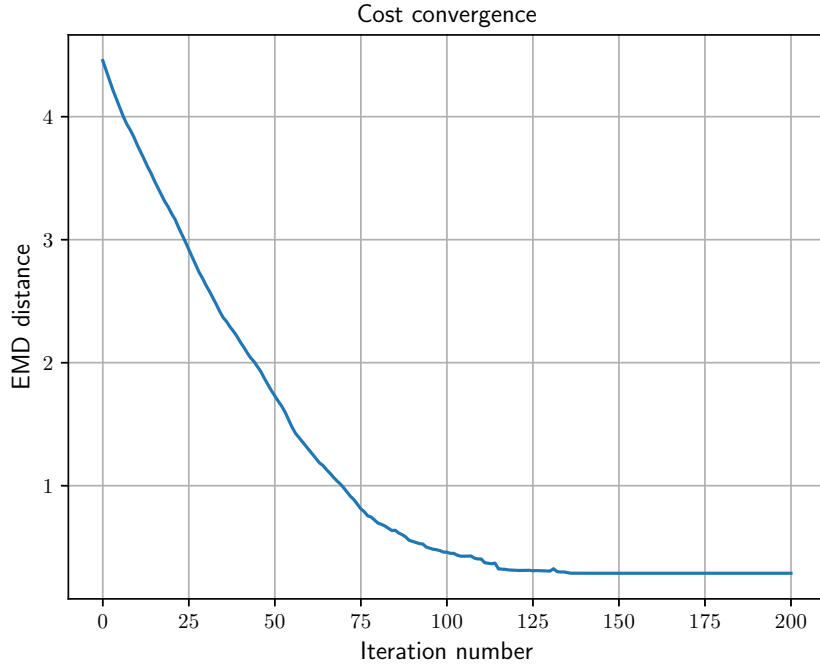


Figure 4.12: cost convergence

It can be seen that, starting from a random distribution over the workspace, the control logic is able to steer the particles towards a desired distribution. In the simulation  $N = 1000$  particles are considered. It is interesting to notice that the probabilistic control logic is the same irrespective of the actual number of particles. As a consequence, the dimensionality of the optimization problem does not scale with the number of the particles but with the number of grid elements. The cost convergence plot 4.12 shows an exponential convergence to a steady-state value. After roughly 125 iterations the algorithm is not able to reduce the distance anymore. This is a consequence of the dynamic model assumed for the density function. A specific actuator has influence all over its row and determines a flow for each internal element in this row, hence not every target distribution is achievable with zero convergence error. Possible solutions to this problem are to extend the time horizon of the optimization problem across multiple steps or to increase the number of the actuators thus refining the grid.

# Chapter 5

## DSENDSEdu model

The GI system presents several challenges from the modeling point of view. It is a very large multi-body system in which the constitutive elements interact along time scales that are orders of magnitude different. In the previous chapters control strategies for the granular particles at the micro-scale have been addressed, in the following a complete environment will be developed to model and simulate the whole system in the DSENDSEdu simulation framework. DSENDSEdu is the educational version of DARTS (Dynamics Algorithms for Real-Time Simulation), a high-fidelity, flexible multi-body dynamics simulator used for real-time hardware-in-the-loop design, integration and testing of spacecraft flight software. The DARTS simulator is based upon state-of-the-art computational algorithms from the Spatial Operator Algebra mathematical framework for multi-body dynamics. The Spatial Operator Algebra is a mathematical approach for modeling the dynamical behavior of complex, articulated collections of bodies interacting with each other in free-space or in contact with the environment.

### 5.1 System modeling and assumptions

This system is modeled as a large ensemble of rigid bodies in space whose equations of motion have been derived in chapter 2. A virtual chief spacecraft is defined to mark the relative reference for the deputy spacecrafts (i.e. the sub-aperture patches) and defines the position of the orbiting reference frame  $\mathcal{F}_O$ . The chief is orbiting in GEO and its dynamics is governed by the associated mean motion (i.e.  $\omega_O \propto 10^{-5} \frac{rad}{s}$ ).

The sub-aperture patches are modeled as large rigid disks and are equipped with linear and angular actuators. Their relative dynamics with respect to the chief spacecraft is described in chapter 2. In this sense, they will be also called deputy

spacecrafts following the formation flying control literature nomenclature. The cloud of grains (particles), modeled as micrometric rigid hemishperes as in chapter 3, is confined inside each patch.

The sparse-aperture array is formed by the deputies flying in formation. A control strategy for the spacecrafts at the macro-scale is derived. The controller is designed so that the deputies perform a certain trajectory around the chief spacecraft while pointing a target. Their dynamics is faster than the orbital motion but it is still in the same order of magnitude. On the other hand, the dynamics of the grains is order of magnitude faster then the previous ones, due to the very small mass and inertia of the particles and the nature of the interacting forces. Performing a complete simulation is a complex task for numerous reasons. Due to the large difference in the time scales the problem is numerically stiff and a large integration step could lead to divergence, on the other hand a complete simulation with a time step in accordance with the dynamic of the particles will lead to very long computations. In addition, the number of interacting rigid bodies is in the order of  $N \propto 10^4$  and this increases even further the computational load. Finally, at every time integration step the force fields and the mutual interactions have to be taken into account. However, due to the high computational performance of the DSENDSEdu engine a successful preliminary simulation is carried out.

## 5.2 Model structure and implementation

The multi-body system implemented in the simulation is intrinsically hierarchical as its dynamics can be decomposed in the dynamics of each element at different scales.

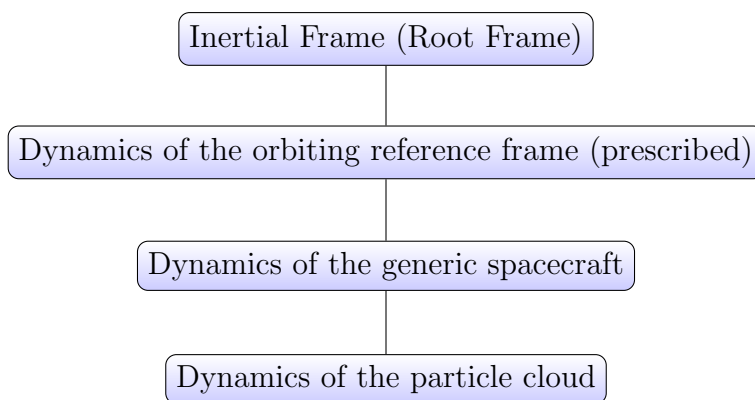


Figure 5.1: Block diagram of the different dynamics involved

Even if the bodies are all disconnected from each other it is useful to divide the

dynamics into different scales as shown in the diagram above. It will be shown that the particles experience much faster dynamics than the one of the spacecrafts around the orbiting reference frame  $\mathcal{F}_O$ . Furthermore, the controlled spacecraft dynamics is faster than the propagation of the orbiting reference frame. Due to this structure, there are many options in which the multi-body system can be implemented in the simulation.

The DSENDSEdu simulator allows to refer the state of a generic body to a parent body or equivalently relate the frames rigidly connected to these bodies. A special parent body is the root frame that is inertially fixed. The hierarchical structure of the system can be exploited referring each subsystem to a parent body in cascade. In particular, the particles are referred to their respective containing spacecraft, each spacecraft to the orbiting reference frame and the orbiting reference frame to the root frame. In this way the multi-body system is connected in series. Another option is to refer every element directly to the inertial frame. These two approaches are explained briefly in the next two sections.

### 5.2.1 Open serial kinematic tree

The logic consists of constructing an open serial tree kinematic chain. a virtual reference body called CS (Chief Spacecraft) is connected via a `Full16Dof` constraint (i.e. it is physically unconstrained) to the inertial root frame. CS is the landmark spacecraft following a circular orbit and it is the origin of the orbiting reference frame  $\mathcal{F}_O$ . Spacecrafts bodies SC, whose body-fixed frame is  $\mathcal{F}_S$  are all child bodies of CS with the same `Full16Dof` joint. Finally the particles are referred to their respective spacecraft via the same joint. In this way, it is possible to assign and extract the relative dynamics directly through the DSENDSEdu function `parentHinge` that computes the relative state between a 'child' body and its 'parent', thus the relative dynamics is directly taken into account in the structure of the simulation without additional coding complexity. However, this approach is computationally heavy and a parallel arrangement would be more efficient.

### 5.2.2 Parallel kinematic tree

Since each element is not physically connected to others, it can be referred directly to the inertial root frame. In this way the kinematic solver sees a parallel structure where the kinematics of each element is referred to the absolute inertial frame via a `Full16Dof` joint. In other words, the inertial root frame is the parent body of each element of the system (i.e. CS, SC and the particles). This logic is computationally lighter for the solver due to the fact that the multi-body solver 'sees' only one parallel layer of elements instead of successive nested elements as in the serial approach.

However, the relative dynamics of each subset of the system is needed to simulate multi-scale interactions (i.e gravitational forces, confinement forces, disturbances) that are dependent on the relative state of one subsystem with respect to another. Sequential relative transformations are performed at each step of the simulation using the tools provided by the Spatial Operator Algebra to capture the relative states and consequently compute the mutual interactions.

```

*****
      BODIES
*****

```

Body	Parent	Hinge	Q	U	Modes	Act. #	Sens. #
CS	ROOT	FULL6DOF	0/7	0/6	0	1	0
SC_0	ROOT	FULL6DOF	7/7	6/6	0	4	0
SC_0_particle_0	ROOT	FULL6DOF	14/7	12/6	0	4	0
SC_0_particle_1	ROOT	FULL6DOF	21/7	18/6	0	4	0
SC_1	ROOT	FULL6DOF	28/7	24/6	0	4	0
SC_1_particle_0	ROOT	FULL6DOF	35/7	30/6	0	4	0
SC_1_particle_1	ROOT	FULL6DOF	42/7	36/6	0	4	0

Figure 5.2: Parallel model

## 5.3 Force fields implementation

### 5.3.1 Gravitational model

A spherical gravitational field that simulates the presence of a main primary body (i.e. Earth) is implemented and it is centered at the inertial reference frame (`RootFrame`). Hence, this reference frame can be considered an ECI frame (Earth Centered Inertial), it is labeled 'J2000' in the simulation snapshots. The gravitational effects are felt by each element. Although being a simple model, it is a useful starting point to simulate a GEO orbit.

### 5.3.2 Particle force fields

The nature of the particle force fields implemented is local in the sense that it is related to each spacecraft container. The model for the deputies follow the concept design described in the first chapter. Therefore the presence of a buffer gas inside each container is simulated. This idea allows to add damping and dissipation during the cloud control stages. In this simulation, the inert gas enters the dynamics of each particles providing damping. The Stoke's damping model is adopted, as a consequence, the dissipative forces have the form  $\underline{F} = -K_{d,l} \underline{\rho}_P^S$ , where the damping force depends on the relative velocity of the particle as seen by the spacecraft body-fixed frame  $\mathcal{F}_S$ . This model is motivated by the low-inertia of the particles. A

similar rotational damping is also introduced based on the relative angular velocity  $\underline{\mathbf{T}} = -K_{d,t} {}^S \underline{\boldsymbol{\omega}}^P$ . The confinement and shaping of the cloud is achieved using a combination of electrodynamic and optical trapping. Two models for these interactions are developed. A force of the form  $\underline{\mathbf{F}} = -K_s \underline{\boldsymbol{\rho}}_P$ , that attracts each particle towards the center of the SC element, is the model adopted for the electrodynamic trapping. This interaction forces each particle to oscillate around the point of minimum potential where the force is zero. The mutual repulsive force due to the charge that each particle carries is implemented in the form  $\|\underline{\mathbf{F}}\| \propto \frac{K_{rep}}{r}$ , this is the first-order interaction that a system of charged particles experiences, where  $r$  is the relative distance between a pair of particles. To simulate the optical realignment of the particles, the same laser-particle interaction model described in chapter 3 is used. The laser light is assumed spatially uniform and it points in the same direction as the x-axis of the SC body-fixed frame  $\mathcal{F}_S$ . The laser light changes the angular and linear momentum of the particles. The flat surface realign towards the light direction without global feedback control laws due to the presence of rotational damping.

Symbol	Property	Value	Units
$K_s$	spring-like confinement constant	$1.25 \cdot 10^{-8}$	$N/m$
$\mu_{Ar}$	Argon viscosity	2.1	$Pa \cdot s$
$K_{d,l}$	Stoke's damping constant	$4.95 \cdot 10^{-6}$	$N \cdot s/m$
$K_{d,t}$	Stoke's rotational damping constant	$2.8 \cdot 10^{-23}$	$N \cdot m \cdot s$
$I$	Light intensity	$1 \cdot 10^6$	$W/m^2$

Table 5.1: particles force field parameters

## 5.4 Formation control scheme

The DSENDSEdu simulation environment allows to study the interconnections between the system of spacecrafts at the macro-scale and the system of particles at the micro-scale. A formation controller is derived for the relative dynamics of the deputies with respect to the chief. The position with respect to  $\mathcal{F}_O$  ('ORF' in the simulation snapshots) is controlled with a linear optimal controller scheme that exerts a force on the spacecraft SC based on its relative state. The controller is tuned using the Clohessy-Wiltshire-Hill equations derived in chapter 2. It can be noticed that in the simulator the dynamics is not linearized and the validity of the CWH assumptions must be tested. The aim of the control strategy is to formation-fly the spacecrafts to obtain a very large synthetic aperture made by granular sub-aperture patches. The spacecraft's physical parameters are summarized in table 5.2

Symbol	Property	Value	Units
m	mass	100	Kg
-	shape	cylinder	-
r	radius	10	m
h	height	1	m
$J_x$	inertia component	$5 \cdot 10^3$	Kg · m <sup>2</sup>
$J_z$	inertia component	$2.5 \cdot 10^3$	Kg · m <sup>2</sup>

Table 5.2: Spacecraft physical properties

### 5.4.1 Validation of the linearized gravitational model

A check on the validity of the linearized equations of the relative orbits is performed in the fully nonlinear gravitational model implemented in the simulator. Although perturbation effects such as  $J_2$  are not taken into account, the nonlinear model fully exploits and propagates the differential gravity gradients. The orbital parameters are shown in table 5.4.

Symbol	Property	Value	Units
-	orbit	GEO	-
-	type	equatorial	-
$\mu$	gravitational parameter	$3.99 \cdot 10^{14}$	m <sup>3</sup> /s <sup>2</sup>
R	$\mathcal{F}_O$ orbital radius	$42 \cdot 10^6$	m
$\omega_O$	mean motion	$7.33 \cdot 10^{-5}$	rad/s

Table 5.3: Orbital parameters

The trajectories and time-histories of three spacecrafts are simulated below with no control action applied. It is expected that the relative components behave as the solution of the homogeneous CWH equations. In particular, the radial ( $x$ ) and along-track ( $y$ ) coordinates are coupled and subjected to a linear drift while the cross-track ( $z$ ) evolves as a decoupled harmonic oscillator with frequency  $\omega_O$ . The relative initial velocity in the simulation is set to zero while the relative positions are random numbers within a 200 [m] range. The analytical solution for this case is:

$$x(t) = 4x_0 - 3x_0 \cos(\omega_O t) \quad (5.1)$$

$$y(t) = -6\omega_O x_0 t + y_0 + 6x_0 \sin(\omega_O t) \quad (5.2)$$

$$z(t) = z_0 \cos(\omega_O t) \quad (5.3)$$

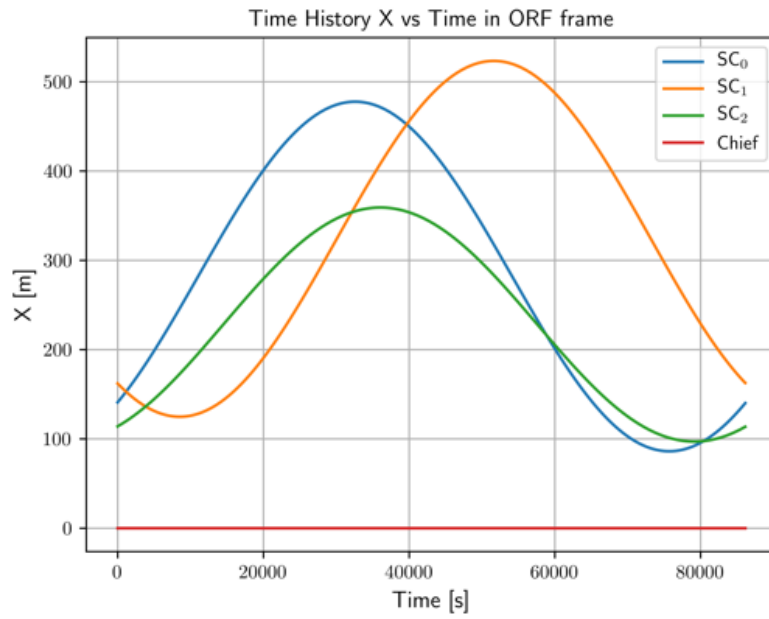


Figure 5.3: Radial Coordinate - DSENDSEdu Simulation

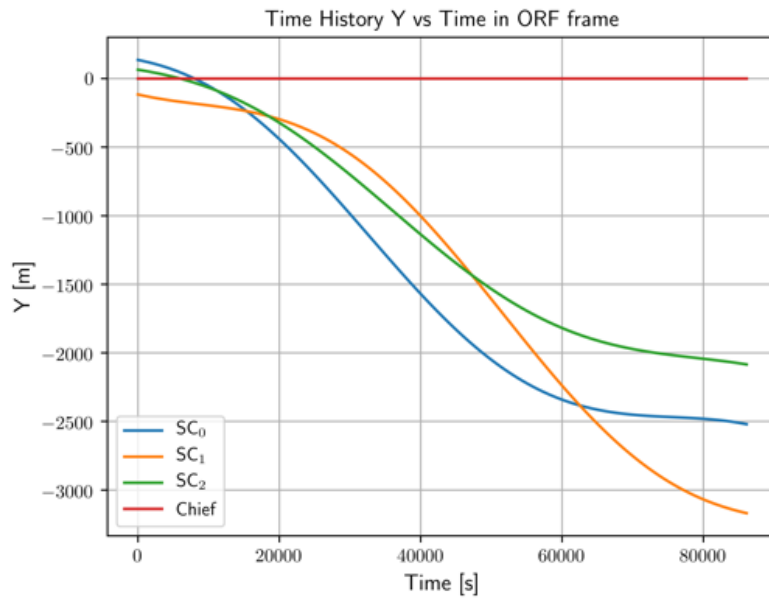


Figure 5.4: Along-track Coordinate - DSENDSEdu Simulation

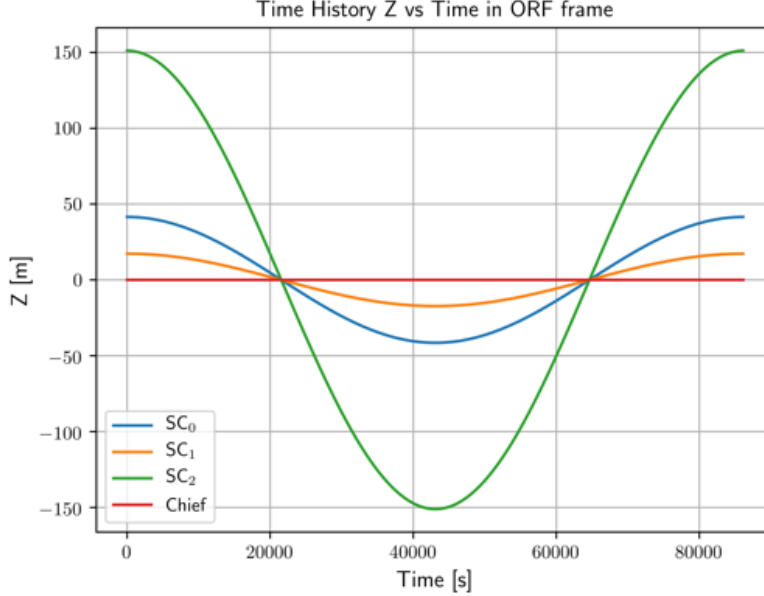


Figure 5.5: Cross-track Coordinate - DSENDSEdu Simulation

### 5.4.2 LQR-based leader tracking

The previous section proved that CWH equations are a valid approximation for the dynamics of the spacecrafts relative to the orbiting reference frame  $\mathcal{F}_O$  within a certain range. Using linear optimal control theory a LQR controller can be used to track the position of  $\mathcal{F}_O$ . It is simple to implement such a controller due to the fact that the only parameters needed as inputs are the mean motion of the orbit (i.e.  $\omega_O$ ) and the mass of the spacecrafts (i.e.  $m_S$ ) as can be seen from equation 2.22 in chapter 2. Regarding the control structures some considerations on the weighting matrices must be done. Usually in the formation flying literature [1] the weighting matrices are rescaled:

$$[Q] = \begin{bmatrix} [Q_{vel}] & [0]_{3 \times 3} \\ [0]_{3 \times 3} & [Q_{pos}] \end{bmatrix} \quad [Q_{vel}] = w_{vel} \frac{1}{\omega_O^2} [I]_{3 \times 3} \quad [Q_{pos}] = w_{pos} [I]_{3 \times 3} \quad (5.4)$$

$$[R] = \frac{1}{\omega_0^4} [I]_{3 \times 3} \quad (5.5)$$

In this way, each term of the quadratic running cost defined as  $L = \frac{1}{2}(\mathbf{x}^T [Q] \mathbf{x} + \mathbf{u}^T [R] \mathbf{u})$  has the same dimension  $[m]^2$ . It is thus easy to weight position and velocity of the state of the relative orbit. The optimal LQR control law takes the state-feedback form  $\mathbf{u} = -[K]\mathbf{x}$ . In the following simulation a leader tracking trajectory is commanded to the spacecrafts. The leader is intended as the virtual

chief spacecraft and the origin of  $\mathcal{F}_O$ . The weights used are  $w_{vel} = 1, w_{pos} = 10^5$ . The spacecrafts relative position converges to the origin of  $\mathcal{F}_O$  within a fraction of the orbital period.

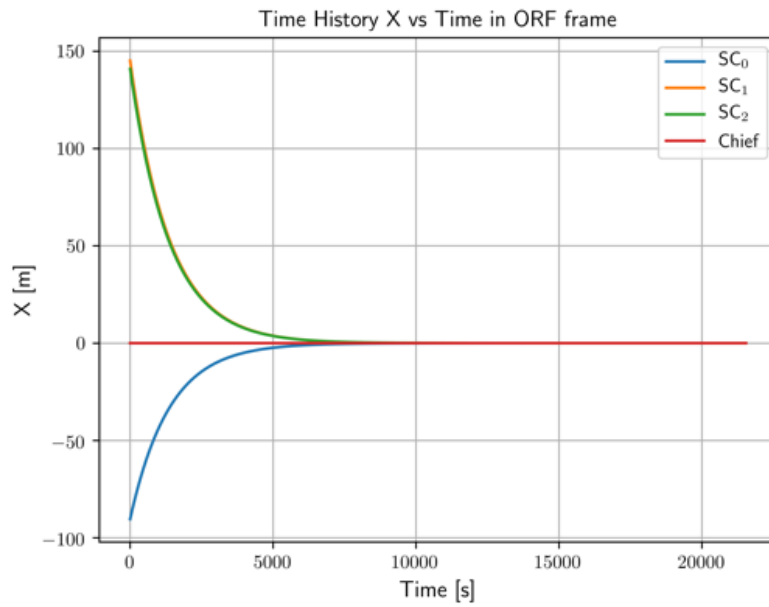


Figure 5.6: Radial Coordinate - LQR Controlled - DSENDSEdu Simulation

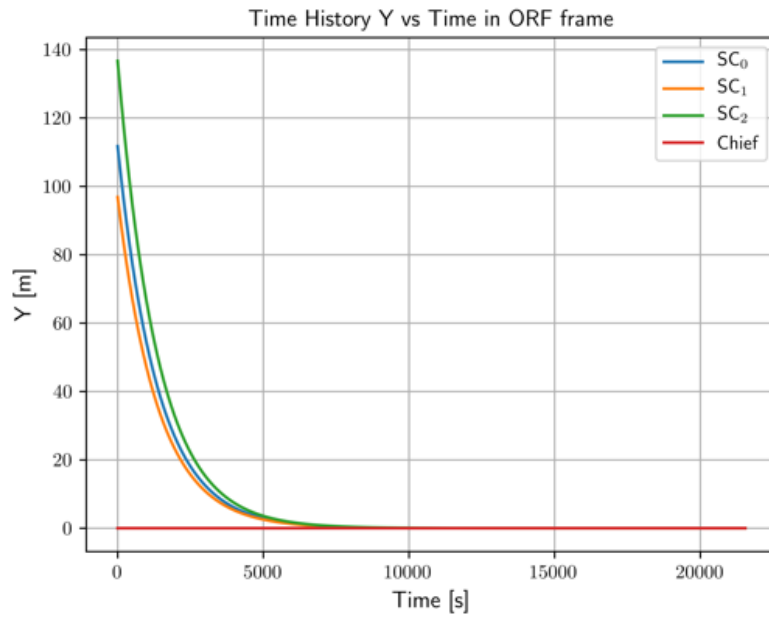


Figure 5.7: Along-track Coordinate - LQR Controlled - DSENDSEdu Simulation

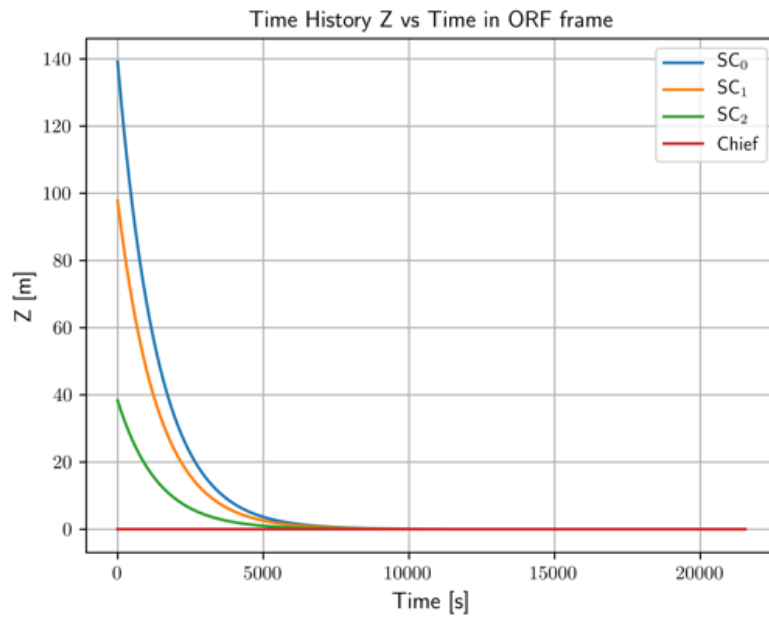


Figure 5.8: Cross-track Coordinate - LQR Controlled - DSENDSEdu Simulation

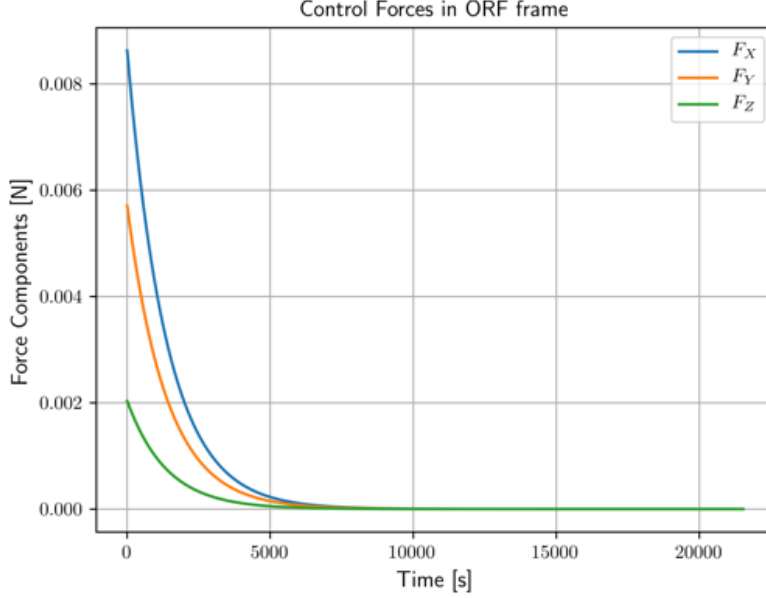


Figure 5.9: Control Actions - LQR Controlled - DSENDSEdu Simulation

### 5.4.3 LQR-based trajectory following

The main objective of the formation flying controller is to achieve trajectory tracking. The structure of the previous controller can be modified in order to follow a reference state trajectory. In this way, the objective of the controller is to minimize the error between the actual and the reference state. The control action takes the feedback form:

$$\mathbf{u} = -[K](\mathbf{x} - \mathbf{x}_{ref}) \quad (5.6)$$

The column vector  $\mathbf{u}$  represents the components of the control force in the orbiting reference frame  $\mathcal{F}_O$ . The control gain matrix  $[K]$  is obtained with the same weighting matrices  $[Q]$  and  $[R]$  used for the leader following of the previous section. Three spacecrafts are simulated and to each of them a reference state  $\mathbf{x}_{ref}$  is commanded. The reference state is defined in such a way that the spacecrafts perform a circular trajectory in the  $y$ - $z$  plane of  $\mathcal{F}_O$  at a specified angular velocity. The initial state is a random relative position within a specified range (i.e.  $200 [m]$  in this case) while the commanded radius of the circular reference trajectory is  $100 [m]$ . The angular velocity is a multiple of the orbital angular velocity (i.e.  $\omega_{form} = 8\omega_O$ ).

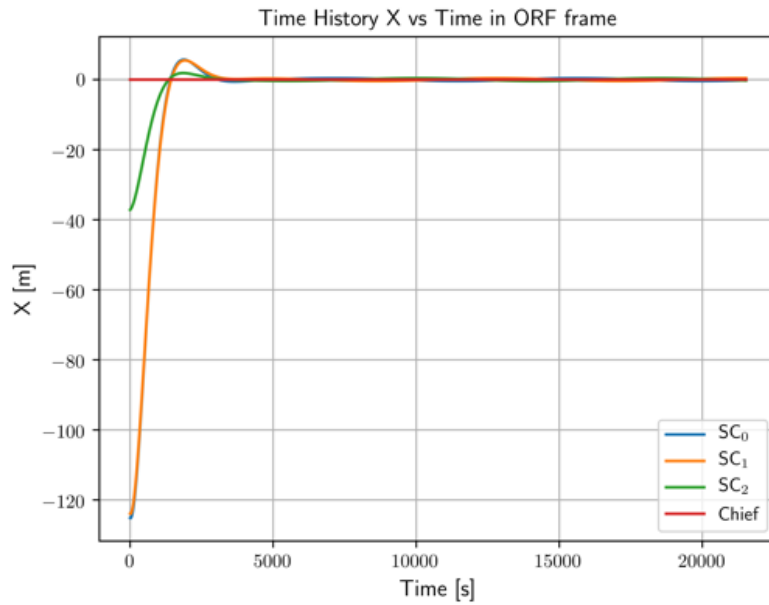


Figure 5.10: Radial Coordinate - LQR Tracking - DSENDSEdu Simulation

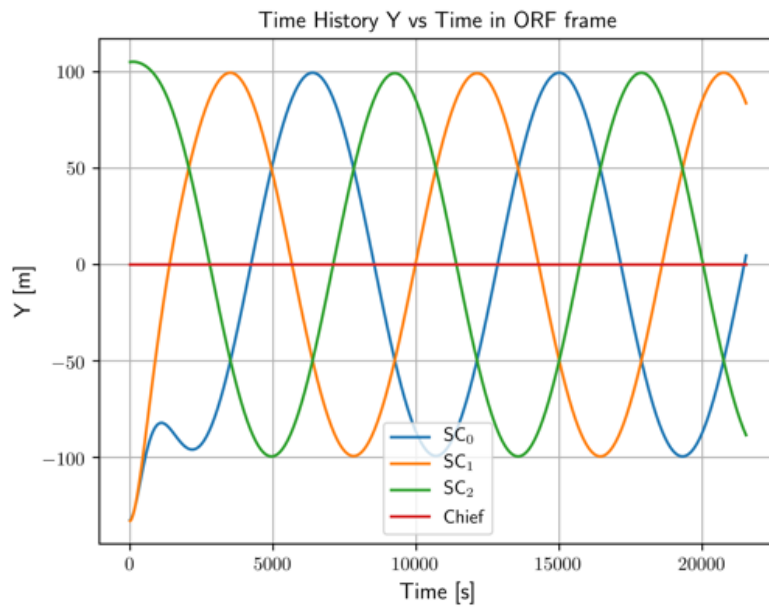


Figure 5.11: Along-track Coordinate - LQR Tracking - DSENDSEdu Simulation

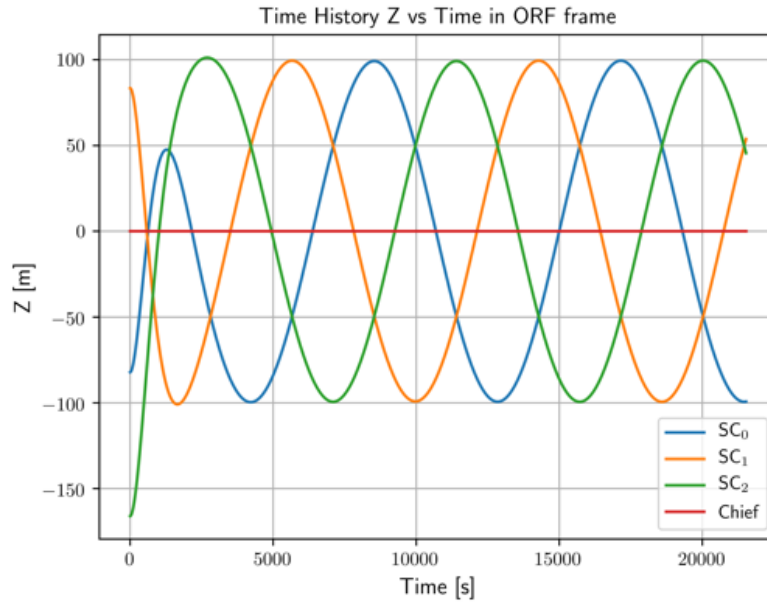


Figure 5.12: Cross-track Coordinate - LQR Tracking - DSENDSEdu Simulation

In the figures above, the relative coordinates are plotted with respect to  $\mathcal{F}_O$ . The Chief spacecraft trajectory is plotted to check that the simulator does not carry numerical errors. The radial coordinate in figure 5.10 converges to zero while the along-track and cross-track coordinates perform trajectory tracking after an initial transient.

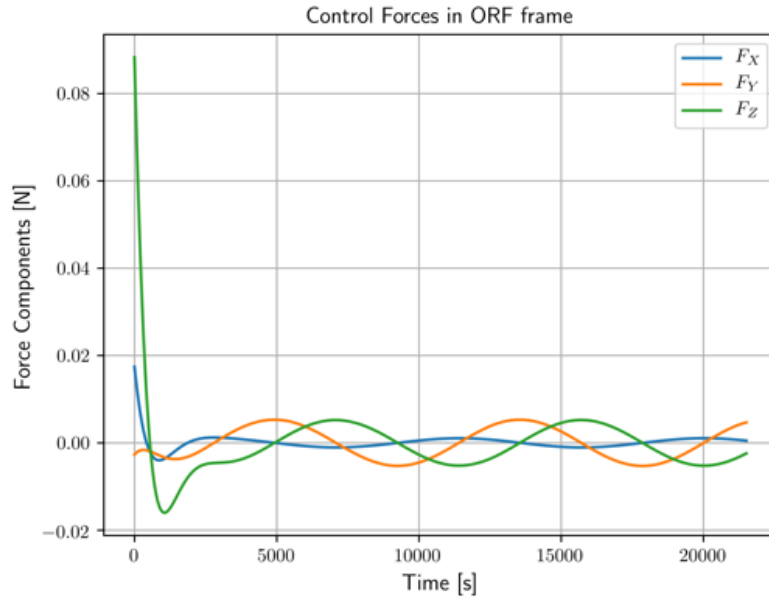


Figure 5.13: Control Actions - LQR Tracking - DSENDSEdu Simulation

In figure 5.13 the control actions for one of the three spacecrafts (i.e.  $SC_0$ ) are plotted. The components are expressed in frame  $\mathcal{F}_O$ . It is interesting to notice that the main effort is at the beginning when the controller brings the spacecraft from a random position closer to the reference trajectory. After this initial transient the trajectory following is performed with less effort. Furthermore, the control action in the radial direction is needed only to compensate the gravitational gradients and therefore is slightly lower than the other two.

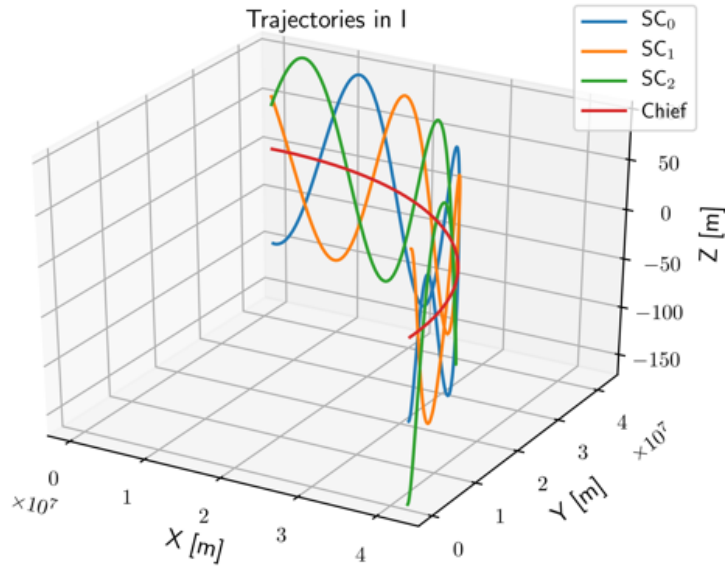


Figure 5.14: Trajectories in  $\mathcal{F}_I$  - LQR Tracking - DSENDSEdu Simulation

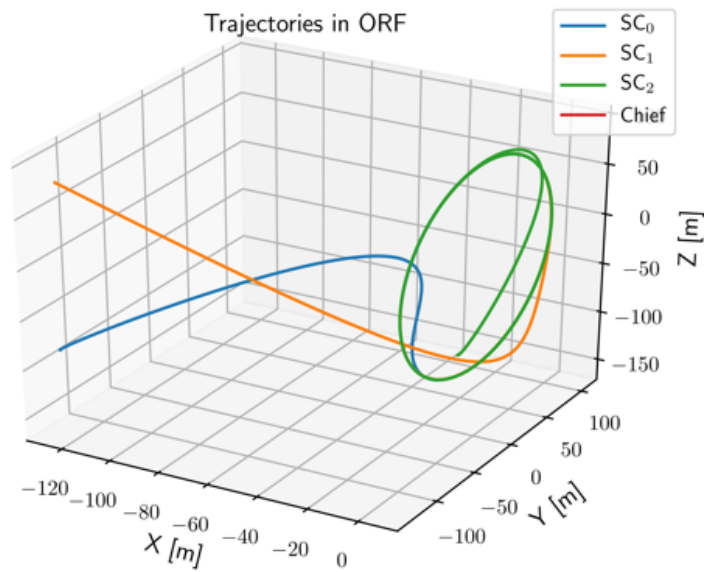


Figure 5.15: Trajectories in  $\mathcal{F}_O$  - LQR Tracking -DSENDSEdu Simulation

After an initial transient the spacecrafts perform a circular trajectory at the commanded velocity. The reference trajectories are designed so that the spacecrafts are phased of the same angle along the circular path.

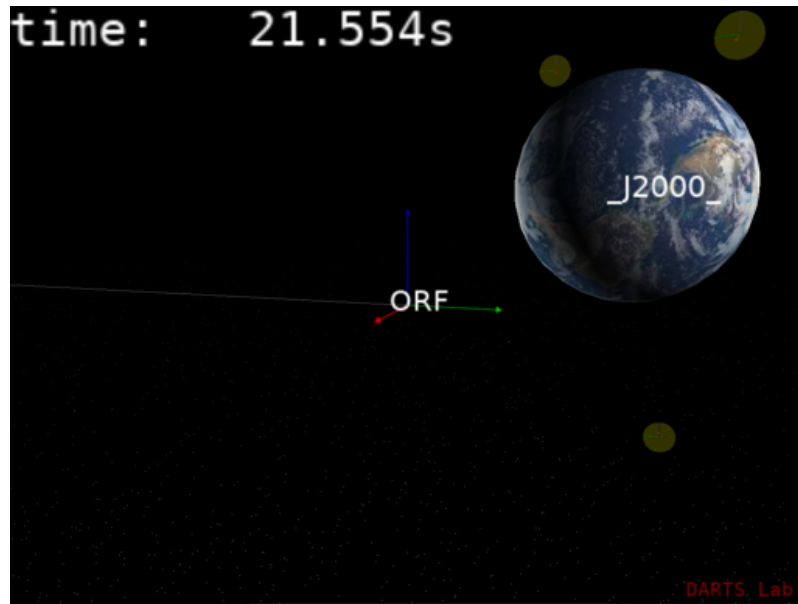


Figure 5.16: Initial Transient Steps - DSENDSEdu Simulation

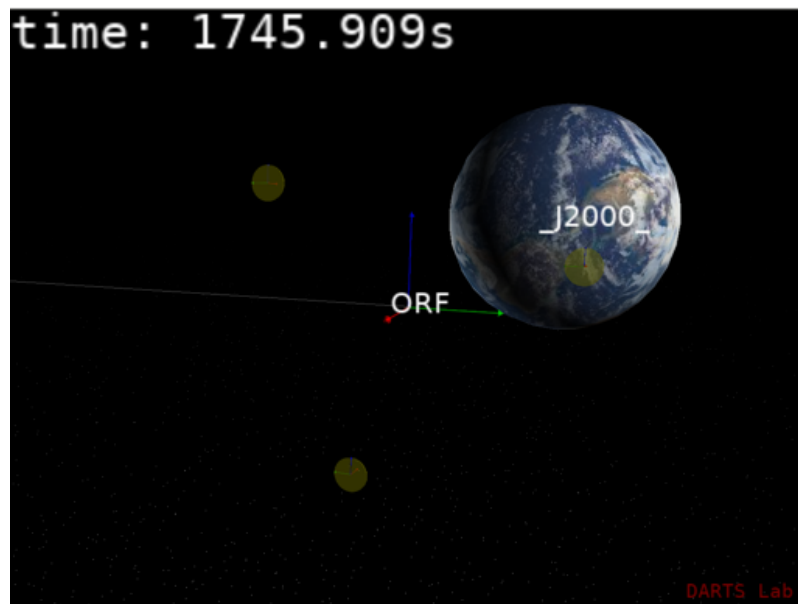


Figure 5.17: Formation Steady-State - DSENDSEdu Simulation

## Scalability and modularity

The architecture of the whole code and therefore of the controller as well is designed to be modular with respect to the number of spacecrafts and obviously to the number of particles. The reference planner automatically computes the relative trajectories irrespective of the number of spacecrafts. Only a snapshot of the simulation is plotted due to the fact that the control actions and relative trajectories are similar to the previous case.

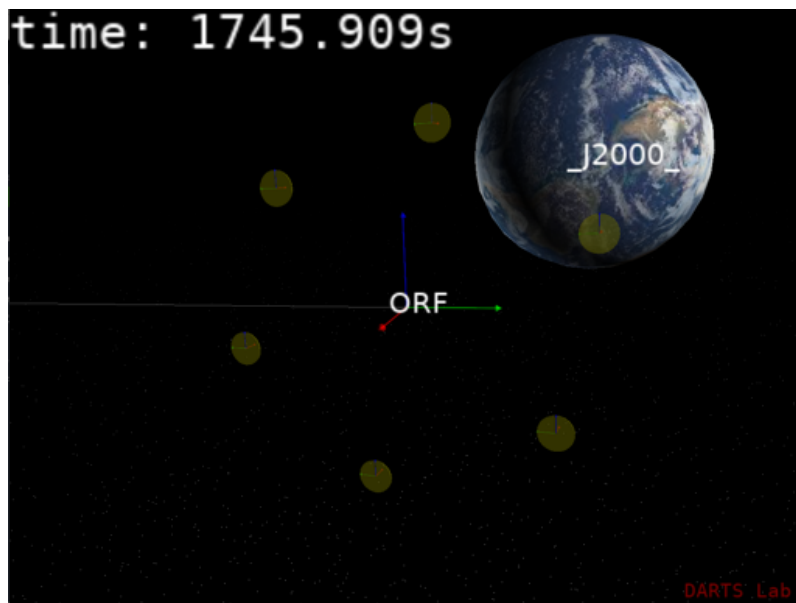


Figure 5.18: Formation Steady-State six spacecrafts - DSENDSEdu Simulation

## 5.5 Attitude control

A PD attitude control scheme is derived to solve the pointing problem of the deputies spacecrafts at the macro-scale. The granular medium remains trapped inside the deputies and a constant laser intensity forces the reflective surface of each granular element to be perpendicular to the pointing vector commanded at the macro-scale. The aim of the control system is to orient the x body-axis of the spacecraft to point in a specific direction (i.e. somewhere on the surface of Earth), this desired orientation is described with a quaternion  ${}^I\mathbf{q}_{ref}$ . The reference direction is selected so that each spacecraft in the formation is oriented towards the same point. This arrangement simulates the focusing control problem of the distributed telescope. The reflective surface is normal to the x body-axis. Once that the direction is chosen, the difference in rotation between the actual orientation and the reference can be com-

puted using the quaternion metric. The reference quaternion can be expressed as the quaternion product  $\otimes$  between two successive rotation. The difference quaternion is then obtained inverting the equation:

$${}^I \mathbf{q}_{ref} = {}^I \mathbf{q}_S \otimes {}^S \mathbf{q}_{ref} \rightarrow {}^S \mathbf{q}_{ref} = ({}^I \mathbf{q}_S)^{-1} \otimes {}^I \mathbf{q}_{ref} \quad (5.7)$$

The aim of the control system is to reduce the attitude and angular velocity error. A PD control law can be designed based on the vectorial part of the error quaternion (its first three elements) and on the angular velocity error in body frame.

$$\boldsymbol{\tau}_c = [K_p] \begin{bmatrix} {}^I q_{ref,1} \\ {}^I q_{ref,2} \\ {}^I q_{ref,3} \end{bmatrix} + [K_d] \begin{bmatrix} \omega_{ref,1} - \omega_1 \\ \omega_{ref,2} - \omega_2 \\ \omega_{ref,3} - \omega_3 \end{bmatrix} \quad (5.8)$$

Symbol	Property	Value	Units
$K_{p,i}$	proportional gain component	$1 \cdot 10^{-3}$	$N \cdot m$
$K_{d,i}$	derivative gain component	1	$N \cdot m \cdot s$

Table 5.4: Attitude controller gains

Usually a gyroscopic compensator is added while the simplest form of the controller is adopted here. The disturbance rejection is achieved by the feedback nature of the control law. The attitude controller is simulated in the following figures. The target point is located on the surface of Earth, hence the target angular velocity's norm is  $\omega_{ref} = \omega_O$  while the reference quaternion is obtained from the kinematic mapping described in chapter 2.

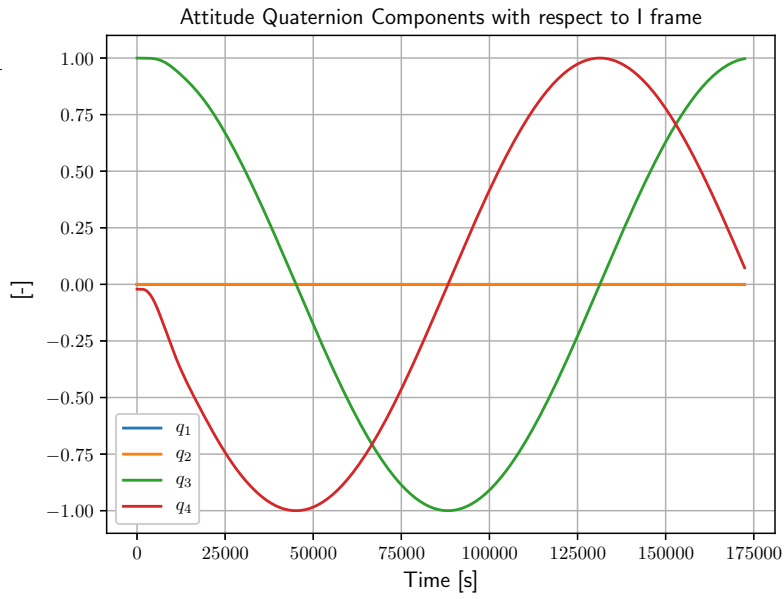


Figure 5.19: Attitude Parameters - DSENDSEdu Simulation

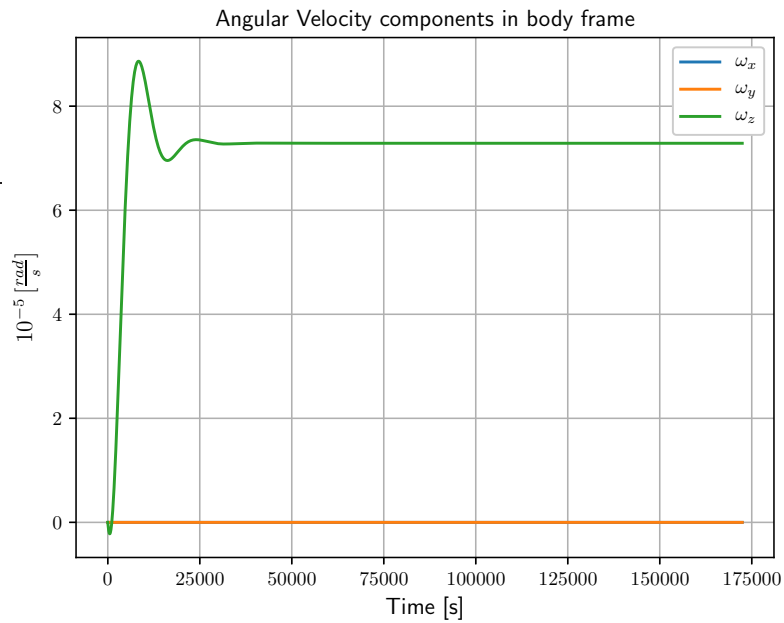


Figure 5.20: Angular Velocity - DSENDSEdu Simulation

The orbit lies in the x-y equatorial plane as a consequence the rotation is only around

the z-axis. Even if the spacecraft is performing out of plane formation flying tasks the angular difference does not change significantly and only an initial torque along the body-fixed z-axis is needed. Due to the nature of the control objective, the spacecraft angular velocity matches the orbit's angular velocity after a transient. In addition, gyroscopic torques are not present for in-plane motion, therefore the control torque eventually goes to zero. The control gains are tuned so that the settling time is a fraction of the orbital period.

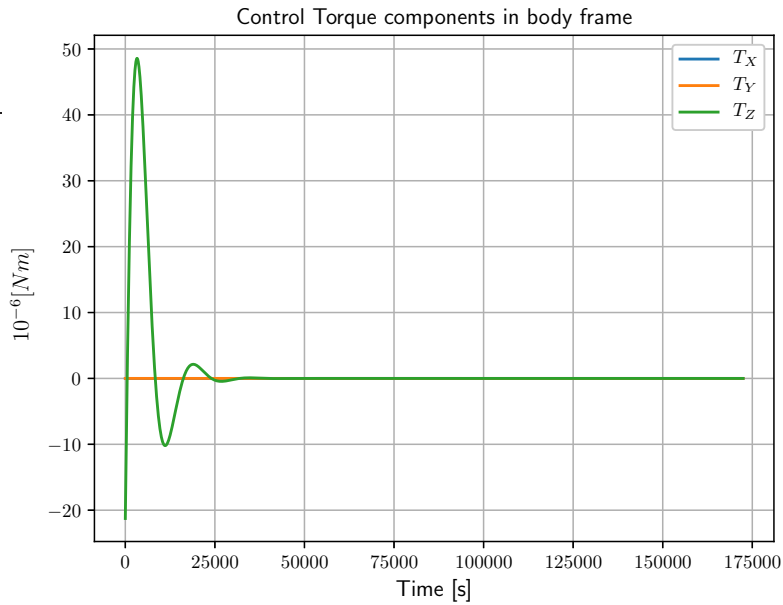


Figure 5.21: Control Torque - DSENDSEdu Simulation

## 5.6 Granular medium model

The optical system inside each sub-aperture patch (i.e. each spacecraft) is composed by a cloud of particles. The particles are endowed with a principal orientation perpendicular to which lies the reflective plane. The model and physical properties described in chapter 3 are used. The DSENDSEdu engine allows to model the three dimensional dynamics of the system of particles. The control system at the macro-scale affects the dynamics of the particles through the coupling terms derived in chapter 2. However, this coupling terms are very small and they have been neglected in chapter 3 and 4. The complete simulation environment implemented here allows to prove this assumption.

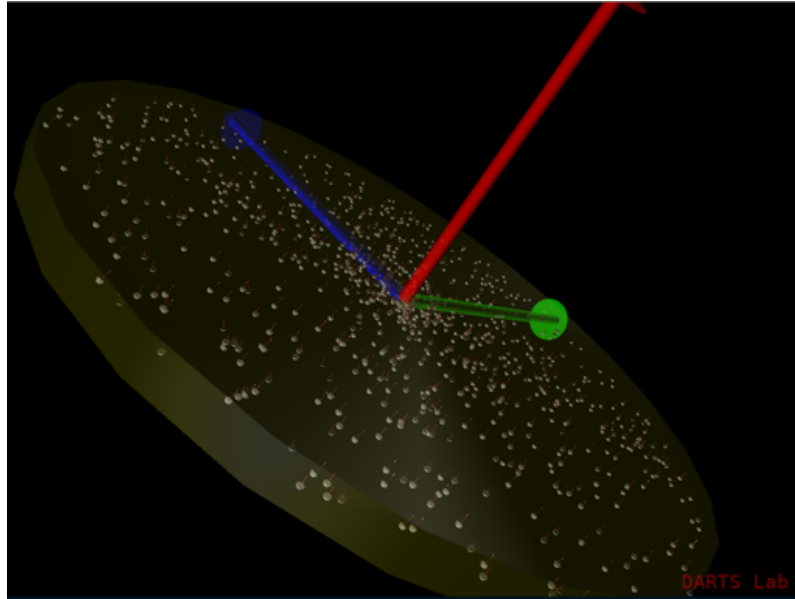


Figure 5.22: Granular Sparse-Aperture - DSENDSEdu Simulation

### 5.6.1 Realignment

While each sub-aperture is actuated at the macro-scale to solve the pointing problem, the grains at the micro-scale must be retargeted and kept with the right alignment. Thanks to the presence of the rotational damping introduced by the inert gas, all the grains will asymptotically point towards the laser direction.

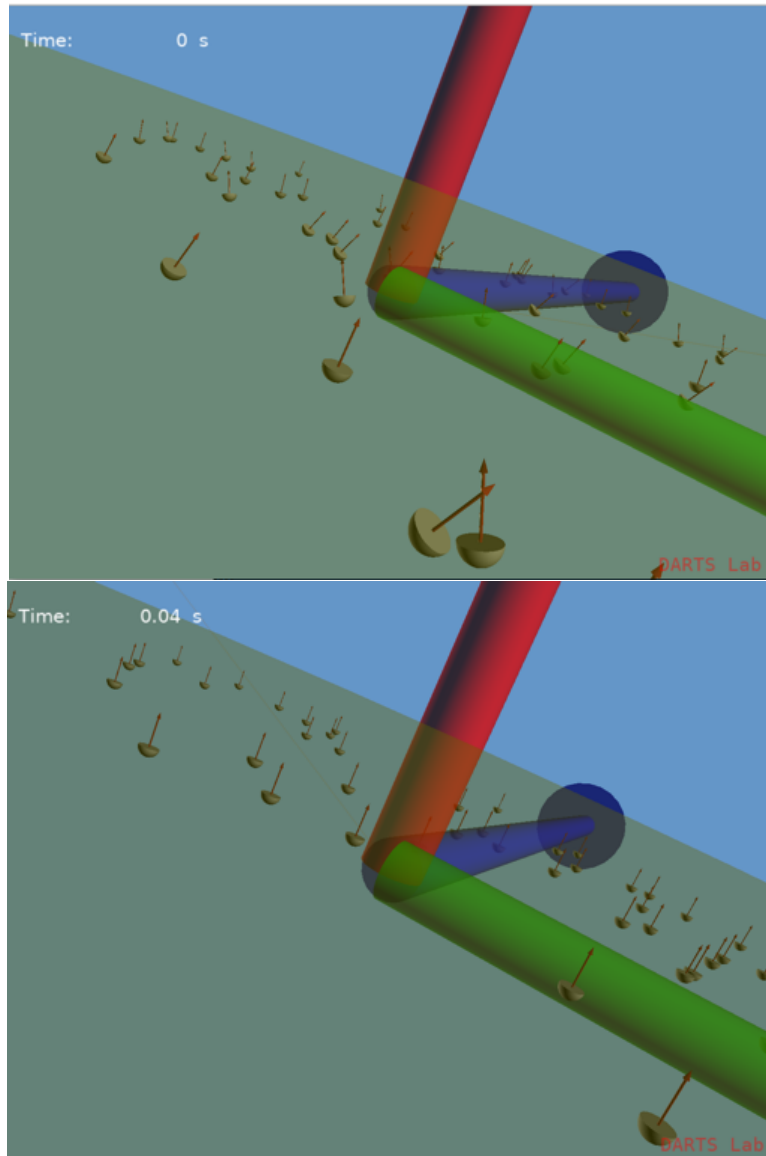


Figure 5.23: Realignment snapshots - DSENDSEdu simulation

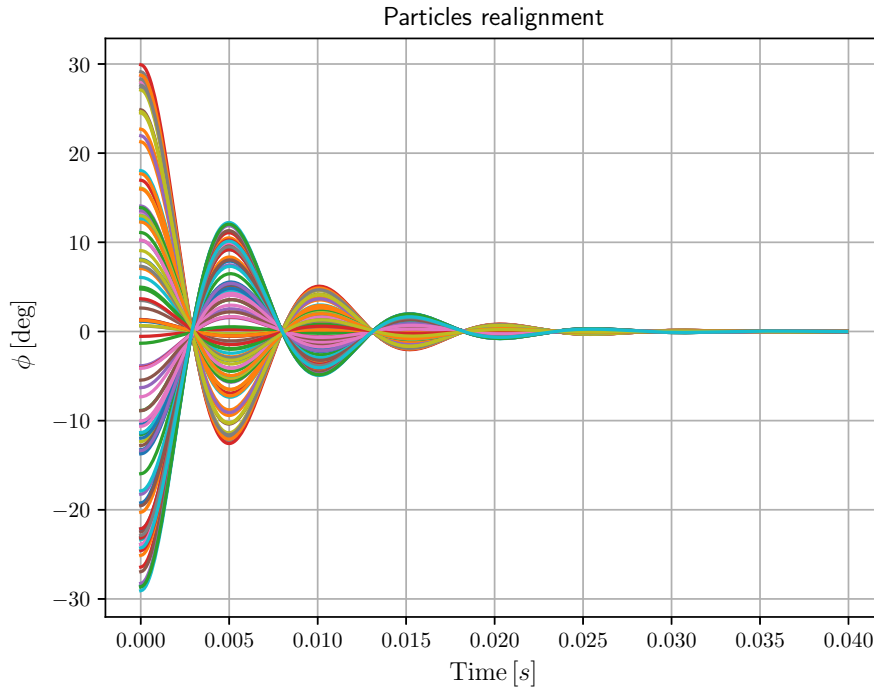


Figure 5.24: Particles realignment - DSENDSEdu simulation

The rotational and translational dynamics of the particles is order of magnitudes faster than the control bandwidth at the macro-scale. The rotational realignment is dominated by the frequency imposed by the laser source. As in chapter 3, the laser intensity is  $I = 10^6 [\frac{W}{m^2}]$  and the oscillation frequency is  $\omega_l \approx 600 [\frac{rad}{s}]$ . Therefore, the granular medium is rigidified in a small fraction of the reorientation time needed for the spacecraft at the macro-scale.

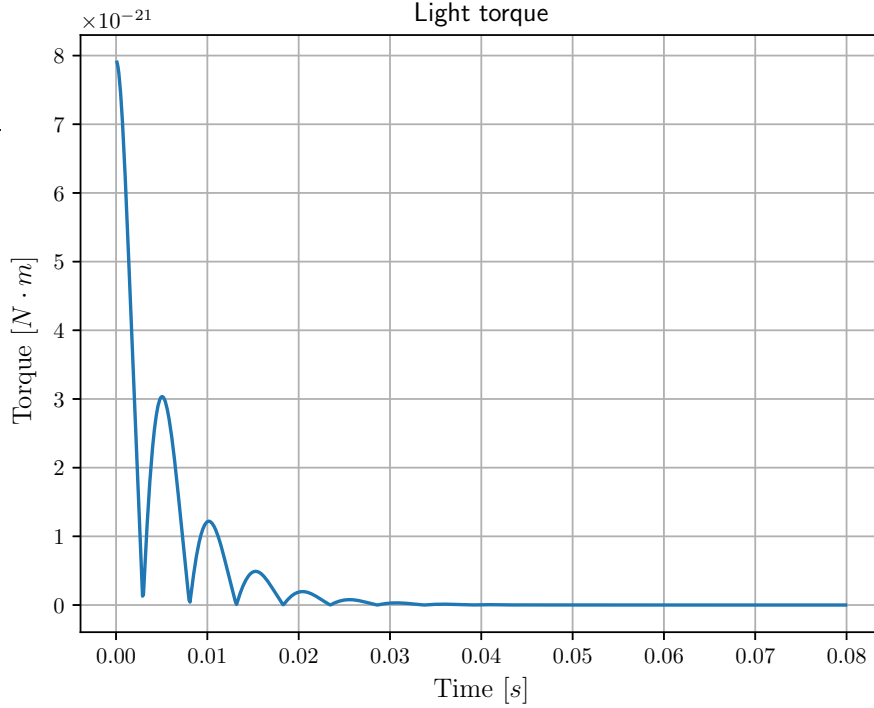
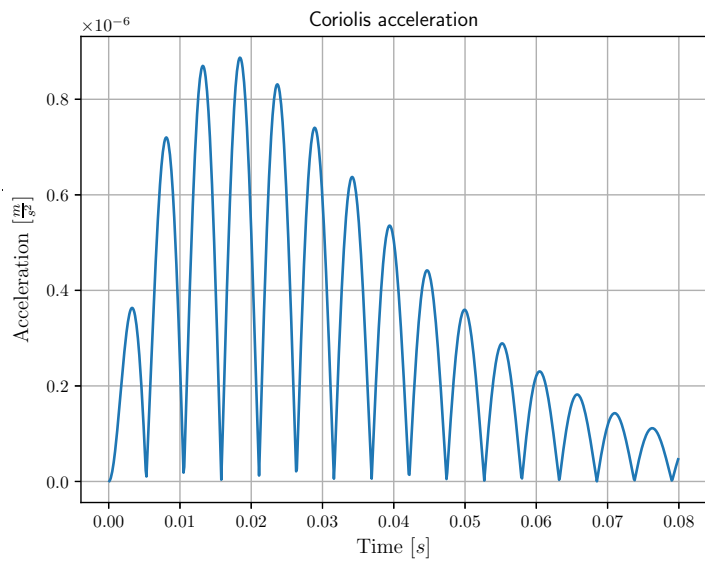
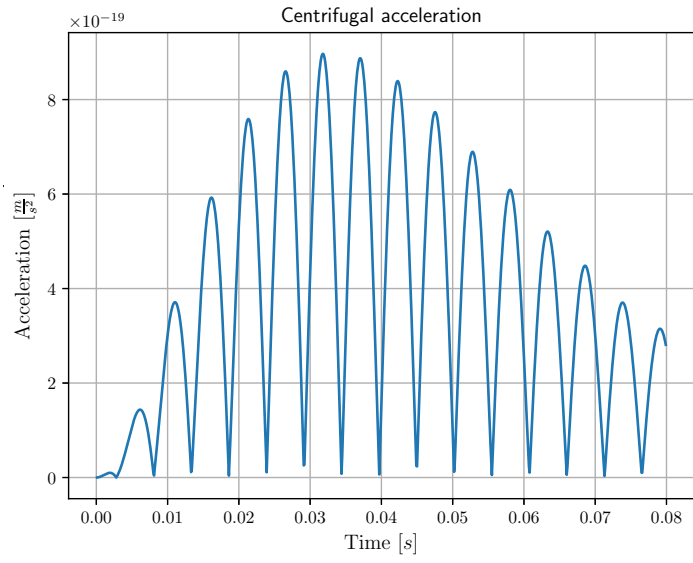


Figure 5.25: Light torque magnitude on a particle - DSENDSEdu simulation

### 5.6.2 Decoupling and confinement

The non inertial effects of the reference frame  $\mathcal{F}_S$  generate the accelerations described in chapter 2. These effects have been neglected in chapters 3 and 4, thus not considering that the spacecraft's attitude control system influences the particle dynamics through the angular velocity  ${}^I\boldsymbol{\omega}^S$ . In this complete simulation, the magnitude of the controlled angular velocity can be seen from figure 5.20. It is in the same order of magnitude of the orbital angular velocity  $\omega_O$  and eventually converges to it due to the attitude reference. The particles are trapped by the spring-like force field while retargeted in the light direction. At the macro-scale the attitude and formation control of the spacecrafts are active. This simulation allows to study the non inertial relative accelerations compared to the one observed from the spacecraft frame.



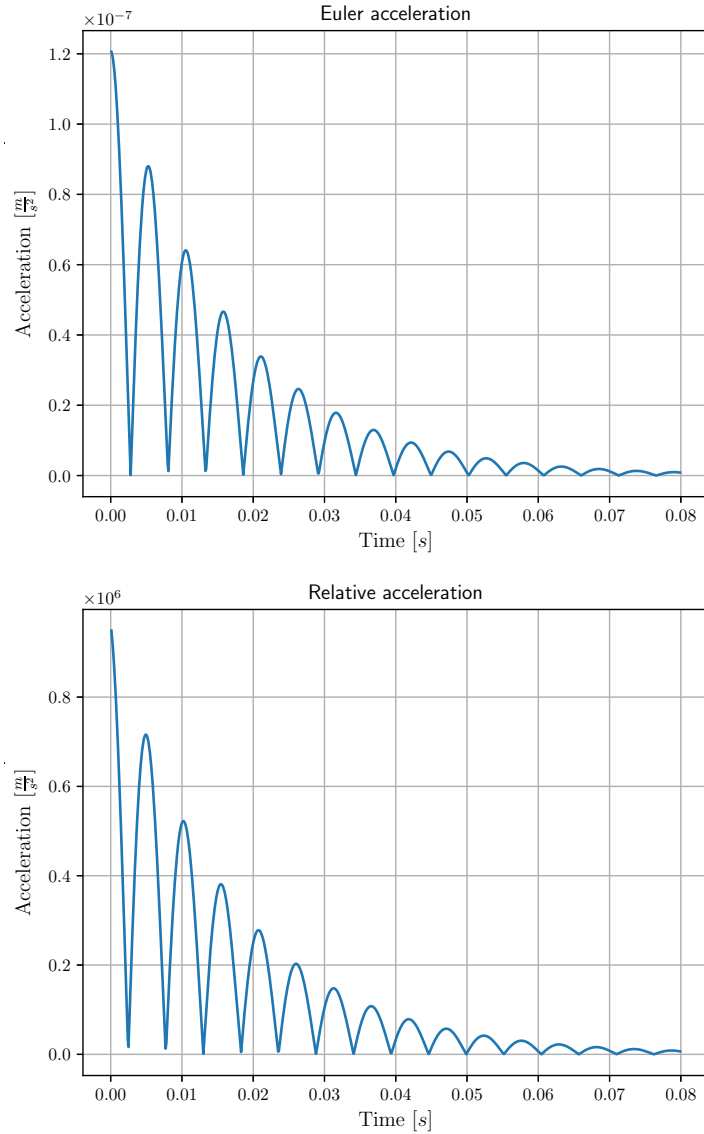
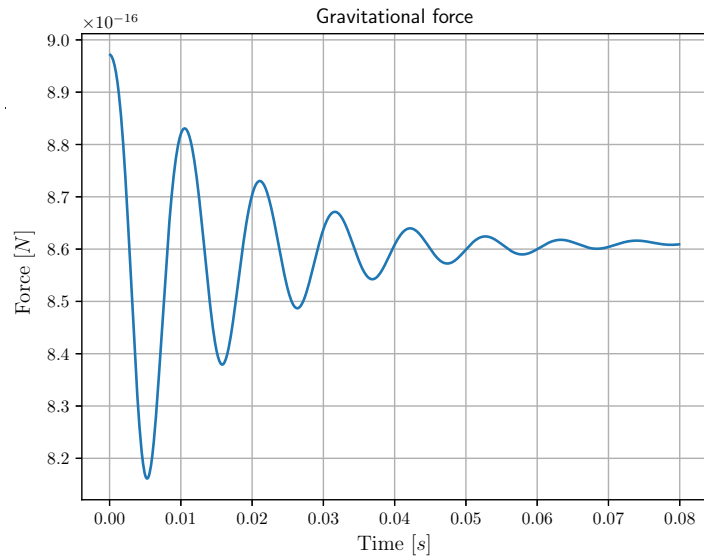
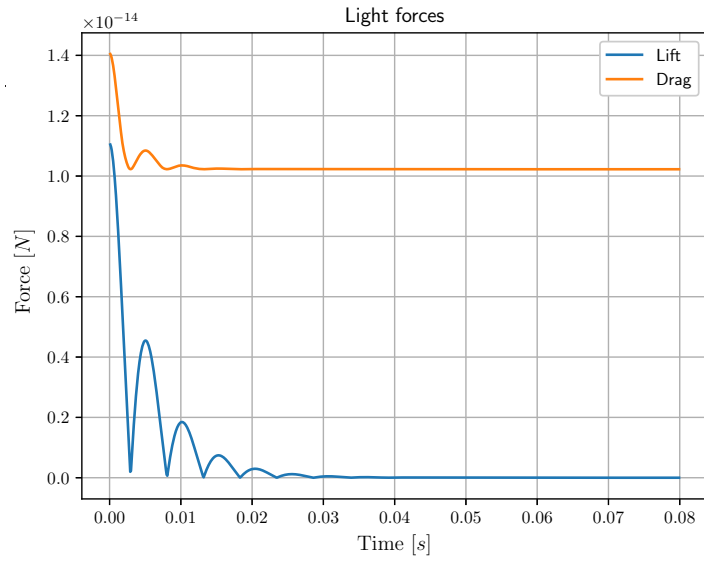


Figure 5.26: Acceleration terms magnitude comparison - DSENDSEdu simulation

The particle dynamics converges to the equilibrium condition in a very small fraction of the orbital period. The movement at the macro-scale does not influence this dynamics. The accelerations introduced by the non inertial effects are many order of magnitudes smaller than the acceleration observed by the spacecraft frame  $\mathcal{F}_S$  (i.e.  $\|\underline{\rho}_P^{SS}\|$ ). Hence, the approximation in the following equation is valid:

$$\|\underline{\rho}_P^{SS}\| \gg \|\underline{I}\dot{\underline{\omega}}^S \times \underline{\rho}_P\|, \|2\underline{I}\underline{\omega}^S \times \underline{\rho}_P^S\|, \|\underline{I}\underline{\omega}^S \times \underline{I}\underline{\omega}^S \times \underline{\rho}_P\| \quad (5.9)$$

Therefore, the hypothesis used to simplify the dynamics in chapter 3 is valid. Finally, the effect of the force fields introduced is plotted while the particles are experiencing realigning torques. The forces plotted are the one referred to one generic particle. The effects on the other particles is in the same order of magnitude. The light lift forces become null when the angle of attack is 0. The dominant forces are the one associated with the spring-like confinement.





# Chapter 6

## Conclusions and future work

### 6.1 Research outcome and discussion

The aim of this dissertation was to investigate the Granular Imager concept from the dynamics and control perspective. The general structure of the dynamic equations of the system in orbit have been reformulated in a way suitable for control applications at the macro and micro scale. The decoupling arguments studied in [5] have been used to divide the multi-scale problem and study the overall system separately. Then, the interconnections between the two systems have been simulated in the DSENDSEdu environment. The control problem at the micro-scale has been addressed in chapters 3 and 4. The nonlinearities introduced by the actuation model have been exploited to derive suitable control strategies. The kinematic properties of the switched geometrical laser control strategy have been investigated to develop a novel open-loop control law, thus partially addressing the challenging problem of multiple particles simultaneous realignment with a single input (source). The controllability of an underactuated system of multiple particles has been investigated with the result that the current layout fails the controllability test in a deterministic sense. This outcome has motivated the research carried out in chapter 4 on a simplified but analogous system. Starting from the stochastic model developed in [26], a novel approach to probabilistic control of largely underactuated systems has been proposed. The nature of the cost function, taken from Optimal Transport theory, allows the optimization problem to retain a single step horizon thus keeping the computational complexity on a reasonable level, while, at the same time, providing a global metric to minimize. Furthermore, the probabilistic nature of the control logic is insensitive to the number of states (particles) considered and is thus suited for very large scale system. In addition, the challenging problem posed by the global external nature of the actuation is solved and stochastic control over the distribution

of particles is achieved. In the last chapter, classical linear optimal control theory has been applied for motion control at the macro scale. The linearized set of equations obtained in chapter 2 has been proven to be a useful starting point for the sub-aperture formation controller. The flexibility and computational power of the DSENDSEdu simulator software has been used to create an environment where the whole system can be simulated to give a quantitative measure of the coupling and the entity of the forces involved.

## 6.2 Future work

In this dissertation the granular medium has been modeled as a large ensemble of micrometric rigid bodies with specific shape and material properties. The complex characteristics that make the granular materials unique have not been modeled. For example, a more refined modeling should include its peculiar properties such as cohesiveness, fluid behaviour, compactification and phase transformation capabilities [5]. However, theoretical formulations of these models suited for the control point of view are not present in literature.

Furthermore, the ray-tracing model of laser interaction should be enhanced considering the numerical integration of Maxwell's stress tensor as done in [12]. In this way, it is possible to take into account mutual reflections and interactions between the granular particles and the light field, it is interesting to notice that the particles are trapped by the fringes created by the optical field. A promising experimental layout allows to trap micrometric particles in two dimensions. Nevertheless, a dynamical model is not easy to derive and would be strongly configuration dependent thus not allowing modeling from the control theoretic standpoint.

The DSENDSEdu simulation code allows to gain preliminary insights on the behaviour of the system in space and it constitutes a basic model on which it will be possible to build more refined simulations. First of all, the trapping mechanism can be improved adding a more realistic electrodynamic model together with contact interactions between the particles. Second, the gravitational model is spherical and zonal harmonics, third body disturbances and other higher order effects are not considered. Third, the formation controller is derived from the Clohessy-Wiltshire-Hill equations that, although being simple and widely used [1], do not take into account nonlinear effects that a more refined simulation would require. Finally, the estimation and measurement part is not considered. At the macro-scale, models and algorithms to implement the formation state estimation similar to the one studied in [20] can be easily added as branches to the main structure of the code. A more challenging task is to derive an estimator for the cloud of particles. The DSENDSEdu software contain modules to simulate cameras used for optical

navigation during space missions. This package, together with the implementation of a tracking algorithm for multiple particles such as the one used in [21], will allow to simulate the complex feedback strategy to reshape and retarget the cloud of particles.

Finally, the stochastic control strategy of chapter 4 is based on a discretized single integrator dynamics. A more refined model should include inertial and nonlinear effects. The main theoretical problem even in the introduction of a simple double integrator model (i.e. adding inertia effects) is that a derivation of the probability density evolution is not trivial. Efforts in this direction will be object of future research.

# Bibliography

- [1] K.T. Alfriend et al. *Spacecraft Formation Flying, Dynamics, control and navigation*. Elsevier Astrodynamics, 2010.
- [2] A. B. Artusio-Glimpse, T. J. Peterson, and G. A. Swartzlander. “Refractive optical wing oscillators with one reflective surface”. In: *OPTICS LETTERS, Vol. 38, NO.6* (2013).
- [3] A. B. Artusio-Glimpse et al. “Rocking motion of an optical wing: theory”. In: *Appl. Opt. 53, I1-I9* (2014).
- [4] *assimulo Python library*. <https://jmodelica.org/assimulo/>. Accessed: 12/02/2019.
- [5] S. Basinger, G. Swartzlander, and M.B. Quadrelli. “Dynamics and Control of a Disordered System in Space”. In: *AIAA SPACE 2013 Conference* (2013).
- [6] R. Brockett. “Notes on the Control of the Liouville Equation. In: Control of Partial Differential Equations. Lecture Notes in Mathematics”. In: *Springer, Berlin, Heidelberg* (2012).
- [7] R. Brockett and N Khaneja. *On the Stochastic Control of Quantum Ensembles*. Springer US, 2000.
- [8] Y. Chen. *Modeling and control of collective dynamics: From Schrödinger bridges to Optimal Mass Transport*. University of Minnesota: Dissertation, 2016.
- [9] Tayfun Çimen. “State-Dependent Riccati Equation (SDRE) Control: A Survey”. In: *Proceedings of the 17th World Congress The International Federation of Automatic Control* (2008).
- [10] K. Elamvazhuthi, H. Kuiper, and S. Berman. “PDE-Based Optimization for Stochastic Mapping and Coverage Strategies using Robotic Ensembles”. In: *CoRR abs/1711.11018* (2017).
- [11] J. Gorman, Ar. Balijepalli, and T. LeBrun. *Feedback Control of Optically Trapped Particles*.

- [12] T. M. Grzegorzczuk, J. Rohner, and J Fournier. “Optical Mirror from Laser-Trapped Mesoscopic Particles”. In: *Physical Review Letters* (2014).
- [13] K.D. Hammett. *Control of Nonlinear Systems via State Feedback State-Dependent Riccati Equation Techniques*. Air Force Institute of Technology, Air University: Dissertation, 1997.
- [14] P.C. Hughes. *Spacecraft Attitude Dynamics*. New York: John Wiley, 1986.
- [15] A Jain. *Robot and Multibody Dynamics*. New York: Springer, 2011.
- [16] T.R Kane and D.A. Levinson. *Dynamics: Theory and Applications*. New York: McGraw-Hill, 1985.
- [17] V. Krishnan and S. Martinez. “Distributed optimal transport for the deployment of swarms”. In: *IWSCFF 17-17*. (2017).
- [18] L. Lanzoni. *Simulation of granular media in space environment*. Politecnico di Milano: Master’s thesis, 2016.
- [19] P. K. Menon et al. “Nonlinear Discrete-time Design Methods for Missile Flight Control Systems”. In: *AIAA Guidance, Navigation, and Control Conference, August 16-19, Providence, RI*. (2004).
- [20] E. Mettler, W.G. Breckenridge, and M.B. Quadrelli. “Large Aperture Space Telescopes in Formation: Modeling, Metrology, and Control”. In: *The Journal of the Astronautical Sciences, Vol. 53, No. 4* (2005).
- [21] N.P. Oxtoby et al. “Myriad Target Tracking in a Dusty Plasma”. In: *14th International Conference on Information Fusion* (2011).
- [22] D.K Parrish. *Applications of Nonlinear Control Using the State-Dependent Riccati Equation*. Air Force Institute of Technology, Air University: Thesis, 1995.
- [23] M.B. Quadrelli, S. Basinger, and E. Sidick. “Unconventional imaging with contained granular media”. In: *Proceedings Volume 10410, Unconventional and Indirect Imaging, Image Reconstruction, and Wavefront Sensing* (2017).
- [24] M.B. Quadrelli, S. Basinger, and G. Swartzlander. “Multi-scale Dynamics, Control, and Simulation of Granular Spacecraft”. In: *European Community on Computational Methods in Applied Sciences (ECCOMAS) Thematic Conference, Zagreb, Croatia, July 1-4, , 2013* (2013).
- [25] M.B. Quadrelli, P. Ius, and L. Lanzoni. “Modeling and Simulation of Trapping Mechanisms of Granular Media in Space”. In: *AIAA/AAS Astrodynamics Specialist Conference, Long Beach, California* (2016).
- [26] M.B. Quadrelli and S. Bandyopadhyay. “Optimal Transport Based Control of Granular Imaging System in Space”. In: *IWSCFF 17-17*. (2017).

- [27] M.B. Quadrelli et al. “Dynamics of Drag-Free Formations for Earth Imaging Applications”. In: *AIAA/AAS Astrodynamics Specialist Conference and Exhibit* (2006).
- [28] D.G. Shuster. *Dynamic Response of Dielectric Lenses Influenced by Radiation Pressure*. Rochester Institute of Technology: Master’s thesis, 2014.
- [29] M. Snow and J. Van lent. “Monge’s Optimal Transport Distance for Image Classification”. In: *CoRR* (2016).
- [30] C. Villani. *Optimal Transport, Old and New*. Springer, 2009.
- [31] J. Zemánek, S. Čelikovský, and Z. Hurák. “Time-optimal Control for Bilinear Nonnegative-in-control Systems: Application to Magnetic Manipulation”. In: *Elsevier* (2017).
- [32] J. Zemánek and Z. Hurák. “Feedback linearization approach to distributed feedback manipulation”. In: *American Control Conference (ACC), Montreal* (2012).
- [33] A. Zlotnik and J. Li. “Synthesis of Optimal Ensemble Controls for Linear Systems using the Singular Value Decomposition”. In: *IWSCFF 17-17*. (2017).

# Appendix A

## Mathematical preliminaries

In this appendix a brief description of the notation and of the mathematical methods used is given. A more comprehensive description can be found in [14, 27].

### A.0.1 Notation

In order to derive the equations to model and control the system under study, several mathematical objects will be needed. It is thus useful to briefly review the notation that will be used.

A vector in coordinate-free form will be denoted as  $\underline{\mathbf{V}}$ , it is a quantity possessing both magnitude and direction in three-dimensional space. Vectors in coordinate-free form can also be called Gibbsian vectors. It must be noted that this description of a vector is independent of any reference frame.

A versor is a vector whose magnitude is unity (i.e. its Euclidian norm is unity) and the symbol used is  $\hat{\underline{\mathbf{v}}}$ .

A column vector consists of the components of a coordinate-free vector resolved in a specified reference frame. It will be denoted as  $\mathbf{V} = [V_1 \ V_2 \ V_3]^T$ . In the control sections of this dissertation, the same notation will be used to describe state vectors being them column vectors.

In analogy with vectors, a dyadic is a second rank tensor denoted by  $\underline{\underline{\mathbf{T}}}$ , a geometric object that is independent of any reference frame. A dyadic satisfies the tensor product:

$$(\underline{\underline{\mathbf{u}\mathbf{v}}})\underline{\mathbf{r}} = \underline{\mathbf{u}}(\underline{\mathbf{v}} \cdot \underline{\mathbf{r}}) \quad (\text{A.1})$$

In the equation A.1 above the object  $\underline{\underline{\mathbf{u}\mathbf{v}}}$  is a dyadic while the tensor product between a dyadic and a vector results in a vector. It is useful to notice that this operation is

carried out in coordinate-free form and that the tensor product is not commutative. The dot in A.1 stands for the inner product between coordinate-free vectors. The dyadic is the extension of the concept of the vector in coordinate-free form.

In analogy with column vectors, matrices represent the components of a dyadic in a specified reference frame. Matrices will be denoted as  $[A]$ . Regarding the control section the same notation will be used to describe state and control matrices.

### A.0.2 Reference frames and vectrices

A reference frame consists of three basis vectors of unit length, mutually perpendicular, and right-handed. A reference frame will be indicated as  $\mathcal{F}_A$  and its basis vectors as the triple  $\{\hat{\underline{\mathbf{a}}}_1 \hat{\underline{\mathbf{a}}}_2 \hat{\underline{\mathbf{a}}}_3\}$ . It is useful to describe a reference frame using the vectrix concept. A vectrix is a mathematical object that possess the characteristics of both a vector and a matrix. The vectrix associated with reference frame  $\mathcal{F}_A$  is defined as:

$$\mathcal{F}_A := [\hat{\underline{\mathbf{a}}}_1 \hat{\underline{\mathbf{a}}}_2 \hat{\underline{\mathbf{a}}}_3]^T \quad (\text{A.2})$$

Where the elements  $\hat{\underline{\mathbf{a}}}_i$  are the basis vectors of reference frame  $\mathcal{F}_A$ . Using vectrices is possible to relate rigorously coordinate-free vectors and their relative representation in a specified reference frame (i.e. the column vector defined above). In analogy with the inner product between column vectors an operation between vectrices and column vectors can be defined. Starting from the definition of vector components in a specified basis, vector  $\underline{\mathbf{V}}$  can be described through its components in reference frame  $\mathcal{F}_A$ .

$$\underline{\mathbf{V}} = \sum_{i=1}^3 V_i \hat{\underline{\mathbf{a}}}_i \equiv \mathcal{F}_A^T \mathbf{V} \equiv \mathbf{V}^T \mathcal{F}_A \quad (\text{A.3})$$

Where the last two operations are the symbolic way of representing the vector  $\underline{\mathbf{V}}$  in the coordinate frame  $\mathcal{F}_A$  through its components  $\mathbf{V}$  as a column vector. In a similar way, vectrices can be used to link a dyadic with the matrix describing its representation in a specific reference frame.

$$\underline{\underline{\mathbf{T}}} = \mathcal{F}_A^T [T] \mathcal{F}_A \quad (\text{A.4})$$

Matrix  $[T]$  contains the components of the dyadic  $\underline{\underline{\mathbf{T}}}$  with respect to the reference frame  $\mathcal{F}_A$ .

Vectrices can relate inner product and cross product between vectors in coordinate-free form and their relative counterpart in a specified reference frame. In the next chapter only the cross product transformation will be needed and therefore it is the only relation that will be derived here. A complete discussion is given in [14]. Cross

product between vectrices both representing reference frame  $\mathcal{F}_A$  is defined as:

$$\mathcal{F}_A \times \mathcal{F}_A^T := \begin{bmatrix} \underline{\mathbf{0}} & \hat{\underline{\mathbf{a}}}_3 & -\hat{\underline{\mathbf{a}}}_2 \\ -\hat{\underline{\mathbf{a}}}_3 & \underline{\mathbf{0}} & \hat{\underline{\mathbf{a}}}_1 \\ \hat{\underline{\mathbf{a}}}_2 & -\hat{\underline{\mathbf{a}}}_1 & \underline{\mathbf{0}} \end{bmatrix} \quad (\text{A.5})$$

The result is a skew-symmetric vectrix whose elements are basis vectors. The following equation uses A.5 and vectrix notation to resolve the vector cross product in components with respect to a specified reference frame:

$$\underline{\mathbf{u}} \times \underline{\mathbf{v}} = \mathcal{F}_A^T \mathbf{u} \times \mathcal{F}_A^T \mathbf{v} \equiv \mathbf{u}^T \mathcal{F}_A \times \mathcal{F}_A^T \mathbf{v} = \mathcal{F}_A^T [\mathbf{u}]^\times \mathbf{v} \quad (\text{A.6})$$

Where  $[\mathbf{u}]^\times$  is the skew-symmetric matrix associated with the column vector  $\mathbf{u}$  and it is defined as:

$$[\mathbf{u}]^\times := \begin{bmatrix} 0 & -u_3 & u_2 \\ u_3 & 0 & -u_1 \\ -u_2 & u_1 & 0 \end{bmatrix} \quad (\text{A.7})$$

### A.0.3 Vector derivatives in different reference frames

Time derivative of coordinate-free vectors, unlike scalars, depend on the reference frame with respect to which are taken. The time derivative of a vector in a specified coordinate frame is defined as the derivative of its components in that coordinate frame [15]. In this dissertation many reference frames are needed and the derivatives must be transported between these frames. To avoid confusion a capital letter subscript will be used to indicate the frame of reference in which the time derivative is taken. This notation is needed for coordinate-free vectors, on the other hand, column vectors time derivative will be denoted with an upper dot. In deriving column vectors there is no ambiguity because these vectors represent already the components with respect to a specific coordinate frame.

A useful theorem to transform time derivatives of coordinate-free vectors taken in different reference frames is The Transport Theorem [16]. It allows to relate time derivatives in frames rotating with respect to each other.

$$\overset{A}{\dot{\underline{\mathbf{V}}}} = \overset{B}{\dot{\underline{\mathbf{V}}}} + {}^A\boldsymbol{\omega}^B \times \underline{\mathbf{V}} \quad (\text{A.8})$$

$\overset{A}{\dot{\underline{\mathbf{V}}}}$  is the time derivative of vector  $\underline{\mathbf{V}}$  taken with respect to reference frame  $\mathcal{F}_A$ , while  $\overset{B}{\dot{\underline{\mathbf{V}}}}$  is with respect to  $\mathcal{F}_B$ .  ${}^A\boldsymbol{\omega}^B$ , is the angular velocity of frame  $\mathcal{F}_B$  with respect to frame  $\mathcal{F}_A$ . The same theorem can be applied to vectrices being them formed by basis vectors (basis vectors are always in coordinate-free form). Time derivative of a vectrix is defined as the time derivative of its basis vector elements.

$$\overset{B}{\mathcal{F}}_B := 0 \quad (\text{A.9})$$

$$\overset{A}{\mathcal{F}}_B = [\overset{A}{\hat{\mathbf{b}}}_1 \ \overset{A}{\hat{\mathbf{b}}}_2 \ \overset{A}{\hat{\mathbf{b}}}_3]^T = \overset{A}{\boldsymbol{\omega}}^B \times \overset{A}{\mathcal{F}}_B \quad (\text{A.10})$$

Equations A.10,A.9 are derived applying the Transport Theorem to the unity vectors of  $\overset{B}{\mathcal{F}}_B$  considering  $\overset{B}{\hat{\mathbf{b}}}_i = \mathbf{0}$

According to the definition of time derivative of a vector given above, the components form version of  $\overset{A}{\mathbf{V}}$  is:

$$\overset{A}{\mathbf{V}} = \sum_{i=1}^3 \dot{V}_i \hat{\mathbf{a}}_i \equiv \overset{A}{\mathcal{F}}_A^T \dot{\mathbf{V}} \equiv \dot{\mathbf{V}}^T \overset{A}{\mathcal{F}}_A \quad (\text{A.11})$$